UCLouvain

École polytechnique de Louvain

Atomic transistors

Author: **Jérémie PIRARD**
Supervisor: **Sorin MELINTE**
Readers: **Sorin MELINTE, Benoît HACKENS, Philippe LECLERE**
Academic year 2019–2020
Master [120] in Physical Engineering

Contents

Abstract

Single-atom and single-molecule transistors control the current flowing between two electrodes separated by a nanogap. This enables the tuning of electronic transport at quantum scale. Accordingly, these transistors are based on quantum point contacts, where the quantum effects on the electronic transport are observed. This work will first review the current state of the art in this domain. The experimental methods commonly used to create single-atom and single-molecule transistors are the mechanical break junction, the electromigration technique and the electrochemical method. We review the theory underlying these devices and the applications of the single-molecule transistors in quantum computing. With a molecule linked to two electrodes, the spin qubit of an atomic nucleus can be controlled to perform quantum computing operations. Then, we studied a spectrometry method that could be useful to characterize such systems: microwave impedance microscopy. This non-invasive, scanning-probe method uses the reflection of a microwave signal by a sample to measure its electronic local properties. We performed finite-element simulations to demonstrate the efficiency of this method with nano-sized samples. We demonstrate the ability to detect gap sizes of the order of the nanometer.

Acknowledgements

First, I have to thank my supervisor, Dr. Sorin Melinte for his help, his patience and his advices during the realisation of this thesis, especially during these difficult times of COVID-19 crisis. I would like to also thank the members of his research team for the useful help and advices they provided me. More generally, I thank all the people of ICTEAM that helped me at some points, for software and practical issues. I would also like to express gratitude to the jury members that will take the time to read and comment this work.
Finally, I must express my very profound gratitude to my parents, to my family and friends for providing me with unfailing support and continuous encouragement throughout my years of study and through the process of researching and writing this thesis. I express my gratitude to all the people that have read my work and helped me to improve it with their comments. This accomplishment would not have been possible without them. Thank you.

Useful abbreviations

- 0D: Zero-dimensional
- 1D: One-dimensional
- 2D: Two-dimensional
- 2DEG: Two-dimensional electron gas
- 3D: Three-dimensional
- AFM: Atomic force microscopy
- AMSC: Atomic-sized metallic contacts
- DoS: Density of states
- EBJ: Electromigration break junction
- EBL: Electron beam lithography
- EM: Electromigration
- FESEM: Field-effect scanning electron microscope
- GMR: Giant magnetoresistance
- MBJ: Mechanical break junction
- MD: Moleculars dynamics
- MIM: Microwave impedance microscopy
- MOSFET: Metal oxide semiconductor field effect transistor
- PMMA: Polymethylmethacrylate
- QPC: Quantum point contact
- QTF: Quartz tuning fork
- SAT: Single atom transistor
- SEM: Scanning electron microscope
- SMM: Scanning microwave microscopy
- TMF: Transverse magnetic field
- V_g: Gate-source voltage
- VNA: Vector network analyser
- W: Width of the channel of a quantum point contact

Chapter 1

Introduction and state of the art

Silicon-based transistors are the main building block used in electronics. Their number per area unit in integrated circuits has approximately doubled every twelve-months since their first introduction, following the famous Moore's Law [1] . However MOSFET[2] [3] Si transistor technology is reaching the limits of miniaturization because existing materials and technologies are approaching their physical limits. Semiconductor industry must therefore overcome new technological challenges. And for some of them, there are no known solutions [Peercy, 2000]. These challenges are summarized in table A.1.

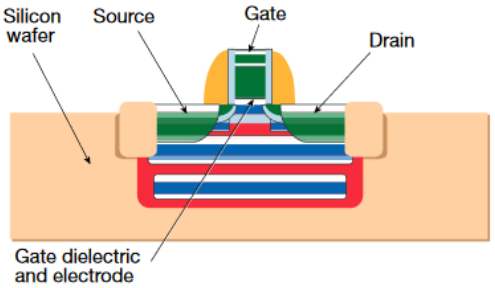

Figure 1.1: Schematic structure of a MOSFET transistor. Ref. [Peercy, 2000].

In parallel, single-atom transistor (SAT) technology is currently being developed, following research in quantum electronics. The first single-atom transistor was pioneered in 2004 by Pr.Thomas Schimmel and his team [Xie et al., 2004]. The device uses an electrostatic gate to move a silver atom in and out of a small junction, allowing switching of electrical contact (figure 1.2). Since then, other SAT techniques were used. This new type of transistor may offer new perspectives in electronics, thanks to its properties: low-power consumption (maximum operating V_g is 30 mV while MOFSETs typical threshold voltage [4] is around 0.7V) and small dimensions (1nm for the SAT switching unit while the projected Si gate size limit is 5 nm)

[1] An empiric law observed by Gordon Moore, engineer and co-founder of Intel.

[2] Metal oxide semiconductor field effect transistor.

[3] Electronic transistor consisting of three electrodes (source, drain and gate). Electrons flows from the source to the drain. The channel of current is controlled electrostatically by the gate. The current is therefore controlled by the gate voltage, called V_g. Mass-produced and miniaturized, MOSFET are widely used in integrated circuits.

[4] Lowest gate voltage required to close the circuit.

[Xie et al., 2017]. Since this technology relies on quantum electronic transport properties, it may be used in the emerging field of quantum computing. This chapter will introduce theoretical and experimental notions of SAT. First, quantum point contacts (on which SAT technology is based) are defined. Then, experimental methods used to create and control SAT devices are discussed. Then, a description of fundamental theoretical notions and simulation techniques is given. Finally, applications in quantum computing are discussed.

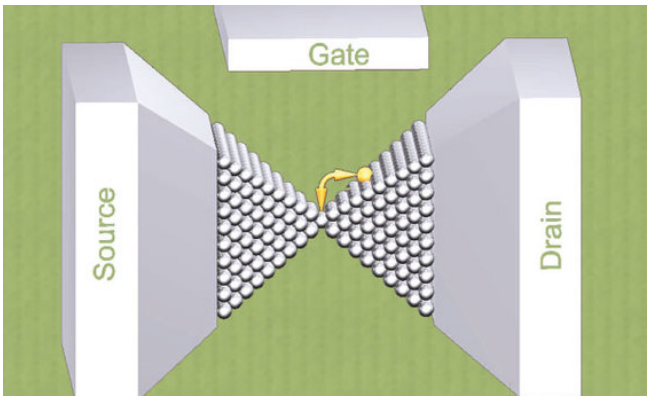

Figure 1.2: Working principle of a single-atom transistor. Voltage applied on the gate is used to close or open electrical contact between source and drain. Ref. [Obermair et al., 2010]

1.1 Quantum point contacts (QPC)

Quantum point contacts are defined by narrow and small contacts between two (2D or 3D) reservoirs of electrons. Since the width (W) of these interconnection is very small (of the order of the Fermi wavelength λ_F), the contact can be considered as a one-dimensional channel [5]. At this small scale, Schrödinger equation has to be solved, and the resulting electronic wavefunction possesses different transverses modes. Only a finite number (depending on W) of these modes can be transmitted. Thus, when W is increased above a certain value (determined by the Schrodinger equation), a new transverse mode is allowed to go through the channel. As a result, conductance exhibits a step function (figure 1.4) of W (which is usually controlled by a bias voltage). The conductance steps show discrete values. They are integer multiples [6] (corresponding to the number of transverse modes transmitted) of G_0, the quantum of conductance (derivation of this result is shown in section 1.1.3).

This "conductance quantization" is a fundamental aspect of the quantum nature of electronic transport at this scale, described by the Landauer-Buttiker formalism.
QPC are useful devices to illustrate the basics of quantum transport, and are widely used for research purposes. In this section, various types of quantum point contact are described. The conductance quantization will be explained in details as well.

[5] The electronic transport has to be ballistic. In other words, the mean free-path of electron must be longer than the channel length.

[6] In theory only. Non-integer multiples of G_0 have been observed in experimental conditions.

1.1.1 2DEG-based QPC

Discrete conductance was observed for the first time in QPC in 2 dimensional electronic gas (2DEG) [van Wees et al., 1988] in GaAs-AlGaAS heterostructures. The following explanations are based on the B.Brun's thesis [Brun, 2014].

2DEG To obtain a quasi 2D gas of electrons, GaAs-AlGaAs heterostructures are commonly used. They are fabricated using molecular beam epitaxy. This process produces pure devices, consisting in a stack of different materials (figure 1.3). At the interface between the two semiconductors, a band offset is observed, acting as a quantum well (figure A.2). So electrons are confined in the normal direction (along x-axis) to the interface, but free to move along y and z-axis. As a consequence, they have quantified energy levels of confinement in the quantum well: $E_n = \frac{k_z^2}{2m*} + \frac{k_y^2}{2m*} + E_n^{conf}$. Usually the confining potential is so narrow that only one energetic level n is available. It then results in a high mobility 2DEG thanks to the purity of the sample.

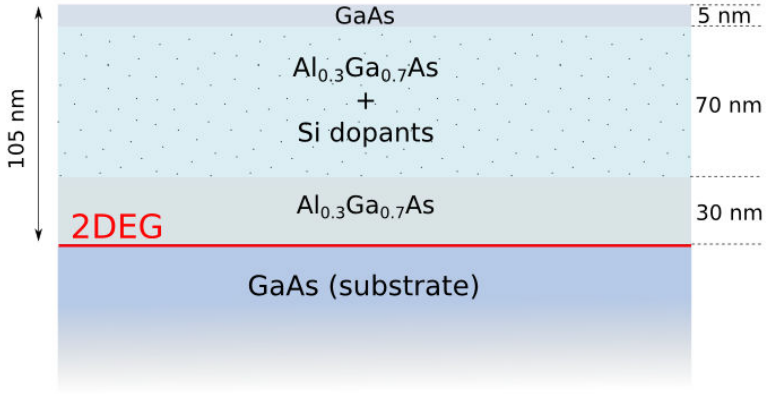

Figure 1.3: Schematic view of a typical GaAs-AlGaAs heterostructure. Ref. [Brun, 2014]

Electrostatic constriction A quantum point contact is then defined by lithography in the newly fabricated 2DEG. Two metallic electrodes separated by a small gap (fig. A.1) are deposited. A gate is then placed above this "hole" and the channel can be closed or opened, by electrostatically confining electrons underneath it, using the bias voltage. V_g is therefore used to define the path of electrons and, as a result, to control the width W of the QPC. Figure A.30 shows a step function of conductance obtained with this device.

Disadvantages The main disadvantage of AlGas-based structures is their temperature dependency. Above a given value, conductance steps acquire a non-zero slope and there are no distinguishable, because the electronic transport is no longer ballistic inside the channel. In addition, molecular beam epitaxy is a costly and slow process. Hence, these structures are limited to research applications and they are addressed here for theoretical purposes.

1.1.2 Other types of QPC

Atomic sized metallic contacts (ASMC) Single-atom QPC use atomic-sized junctions between two metallic electrodes (figure 1.2). W is therefore defined by the size of the contact

itself. Using quantization results from previous experiments on 2DEG, the first conductance steps were observed on Pt constrictions (figure A.25). This phenomenon was interpreted as atomic rearrangements in the contact occurring when modifying the control voltage, leading to a modification of W [Rubio et al., 1996].
Atomic sized metallic contacts exhibit quantized conductance at room temperature. Since the contact size is smaller than the mean free path of electrons, the electronic transport is ballistic [Xie et al., 2008]. Two techniques are mainly employed to create these structures: mechanical breaking junction and electrochemically-based methods, and will be addressed longer in the next section. In practice, most of experiments on ASMC conductance result in conductance being a non integer multiple of G_0. Different explanations were proposed, such as defect-enhanced scattering in the junctions [Agrait et al., 2003], or the existence of multiple channels acting as series resistance [de Heer et al., 1997]. The first QPC switch at room temperature was an ASMC [Xie et al., 2004].

Graphene QPC Graphene is a recently discovered two-dimensional material with exceptional physical properties such as: high conductivity, high mechanical resistance and a unique linear dispersion relation at the Dirac points (edges of Brillouin zone). However, the relativistic nature (caused by this band structure) of electronic transport makes the creation of effective QPC very difficult. Two ways of making QPC in graphene were reported. The first one is to define electrodes such as in AlGas structures. But defining an electronic path electrostatically between electrodes is hard, due to the creation of a pn junction which is gap-less and conductive and short-circuit the constriction. That said, conductance can still be tuned by a transverse magnetic field in the quantum Hall regime [Zimmermann et al., 2017].The second one is to define a small channel by etching. This method has proven to be effective if the process is well-controlled [Tombros et al., 2011]. Conductance quantization was observed and is shown in figure A.27. However, it requires low temperature, and applications are now limited to research.

Superconductive QPC Under a certain critical temperature T_c, superconductive materials exhibit a null electronic resistance. Electrons form Cooper pairs, which have a creation energy Δ (the energy gap between normal state and superconductive). They carry supercurrents until a certain value I_c is reached, called critical current. In superconductive QPC, I_c is quantified and steps as a function of W have been observed [Muller et al., 1992], in accordance with theory developed in [Beenakker and van Houten, 1991]. These steps are shown in figure A.26.

1.1.3 Conductance quantization

As explained previously, a quantum point contact can be considered as a quasi 1D channel, with transverses dimensions of the order of λ_F. The transport regime is assumed ballistic inside the channel, and electrons flow in the 1D channel without scattering. Electrons behave as waves and the channel acts as a waveguide. Multiple transverse electronic modes are well defined. Rolf Landauer established the link between conduction and transmission. Starting from the formula inside a 3D channel:

$$I = e \sum_{n=1}^{N} \int_{Ef}^{Ef+Vsd} D_n(E) v_n(E) T_n(E) dE \tag{1.1}$$

With Dn the 1D density of states, v_n the group velocity of transverse modes and Tn the transmission probability of each transverse mode, e the electronic charge and E the energy.
He established [7] his famous Landauer formula:

$$G = \frac{2e^2}{h} \sum_{n=1}^{N} T_n \tag{1.2}$$

This is a fundamental result for quantum transport theory. It shows that each electronic mode has a conductance of $\frac{2e^2}{h}$, and total current can be linked to the transmission of each mode. This equation constitutes the basics of Landauer formalism, used to calculate conductance in the ballistic regime.
To effectively explain the quantization conductance, the transmission probabilities T_n have to be calculated. The Schrödinger equation must be solved. The saddle-point model [Büttiker, 1990] is an effective way to describe the constriction. In this model (whose name come from the saddle point at the origin), electrons are focused into a channel by a quadratic potential V:

$$V(x, y) = V_0 - \frac{1}{2} m\omega_x^2 x^2 + \frac{1}{2} m\omega_y^2 y^2 \tag{1.3}$$

where x is the transport axis and y the transverse axis. ω_x and ω_y are parameter which describe the curvature of the potential (i.e. the shape of the channel). This Hamiltonian can be separated along the two axes. It reduces itself to an harmonic oscillator along y-axis direction. Transverse modes are therefore conventional eigenmodes ϕ_n with energies $E_n = \hbar\omega(n + \frac{1}{2})$ where n is the level index. The transmission probability for each mode can be found:

$$T_n = \frac{1}{1 + e^{-\pi\epsilon_n}} \tag{1.4}$$

with

$$\epsilon_n = \frac{2(E - \hbar\omega_y(n + 1/2) - V_0)}{\hbar\omega_x} \tag{1.5}$$

This result is summarized in figure 1.4. Equation 1.2 (combined with (1.5 and 1.4) can therefore be viewed as a step function of V_0 (gate voltage). Two conditions are required to observe steps: $\frac{\omega_y}{\omega_x} > 1$ (the channel must be narrow) and $\hbar\omega_y, \hbar\omega_x > k_B T$. The explanation of the steps lies in the energetic separation of transverse modes. When the channel is narrow, a limited number of states is located below Fermi energy and participates to the transmission. When W increases (i.e. ω_y is reduced), the number of modes below E_f increases.
The link between conductance and the number of electronic modes has been experimentally confirmed and these modes were observed in [Topinka et al., 2000]. This experimental result is illustrated in figure A.29.

[7] Derivation of this result can be found in [Brun, 2014].

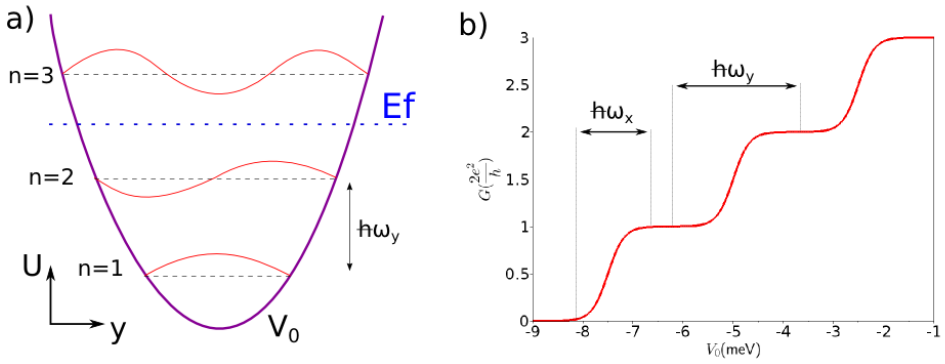

Figure 1.4: a) Transverse mode energies in the saddle-point model. Only available modes (i.e. below E_f) participate to the transport. b) Diagram of conductance vs V_o. The smoothness of the steps is governed by ω_y and ω_x. Ref. [Brun, 2014].

1.2 Experimental methods

This section focuses on QPC with a single to a few atoms/molecules contacts. The methods employed to create these contacts and tune their size in order to create stable switches are addressed in this section.

1.2.1 Mechanical break junction (MBJ)

The break-junction technique was first employed in 1983 [Moreland and Hansma, 1984] and is based on the bending of a substrate supporting two electrodes (called the drain and the source). These electrodes are separated by a sharp junction (with a width down to a few atoms). The bending of the substrate causes an horizontal displacement between the drain and source. Hence, the gap (and the atomic configuration of the junction) can be controlled. In addition, an electrostatic gate or electromigration methods can be used to switch (usually between two stable electronic configurations [Schirm et al., 2013]).

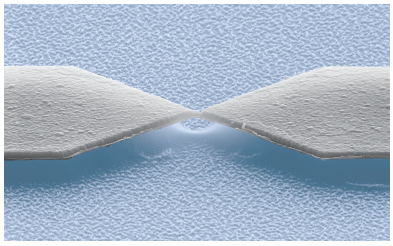

Figure 1.5: SEM image of a nanobridge created for mechanical break junction(false colors). Ref. [Schirm et al., 2013].

Sample creation The commonly used metal is Al. On a bronze wafer with a size from 50 to 200 μm, a layer of polymide (2-3 μm) is deposited by spin-coating. This polymer is used to electrically isolate the structure from the substrate and will be removed by plasma etching to create the bridge structure. The shape of the electrodes is then defined by electron-beam lithography with a MMA-MAA/PMMA resist. After removal of PMMA, an Al (or any other metal) layer is deposited by electron beam evaporation. The "bridge structure" is then created by dry ion etching with O_2 (and CF_4). The layer below the electrodes is removed during the process, creating a suspended nanobridge. This standard process was used in [Schirm et al., 2013] and [Martin et al., 2008], with slight variations in the parameters. Figure 1.5 shows a sample obtained with this method.

Bending and characterization To allow a precise monitoring of the distance between electrodes, the substrate has to be flexible. The electrodes are contacted electrically and the substrate is mounted on a three-point bending mechanism (figure 1.6). The bending is obtained by pushing on the two points at the ends or on the middle one. Different devices are used to apply the force (figure 1.6). Electrode gap (as function of the bending) is monitored using I-V curves. A resolution of the order of the Angstrom can easily be obtained [Ballmann and Weber, 2012]. With a linearly varying bending force, series of sharp changes of conductance were observed

[8] (figure A.5). Hence, bending can be used to prepare the sample into a given conductance configuration [Schirm et al., 2013].

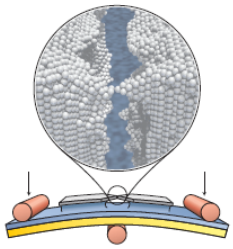

Figure 1.6: Schematic illustration of the 3 points bending mechanism. An artistic view of the atomic contact between the two electrodes is shown above. Ref. [Schirm et al., 2013].

Theoretical model of the junction An explanation given for these abrupt changes is atomic reconfigurations occurring during the bending. The simulations performed by [Schirm et al., 2013] have confirmed this hypothesis[9]. The theoretical results have been obtained by performing molecular dynamics and tight-binding operations. The simulation process is as it follows: electrodes were separated at a constant speed. Using MD, atomic configurations were computed for some gap values. Figure 1.7 (b) and (c) show the computed atomic configurations. The transmission probability of each channel was computed [10] as well as the number of open conduction channels. Some results can be drawn from this figure. The first one is that the conductance has values of non integer multiples of G_0 while the number of open channels exhibit a step function of displacement. The conductance shows a random behaviour, as each value of G corresponds to a given atomic configuration. However, this non multiple integer conductance does not prevent the creation of a bistable switch. In conclusion, bending is generally a good method to control the atomic configuration of the switch.

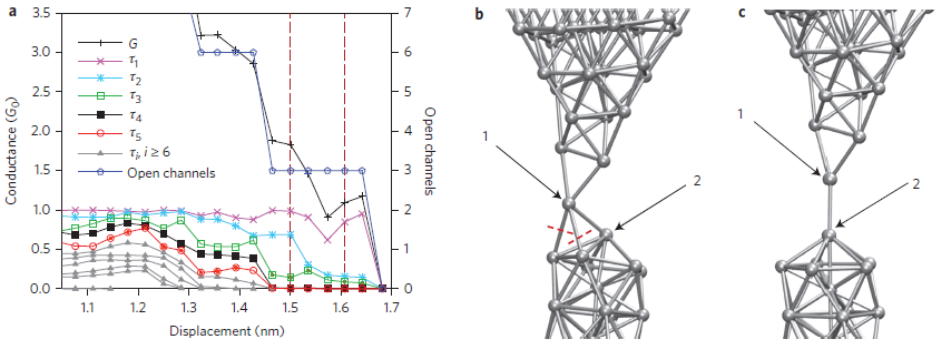

Figure 1.7: a) Theoretically determined conductance as a function of electrode gap. Transmission probabilities of the eigenmode τ_i is also indicated. b) and c) Simulated atomic configurations with respectively 1,50 and 1,61 nm of displacement. Ref. [Schirm et al., 2013].

[8] At small temperatures.

[9] Note: these simulations included only a few atoms and did not represent the true structure. However, the experimental results and the simulations were in accord.

[10] Experimental data from superconductive state have been used.

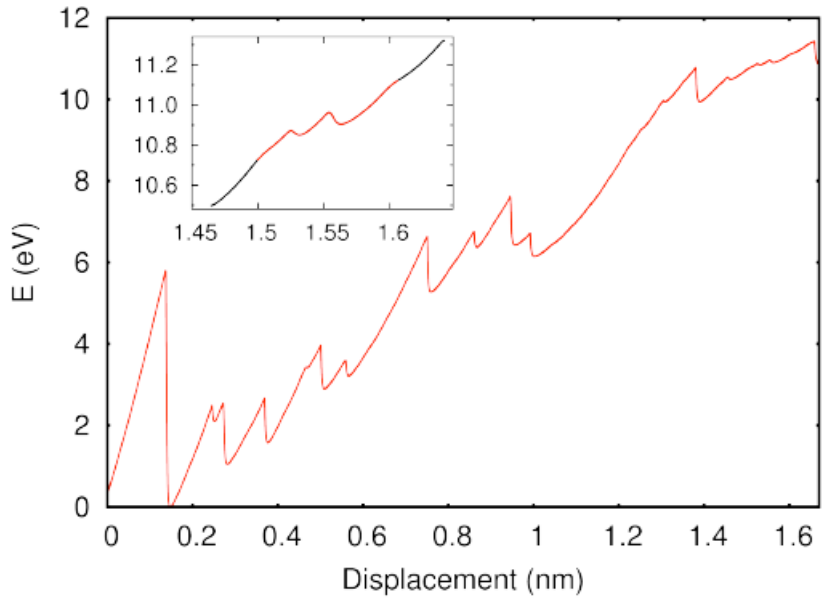

Figure 1.8: Simulation of the total energy of a few-atoms contact junction as a function of the displacement between two electrodes. Ref. [Schirm et al., 2013].

The atomic stretching mechanics were also considered. Total energy E as a function of displacement was computed. It shows a series of elastic phases with a linear increase of E and sharp plastic phases, corresponding to an atomic rearrangement caused by the breaking of a bond (figure 1.8).

Current-driven MBJ transistor Electromigration consists in the rearrangement of atoms inside the contact due to thermal effects, strong currents or mechanical stretching. Using a current allows the conductance state to be tuned without the use of an electrostatic gate or mechanical bending. Therefore, only two terminals are required (the source and the drain). The creation of an electromigration-driven switch was done by [Schirm et al., 2013]. To realize this kind of device, a bi-stable configuration between two conductance states must be reached. In other words, the conductance must be able to switch between two and only two levels. This was effectively achieved using a control current. Each time a sharp step in conductance was observed, the ramp direction of the current was reversed, with a changing rate proportional to the step height. A bi-stable configuration was finally reached after repeating this operation several times (this process is illustrated in figure 1.9). The electromigration phenomenon underlying the switching process will be described in details in the appropriate section.

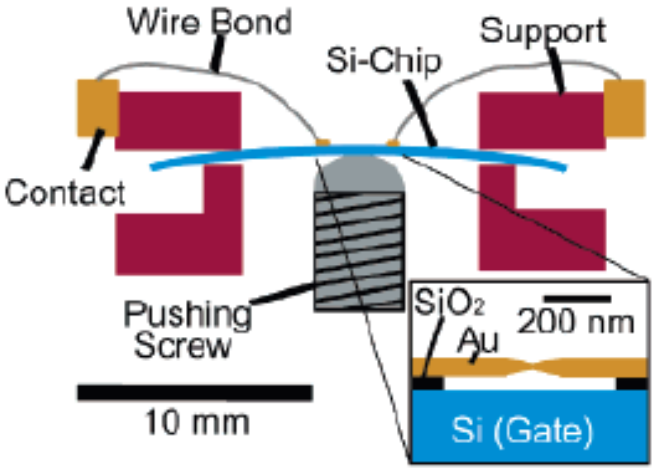

Figure 1.10: Schematic view of a MBJ sample with Si substrate used as a gate.Ref. [Champagne et al., 2005].

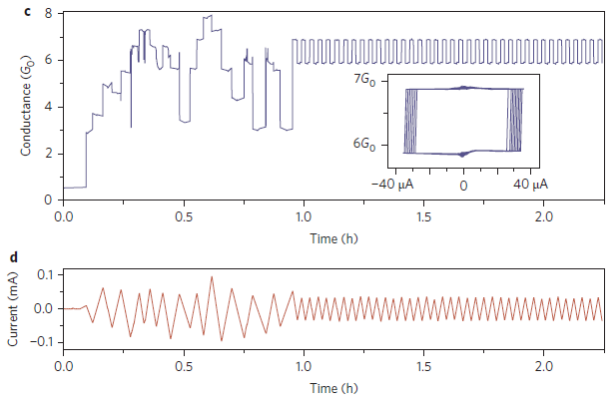

Figure 1.9: Examples of bistable configurations and switching events. Ref. [Schirm et al., 2013].

Gate controlled MBJ transistor MBJ was also employed to create a SAT [Champagne et al., 2005] [Martin et al., 2010] [Martin et al., 2009] controlled by an electrostatic gate. In this case, the fabrication differs as the gate must be added to the structure (figure 1.10). Usually, a highly doped Si substrate supporting the bridge structure fulfils this function (another electrode can also be deposited under the "bridge"). Adding a gate is sometimes complicated since it must be well isolated from the source and drain. These structures were first engineered for research purposes, such as the study of electrical properties of a single molecular wire deposited chemically between the two electrodes [Martin et al., 2008]. Two types of this SAT are currently explored : molecular and atomic ones.
In molecular transistors, a long molecule is lying (usually C_{60}) between the two electrodes. In this case, V_g is used to shift molecular energy levels and hence tune the molecular conductance. Successful experiments were performed, and the ability to tune the energy levels were demonstrated [Xiang et al., 2013] [Champagne et al., 2005]. However, significant challenges remain before creative effective switches remains, as the gate effect is still too small to effectively tune the conductance [Perrin et al., 2015]. Also, the electrostatic interaction modifies the charge dis-

tribution inside the molecule, and the gate effect is not symmetric [Champagne et al., 2005](in respect to V_g). This is illustrated in figure A.6.
A gate SAT realised by MBJ has been engineered in 2009. Its ability to realise shifting cycles were proven by [Martin et al., 2009]. The gate acts as an electromigration agent, as the electrostatic force is employed to create or remove atoms from the junction, and therefore closing or opening the contact. As a consequence, depending on V_g values, the electronic transport regime was either tunnelling (varying linearly with V_g) or quantized (the conductance has integer values of G_0). However, this encouraging result was only obtained at cryogenic temperatures (around 7 K).

Drawbacks and advantages The main drawback of MBJ technique is the push road mechanism. It must be used with a motor, and a complex system of 3 points (or 1) pushing mechanism. This is a major constraint preventing integration in mass-produced chips. To overcome this, some solutions were proposed such as:

- A micrometer-scale push rod ;
- A thermal-enhanced actuator able to generate forces and deformation as a function of heat [Meng et al., 2015];
- A cantilever deformed with the use of terahertz waves [Gong et al., 2013];

However, they are still in development. Another major drawback is the temperature dependency, as no precise control of G has been recorded at room temperature so far, unlike in case of the electrochemical-based SAT. MBJ is a time-consuming technique as well, as it involves many fabrication steps and a specific equipment. However, this technique offers singular advantages. The main one is the resolution. With MBJ, materials can be scaled down to the molecular level, and the gap between electrodes can be monitored to the picometer range. The sample is very small (several μm), and it can be integrated into experimental systems. In addition, this method avoids the use of chemicals to manipulate the junction. Therefore, the risk of contamination is greatly reduced. In general, the samples obtained by MBJ are stable and of high quality. In conclusion, MBJ is perfectly suited for experimental purposes, as it enables precise measurements on great quality samples. However, it requires specific conditions and equipment to be effective for other applications, and SAT operating in normal conditions have not been developed yet.

1.2.2 Electromigration breakdown junction

Electromigration consists in the migration of metallic atoms caused by an electric current. The electronic momentum is transferred to the atoms, causing a gradual motion. This effect is proportional to the current density inside the conductor. In metallic nanoconstrictions, the density reaches great values and EM is increased. This atomic motion causes the metallic interconnection to shrink down, even to nanoscale sizes. Therefore, with a sufficiently small width and high currents, the breakdown of the structure can occur, and the constriction is split into two distinct electrodes. Thus electromigration can be used as a tool to create small gaps [11].

[11] It is also a problem in the semiconductor industry, when the phenomenon occurs when undesired.

This method is similar to MBJ, but it uses electrical current instead of a mechanical force. The size of the gap cannot be precisely tuned, as the migration of atoms is randomized [12].

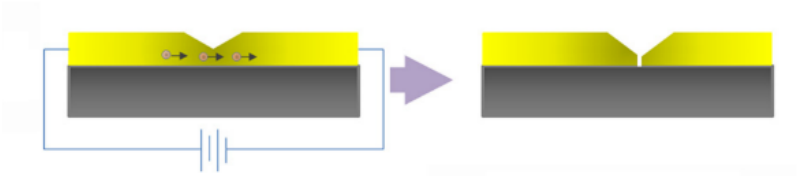

Figure 1.11: Schematic explanation of the electromigration process. Under a strong electric field, electrons transfer their momenta to atoms, which migrate in the direction of the current. Ref. [De Los Santos Valladares et al., 2010]

Creation of junction using EBJ As the breakdown requires high density currents, a heat supply is usually used to help the process by increasing the mobility of the atoms. This heat must therefore be controlled, as it can induces undesired effects (melting of metals, destruction of molecules and formation of metallic debris near the gap). The process is as it follows. First, the initial electrodes or wires are usually defined using optical or electron beam lithography [De Los Santos Valladares et al., 2010]. Wires can also be defined by evaporation [Prins et al., 2009]. Then a voltage is ramped over the junction and the width of the gap is monitored using the current. Two schemes are usually employed: a passive and an active one. In the passive scheme, a voltage is ramped over the junction while the current is monitored until the junction breaks (typically the electromigration process starts at a few milliamperes). In the active scheme a computer program ramps the voltage until either the resistance rises above a threshold or a maximum voltage is reached, whereupon it is returned to zero (or another lower value) and the ramp is started over[Heersche et al., 2007]. This method enables a slower and more precise control of the conductance. EBJ junctions are employed to perform experiments on single molecules as well.

Self breaking A method called "self-breaking" was recently developed and has been proven efficient in reducing metal debris [O'Neill et al., 2007]. This process relies on thermal fluctuations of atoms inside the junction. The process starts with a classical electromigration procedure. A monitored current is applied until the wire is narrowed to a few atoms (i.e. when the conductance reaches the value of G_0). Then this current is stopped and the contact breaks itself due to thermal fluctuations. This process is illustrated in A.8. However, the temperature at which self breaking is possible strongly depends on the material. For example, gold can undergo self-breaking at room temperature, while Pt requires a temperature above 420 K. When used with Pt nanowires, this technique allows the creation of stable samples, since after the goal conductance is reached, one can cool down the constriction to room temperature and therefore keep the atoms fixed[Prins et al., 2009]. This makes Pt EBJ nanogaps good candidates for future applications.

Materials and other methods Other materials were used such as: Au , Zn, Ni, Si, Pt, Pd, graphene and carbon nanotubes [Xiang et al., 2016]. There have been numerous studies to

[12]It is necessary to create multiple samples at once in order to perform a statistical analysis of the phenomenon.

investigate other processes involving electromigration.

Optical lithography and focused ion beam In this experiment, a focus ion beam is used to "scratch" small gold wires prior to the electromigration process. Electromigration is enhanced at this location thanks to the defects. Therefore, this "pre-treatment" allows a control of the location of the gap. The highest number of gap sizes were in the range of 100-300 nm. Using this method [Asghar et al., 2010] achieved more than 60 % yield of devices while in the literature, values of 10% are usually reported. This process has a lot of advantages in terms of cost, time, yield and spatial control of the gap size.

Electrochemical deposition This method uses electrochemical deposition (see next section) to contact two electrodes. Once these electrodes are contacted, electromigration is used to open a nanogap [De Los Santos Valladares et al., 2010]. The experimental setup of this process is shown in figure A.10.

Evaporation Electromigration was also used simultaneously with evaporation [Naitoh et al., 2013]. This method enables the creation of gold electrodes with sub 1nm gap. This proceeds in three steps, illustrated in figure A.12. First, two thick gold electrodes separated by a gap of 4 μm are deposited on a SiO_2 substrate. The width W of this gap is then defined using two resists (fig. A.12 (a)). After, metal is deposited inside the gap with a bias voltage applied, causing electromigration to occur (b,c). The process is terminated after lift-off of the resist (d). The gap size can be modified by changing the magnitude of the bias voltage (fig. A.11).

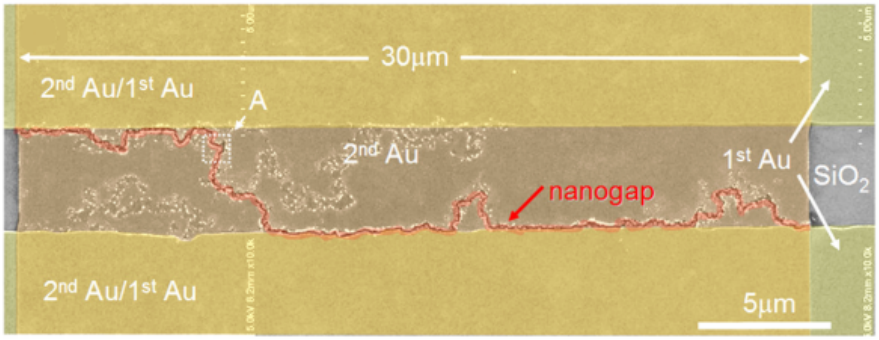

Figure 1.12: FESEM image of a fabricated nanogap electrode thanks to electromigration and evaporation. The first Au layer, the second Au layer, and the nanogap parts are indicated by the yellow, orange, and red translucent bands, respectively.Ref. [Naitoh et al., 2013].

Spatial control of electromigration with a magnetic field The effect of a magnetic field on electromigration has been investigated in [Sheikholeslam et al., 2014]. Simulations were performed on a nanowire. It shows that electromigration is increased on one side of a nanowire and reduced on the other. An explanation may lie in the Hall effect, since it increases the current density on one edge of the wire. Using the formula for electromigration (1.9) and considering the wire as an ensemble of N sub wires (each one carrying a current density j_n) in parallel, one finds $MTF_N < MTF_1$[13], as $j_N < j_1$ due to Hall effect. This was demonstrated thanks to bulk

[13]MTF: mean time failure (due to electromigration).

simulations [14] performed on a piece of metal wire with a length of 1 μm and a width of 100 nm and tight binding simulations on a lattice of 50*50 atoms.

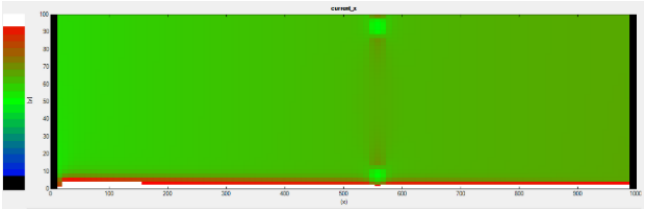

Figure 1.13: Simulated 2D map of the electromigration-induced stress in a nanowire when a transverse magnetic field is applied. The stress is focused on one edge of the wire. This was obtained by bulk calculations. Ref. [Sheikholeslam et al., 2014].

This method is a simple (it only requires a magnet) and elegant way to decrease the metal wire width in a certain area along the wire, and could be employed to fabricate nano-electrodes and nano-needles.

Physical model of electromigration The theoretical model of electromigration is based on the theory of diffusion. However, many quantities must be considered to give an efficient description of the phenomenon, such as temperature, pressure, materials, lattice defects, etc.[Baldini et al., 1993] This phenomenon has been known for a century, and a lot of articles have addressed the matter. Electromigration is nowadays a well-known phenomenon.
Let us first consider a pure metallic lattice with an atomic density N_1. The motion of interstitial atoms (and impurities) and vacancies in the lattice, all having a density N under a force $\boldsymbol{F}$ at temperature T is described by this equation:

$$\boldsymbol{J} = -D^* \nabla N + (ND/k_B T)\boldsymbol{F} \tag{1.6}$$

Where D is the absolute coefficient of diffusion at T and $\boldsymbol{J}$ is the resulting ionic current [15]. In most metals, D has this expression:

$$D = D_0 \exp\left(-E_\mathrm{a}/kT\right)$$

with E_a the activation energy of this particular diffusion process.
The force acting on the atoms must then be considered. Here, only the force resulting from the EM field is taken into account. This force is divided in two components: the first one, which is the directly applied on the atoms by the EM field and the second one, called *the wind force*, is the consequence of the motion of charge carriers on the atoms. The effective valence number $Z*$ is introduced. It represents the number of elementary charges the atom must have to undergo an electrostatic force F:

$$\boldsymbol{F} = \boldsymbol{Z}^* \boldsymbol{q}\boldsymbol{E} = \boldsymbol{Z}^* q \rho \boldsymbol{j} \tag{1.7}$$

This equation can therefore be split to consider the two contributions (respectively, the direct electrostatic force and the *wind force*):

$$\boldsymbol{F} = \left(Z^*_\mathrm{el} + Z^*_\mathrm{wd}\right) q\boldsymbol{E} \tag{1.8}$$

[14] Using a Current-Schrödinger-Poisson solver software.
[15] If a strain is applied on the metal, the diffusion is therefore anisotropic and $\boldsymbol{J}$ must be treated as a tensor.

with the wind term being [Ho and Huntington, 1966]:

$$Z^*_{\mathrm{wd}} = -\gamma z \frac{\rho_{\mathrm{d}}}{N_{\mathrm{d}}} \frac{N}{\rho} \frac{m^*}{|m^*|}$$

Where ρ and ρ_d are the partial resistivities due to scattering by lattice atoms and activated defects, respectively. N and N_d are the density of lattice atoms and activated defects, respectively. $m*$ is the effective mass of the electron, z is the electron per atom and γ is a numerical constant of the order of $\frac{3}{2}$.
With this know, we can rewrite the diffusion equation (1.6) as:

$$J = (ND/kT)Z^*q\rho j = \left(\frac{NZ^*q\rho}{kT}\right) D_0 e^{\frac{-E_a}{kT}} j$$

Under the assumption made that only the EM force is contributing to the electromigration, an estimate of the driving force in Al (at room temperature with $Z*$ = -10 and j = $10^6 A/cm$) gives around 3000 eV/m.
Also, the influence of stress has to be considered, as thin wires are usually in a highly stressed state due the high temperature at which the process of deposition occurs. They tend to shrink relative to the substrate and therefore a compressive stress appears. In addition, EM tends to induce a stress gradient along the wire. This phenomenon induces a backflow of ions, reducing the EM process. As a consequence, there is a current density threshold j_{th}. By considering the force induced by the stress field $F_j = \Omega \sum_{i=1}^{3} \frac{\partial \sigma_{ij}}{\partial x_i}$ (j = (1,2,3)), one can find that in the steady state (ion flow compensated by the stress-induced backflow):

$$Z^*qE = -\Omega \frac{\partial \sigma_y}{\partial x}$$

For an uniform stress gradient where the compressive yield limit σ_y is reached the equation above can be rewritten as:

$$|jl| = \left|\Omega \sigma_{\mathrm{y}} / Z^* q\rho\right| = (jl)_{\mathrm{th}}$$

Giving the current density threshold and the threshold length l_{th} of the wire.
In our case, EM is used to create defects in a metal lattice. However, in this model, they cannot be induced by EM alone. In fact, if $\boldsymbol{\nabla} \cdot \boldsymbol{J} = 0$, each mass leaving a point is replaced by another mass coming from elsewhere. Thus, for a perfect wire, no mass depletion can occur. The non uniform grain structure has been commonly agreed to be the main cause of vacancy formation (fig. A.15).The parameter η was introduced to characterize the microstructure of Al interconnections:

$$\eta = \left(d/\sigma_{\mathrm{d}}^2\right) \log\left(I_{111}/I_{200}\right)^3$$

d is the average grain dimension, σ_d the standard deviation of the grain dimensions, and I_{111}/I_{200}) is the degree of preferential orientation, a ratio between the (111) and (200) crystallographic dimensions [16].
This parameter is directly proportional to the resistance of a thin film to EM.
Another widely used result was found in 1969 by Black [Scorzoni et al., 1991]. He stated that the TTF (time to failure) of a conductor due to EM follows this law:

[16] Measured by X-RAY diffraction process.

$$MTF = A\left(\frac{1}{j}\right)^n e^{\left[\frac{E_a}{k_B T}\right]} \tag{1.9}$$

where A is a constant embodying several parameters, j the current density, n an exponential factor [17] and E_a being the activation energy.
This famous equation is called *Black equation* and is still used. Experimental results of this law are illustrated in fig A.16.

[17] In literature, several values are used, depending on the experimental conditions and the processes used to measure. However, values lying between 1 and 2 are mostly used. In the simple model of eq. (1.2.2), n equals 1.

1.2.3 Electrochemical techniques

Electrochemical techniques are a flexible way of designing nanogaps. Metal atoms are electrodeposited on the top of two narrow electrodes (called working electrodes) previously patterned with optic or electronic lithography [Morpurgo et al., 1999] and immersed into an electrolytic solution. By monitoring deposition currents and voltages, the process can be carefully controlled. It can also be turned into a dissolution process by simply changing electrochemical voltage. Defect-free devices that can achieve quantified conductance (at room temperature) and stable switching between two states were obtained with these methods.

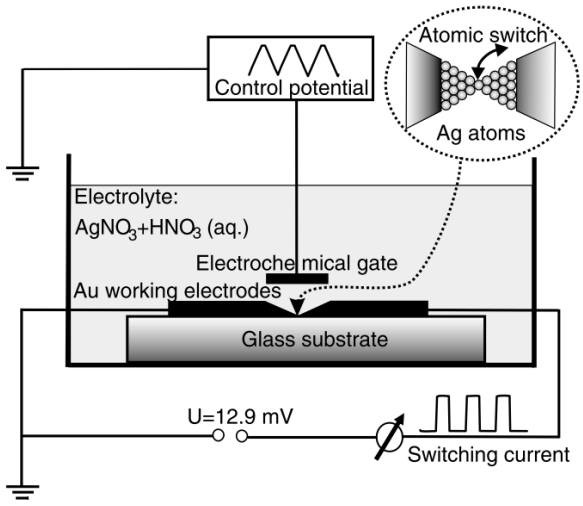

Figure 1.14: Electrochemical setup for making nanogap. This setup was employed the first single-atom transistor. Ref. [Xie et al., 2004].

Fabrication and nanogap control The process described here was used by [Morpurgo et al., 1999]. However, materials and procedures used in the literature may vary a bit from this. The fabrication process is usually split into two steps. First, electrodes are patterned on SiO_2 substrates. In the second step, these electrodes are immersed into an electrolytic solution and metal is deposited, resulting in the gap being narrowed. The first procedure is as it follows: two metal electrodes (Ti/Au, 15/35 nm) are patterned with EBL and lift-off on SiO_2 substrates. The gap between those electrodes is of the order of dozens of nm (40-200nm gaps are reported in the article). However, the gap size is not really important since it will be reduced. To avoid leaking currents, the electrodes are usually covered with a photoresist or SiO_2 except for a small region where metal is deposited [Xie et al., 2004]. After this, samples are placed into an aqueous solution consisting of $KAu(CN)_2$, $KHCO_3$ and KOH. Electrodes are contacted and a voltage V_{ac} (usually an alternative voltage is used in order to prevent an asymmetric deposition) is applied between those two in order to perform conductance measurements. A third (gold) electrode controlling the electrodeposition operation is added, with a control voltage V_{dc} (also referred as gate, since its role can be seen similar to a MOSFET gate). When the voltage of the working electrodes is negative relative to the gate, deposition occurs. $KAu(CN)_2$ accepts an electron and undergo a reduction. A gold atom is then released at the electrode surface. Also, when the gate voltage is reduced, this reduction occurs at this electrode and the deposition

is limited. In the article [Morpurgo et al., 1999], this bias voltage is from -0.5V to 0.6 V. In [Xie et al., 2004], the range is from 0 to 0.3 V. The deposition currents were measured with values of 2 to 3 μA. It resulted in a deposition rate of 1 Å/S.
The gap size is monitored using I-V curves. When electrodes are separated, the monitored current is small and constant (nA). When the gap becomes extremely small, current steps can be observed, corresponding to an atomic contact. In the case of gold atoms, the conductance steps were measured with a value of G_0. Au has indeed one electronic valence state available for conduction (however, steps with 1 G_0 values were also measured with other materials, such as Pb [Xie et al., 2004] and Ag [Xie et al., 2018]. The existence of only one conducting state is not linked to the valence state).
It is also interesting to note that when the contacts are close (below 1 nm) but not touching, tunnelling current regime can be observed. In [Morpurgo et al., 1999], a linear augmentation of current was observed before the contact. This phenomenon was investigated more precisely in [Li et al., 2000]. Stepwise increasing tunnelling current was recorded. An explanation given for these steps was that atomic reconfigurations occur each step of 0.5 Å(which is smaller that the size of an atom) in order to minimize the energy. This result shows that although the gap size cannot be adjusted continuously, an accuracy below the angstrom can be achieved for electrochemical nanogaps.

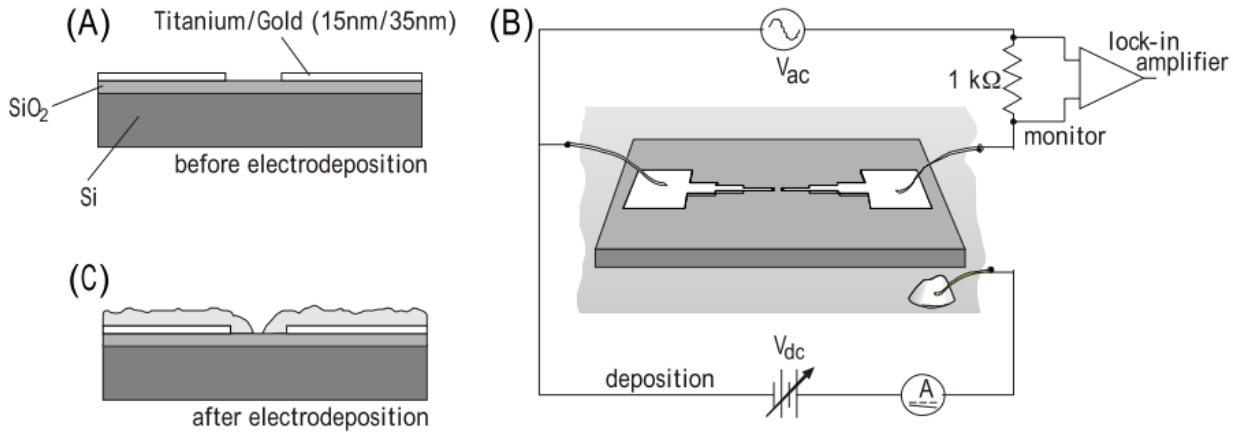

Figure 1.16: Schematic view of experimental setup before a) and after c) electrodeposition on gold electrodes. The electric setup with the different electrodes is illustrated in b). Ref. [Morpurgo et al., 1999].

Bistable configuration and memory A bistable configuration was obtained by several research teams [Xie et al., 2004] [Maul et al., 2012] [Xie et al., 2018], by applying a control voltage. It has been shown that the switching (only the closing ones) events between two conductance states (usually to be between 0 and 1 G_0) are random but correlated. In other words, in a bi-stable configuration, the atoms are preferentially moved along specific pathways

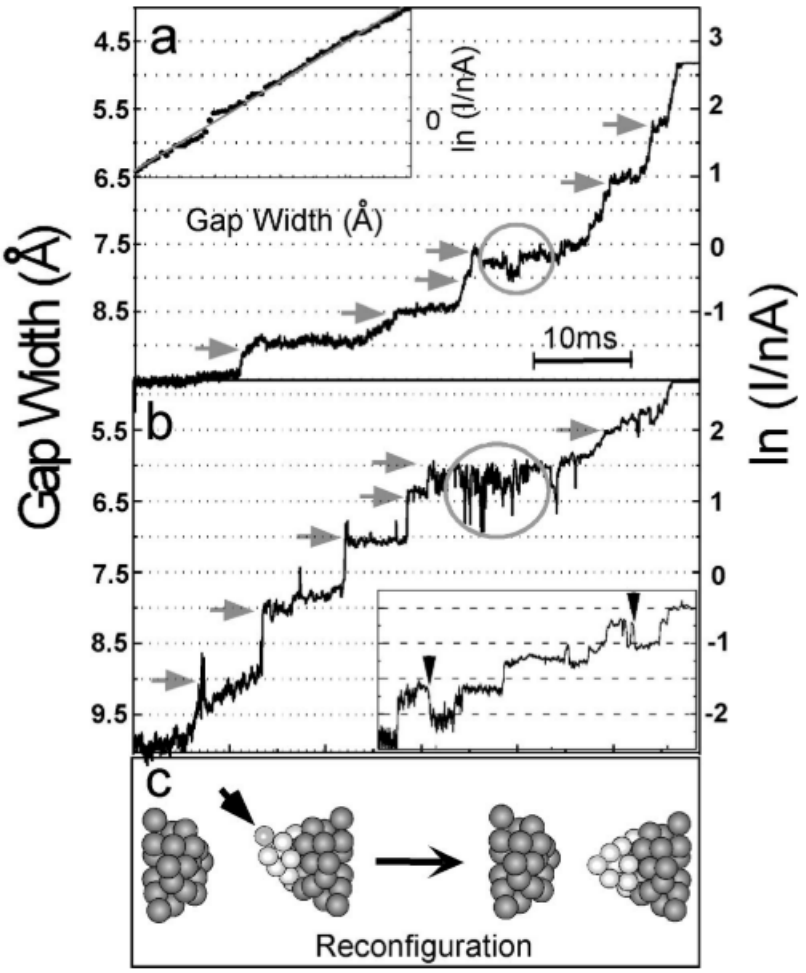

Figure 1.15: a) b) Variation of tunnelling current between two electrochemically deposited Cu electrodes as the gap is reduced linearly with time. It exhibits a step function, each step corresponding to an atomic reconfiguration. Ref. [Li et al., 2000].

due to the influence of electrodes. Subsequent switching events are more likely to follow the same paths. This result obtained by [Maul et al., 2012] was obtained by performing statistical calculations on switching events with an gold nanogap. The closing and opening of an atomic-scale contact involve structural reorganization on the atomic scale. These structural changes of the contact area, in turn, have consequences on the conductance. Thus, to characterize a switching event, the values of the plateaus in the conductance curve are used (fig 1.17). Then, the correlation between two subsequent switching events to observe the same conductance plateau was computed. If the events are uncorrelated, and the atomic switching configurations are random, the function should be constant. However, it was not the case (the plotted correlation function is shown in figure A.17). Simulations (using Gouy-Chapman model) of the atomic recombinations combined to experimental results showed that it exists preferred pathways for atoms, and therefore the correlations can be explained. This result shows that switching events are not instantaneous jumps between two conductance states. It should be taken into account while dealing at high frequencies.

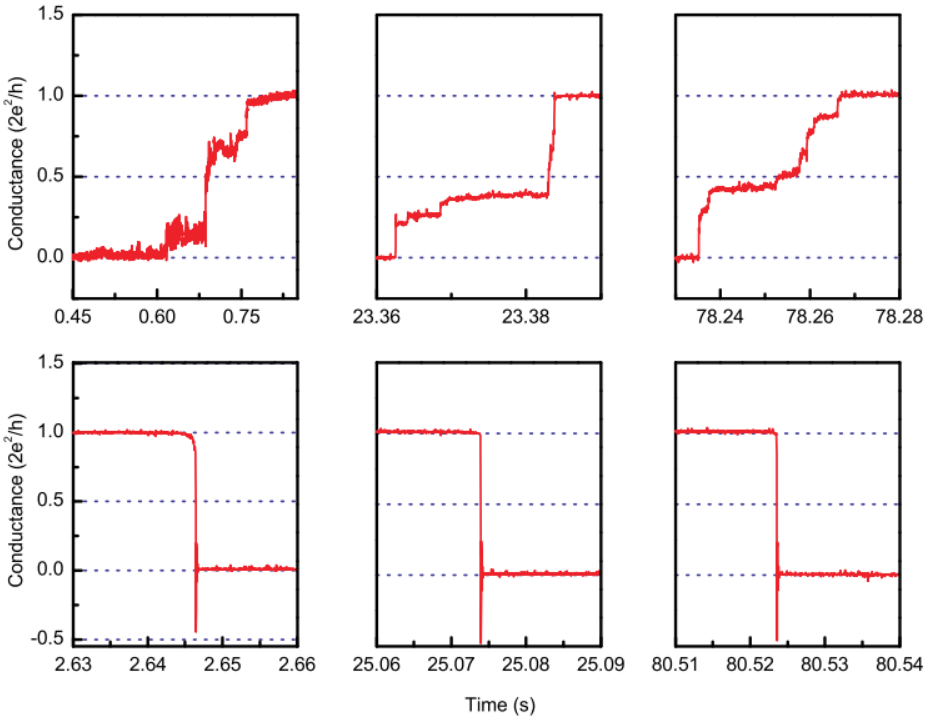

Figure 1.17: Conductance as a function of time for a switching cycle in an electrochemical gold atomic transistor. Ref. [Maul et al., 2012].

Device integration The aqueous solution makes the integration of those switches difficult. It also adds a risk of leakage, and corrosion. However, a quasi-solid state electrochemical switch has been fabricated by [Xie et al., 2018]. It relies on the gelation of pyrogenic silica, and the resulting solid has the diffusive properties of a liquid. The electrodes are therefore "immersed" into a silica-gel $AgNO_3$ + HNO_3. Silica gel is a randomly porous medium with pores of maximum 10 nm, that can contain the electrolyte. It is a well known material, and it is inert. The solid state electrolyte was prepared by mixing an aqueous electrolyte solution with colloidal silicon dioxide. The silica gel can stand freely on the working electrodes with this

process. The performances of the liquid and quasi solid-state atomic transistors were compared in order to understand the influence of gelation. A picture of the quasi-solid state SAT is shown in figure 1.18. Cyclic voltammetry experiments have shown that silica gel is inert. Conductivity measurements have shown that the ionic conductivity of the electrolyte is the same for aqueous and solid phases. However, switching periods are longer for the solid electrolyte (it is illustrated in figure A.31). This is due to the ionic mobility being slower in the solid state ($\approx 10\%$). These devices open perspectives for device integration, since it works at room temperature, is easy to manufacture (thin wires are used as gate electrodes) and avoids the use of a liquid solution.

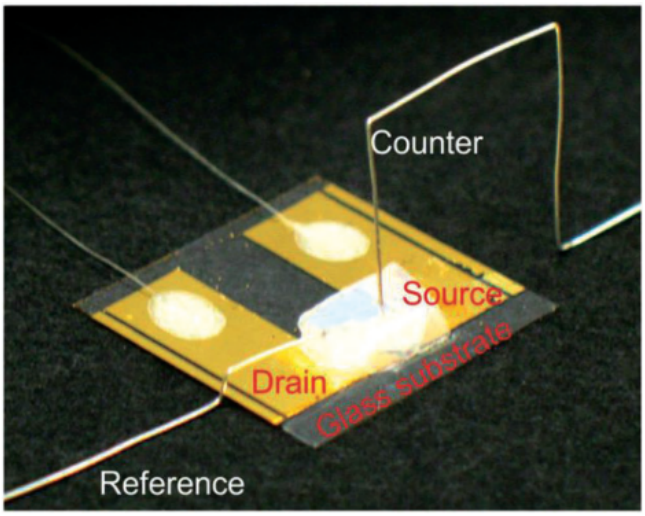

Figure 1.18: Quasi solid state (electrochemical) single atomic transistor. Ref. [Xie et al., 2018].

1.3 Theory

1.3.1 Electronic transport

In this subsection, electronic transport is addressed within the context of a nanosized contact connected to two electrodes acting as reservoirs of electrons. The conduction regime is assumed to be ballistic (i.e. electron-defect scattering is negligible).

Conductance

Electronic conductance is the opposite of the resistance:

$$G = \frac{1}{R} = \frac{I}{U}$$

In the Landauer formalism (which is described in the previous section), the conductance in a 1D nanostructure obeys the equation (1.2). To go deeper into this result, the electron leads[18] have to be defined. The leads are linked to reservoirs. They send electrons and absorbs them with a given chemical potential μ and a temperature T. Transport through a nanostructure can be described as two leads joined by a channel (figure 1.19).

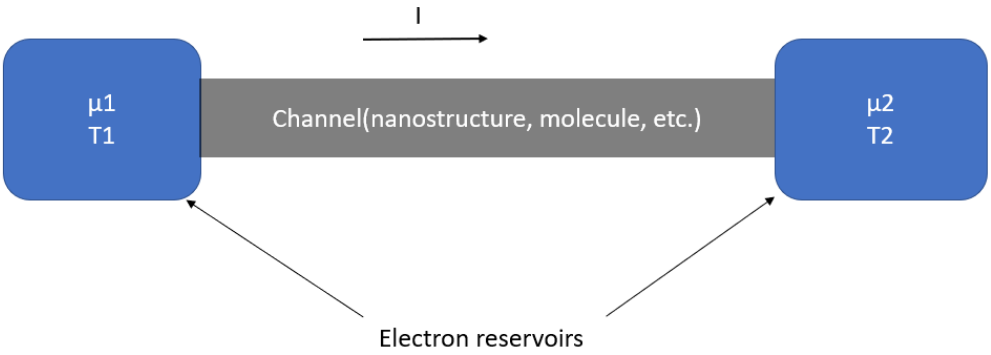

Figure 1.19: Schematic model of the transport through a nanoconstriction. The electron reservoirs are also called "leads".

For a 1D channel, the current can be easily calculated. We start from the formula of the probability current density associated to a quantum state ψ:

$$j_p = \frac{1}{m} \mathrm{Re}\left(\psi^* \frac{\hbar}{i} \nabla \psi\right)$$

With m the mass.

[18] More precisely, leads are structures that allow one to inject currents at fixed voltage [Datta, 1995]. They act as connection between electrodes and the channel. On these leads the electrons propagate as plane waves along the longitudinal direction, while its transverse momentum is quantized due to the lateral confinement. The number of modes going in and out each lead is perfectly defined by quantification. This is an idealization of a perfect conductor.

Then, we consider a plane wave $\psi(x) = \frac{1}{\sqrt{L}}(e^{ikx})$ (with k the wave number) emitted by the right lead towards the left one. A part of the wave is reflected back into the channel with a reflection coefficient r. The wavefunction in the channel is therefore:

$$\psi(x) = \frac{1}{\sqrt{L}}\left(e^{ikx} + re^{-ikx}\right)$$

If one calculate the probability current of this wave using the formula above and multiply it by the elementary charge, the electric current leaving the right lead can be found:

$$j = -e\frac{\hbar k}{mL}\left(1 - |r|^2\right)$$

With m the mass, k the wave number and L the conduction channel length. And by the same way, the electric current flowing into the left lead is:

$$j = -e\frac{\hbar k}{mL}|t|^2$$

With t the transmission coefficient through the channel. Using the current conservation the following relations are found:
$|r|^2 + |t|^2 = 1$
We write $|t|^2 = T$ and $|r|^2 = R$ for more clarity. This result corresponds to the current carried by an electronic mode with a wavenumber k.
The total current in the channel is:

$$j = -\frac{ev_k}{L}T \tag{1.10}$$

with $v_k = \hbar k/m$ the "velocity" of the state k.
To calculate the effective current of all the electronic modes, the energetic state of the lead has to be taken into account. The right reservoir has a chemical potential $\mu_1 = \epsilon_F - eV_1$ and the left one $\mu_2 = \epsilon_F - eV_2$, with ϵ_F being the Fermi level. The left reservoir sends a current of electrons I_1. This current can be calculated using the formula of the current for one electronic mode and summing the currents of all the modes with wavenumbers k, multiplied by the probability of this electronic mode being occupied by an electronic (the Fermi-Dirac distribution $f(E)$). It gives:

$$I_1 = -2e\sum_{k>0}\frac{v_k}{L}T\left(\varepsilon_k\right)f\left(\varepsilon_k + eV_1\right) \tag{1.11}$$

And for the current sent by the second lead:

$$I_2 = -2e\sum_{k<0}\frac{v_k}{L}T\left(\varepsilon_k\right)f\left(\varepsilon_k + eV_2\right) \tag{1.12}$$

The two contributions are summed to get the total current:

$$I = -2e\sum_{k>0}\frac{v_k}{L}T\left(\varepsilon_k\right)\left[f\left(\varepsilon_k + eV_1\right) - f\left(\varepsilon_k + eV_2\right)\right] \tag{1.13}$$

The sum on the wavenumber can be transformed into an integral over the energy:

$$\frac{2}{L}\sum_k \cdots = \int \rho(\varepsilon)d\varepsilon \cdots \tag{1.14}$$

With $\rho(\epsilon)$ is the electronic density of states [19].
After some algebra, the current formula reduces to:

$$I = -\frac{2e}{h}\int_0^\infty T\left(\varepsilon_k\right)\left[f\left(\varepsilon_k + eV_1\right) - f\left(\varepsilon_k + eV_2\right)\right] d\varepsilon$$

At low temperature it becomes:

$$I = -\frac{2e}{h}\int_{\mu_1}^{\mu_2} T(\varepsilon) d\varepsilon$$

For a small tension $V_2 - V_1 \approx dV \leftrightarrow edV = d\epsilon$:

$$G = I/V = eI/d\varepsilon = -\frac{2e^2}{h}\int_0^\infty T\left(\varepsilon_k\right)\frac{\left[f\left(\varepsilon_k\right) - f\left(\varepsilon_k + d\varepsilon\right)\right]}{d\varepsilon} d\varepsilon = -\frac{2e^2}{h}\int_0^\infty T(\varepsilon)\frac{\partial f}{\partial \varepsilon} d\varepsilon$$

At low temperature:

$$G = \frac{2e^2}{h} T\left(\varepsilon_F\right)$$

This famous result is however only applicable in the case of a 1D channel. To go further, the geometry of the channel has to be described with more precision. The channel can be considered as a waveguide of length L and section S. Those parameters control the boundary conditions of the transverse electronic modes that can go through this channel. The electronics states are indeed no longer unidimensional waves but multidimensional ones. If the x axis is parallel to the current, the wavefunction is (in 2D):

$$\psi(x, y) = \sqrt{\frac{2}{LW}} \sin k_y y e^{ik_x x}$$

with k_y the transverse number, determined by the boundary conditions. This 2D wavefunction can be generalised to 3D. Only a finite number of those modes can cross. During the conduction, the modes are mixed. In other words, one electronic mode can be transmitted into another mode. The coefficient of transmission T_{ab} corresponds to this transmission, from a mode a to a mode b. Therefore, after a little algebra using the Landauer formula, one can find:

$$G = \frac{2e^2}{h}\sum_{ab} T_{ab}$$

In the case of an ordered region of conduction, the modes are not mixed and $T_{ab} = \delta_{ab}$. Therefore, the conductance is proportional to the number M of modes transmitted. The conductance is quantized in the units of $G_0 = \frac{2e^2}{h}$, the conductance quantum. This quantization is obtained at low temperatures and/or in small nanoconstrictions such as in atomic/molecular transistors (see previous section). The conductive properties of a channel can be characterized by a "scattering matrix". In the case of a terminal device, this matrix is:

$$S = \begin{pmatrix} s_{11} & s_{12} \\ s_{21} & s_{22} \end{pmatrix} = \begin{pmatrix} r & t' \\ t & r' \end{pmatrix}$$

[19] Here we use the 1D DoS : $\rho(\varepsilon) = \frac{2}{\pi\hbar v(\varepsilon)}$.

where r, t, r', t' are the transmission and reflection coefficients. When multiple conduction channels are present, the matrix can be generalized to higher dimensions. This "multi-channel" description is useful while doing simulations on complex structures. Using the current conservation laws, one can find that the S-matrix is unitary. The reflection $R_{\alpha\alpha}$ and transmission $T_{\beta\alpha}$ matrices can be extracted from the S-matrix:

$$T_{\beta\alpha} = \sum_{mn} T_{\beta\alpha,mn} = \sum_{mn} \left| s_{\beta\alpha,mn} \right|^2 = \mathrm{Tr}\left[s^{\dagger}_{\beta\alpha} s_{\beta\alpha} \right]$$
$$R_{\alpha\alpha} = \sum R_{\alpha\alpha,mn} = \sum \left| s_{\alpha\alpha,mn} \right|^2 = \mathrm{Tr}\left[s^{\dagger}_{\alpha\alpha} s_{\alpha\alpha} \right]$$

The Landauer formula can be linked to the transmission matrix with the formula:

$$G = 2\frac{e^2}{h} \sum_{a,b} \left| s_{ij,ab} \right|^2$$

Where i, j are the indices of the terminals of interest and a, b the indices of the conduction channels. An example of scattering matrix for a multichannel configuration is given in figure 1.20.

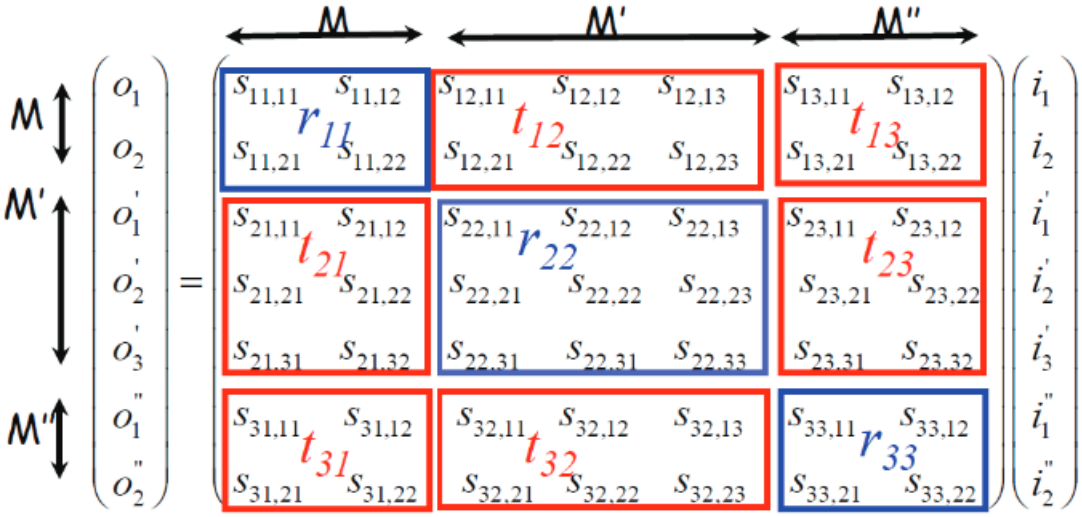

Figure 1.20: Scattering matrix in the case of the multiple terminals and conduction channels. Here, there are 3 terminals. o represents the outgoing currents and i the ingoing currents in each terminal.

Spin

The influence of the magnetic field on the electronic transport (especially for mesoscopic systems) has generated much interest. A new field, spintronics, has emerged with promises of new applications in electronics. In this domain, the spin dependence of the electronic transport in (mostly) ferromagnetic materials is exploited and a new (spin) degree of freedom can be exploited. The point of start was the discovery of giant magnetoresistance (GMR), which is a quantum magnetoresistance effect observed in ferromagnetic multilayers composed of alternating ferromagnetic and non-magnetic conductive layers. This effect induces a massive change in the electrical resistance when the magnetization of the layers changes from parallel to antiparallel

direction (figure 1.21) . The GMR is considered to occur because of spin-dependent scattering. It states that in a magnetically ordered material, electrons with one spin orientation are scattered more strongly than the other ones. To model this phenomenon, the electronic current is usually divided into two parallel conduction channels, each with a different spin direction. Thus, when a current is passing through multiple layers with different magnetization directions, the two spin channels are scattered differently. When the magnetization of those multiple layers is directed in the same direction, the electrons are globally less scattered than in the case of layers with anti parallel magnetization. This is illustrated in figure 1.22.

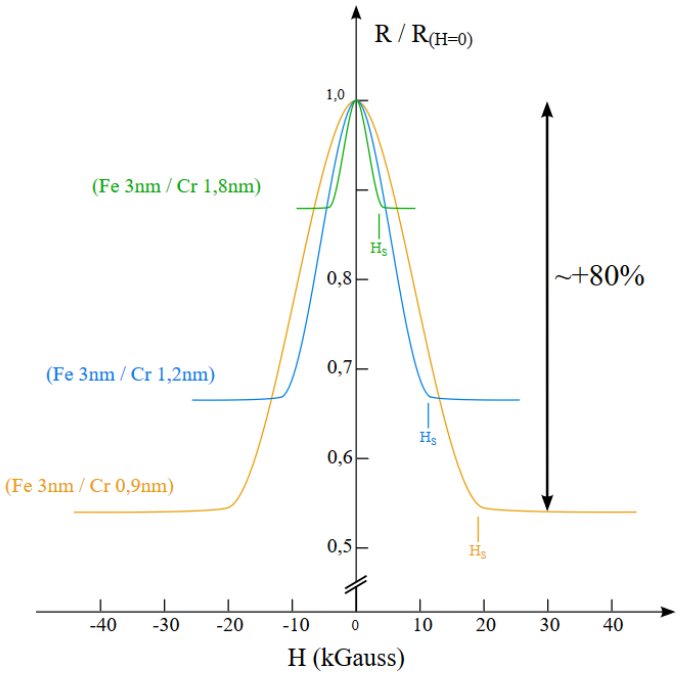

Figure 1.21: Giant magnetoresistance observed in Fe/Cr superlattices. Ref. [Baibich et al., 1988].

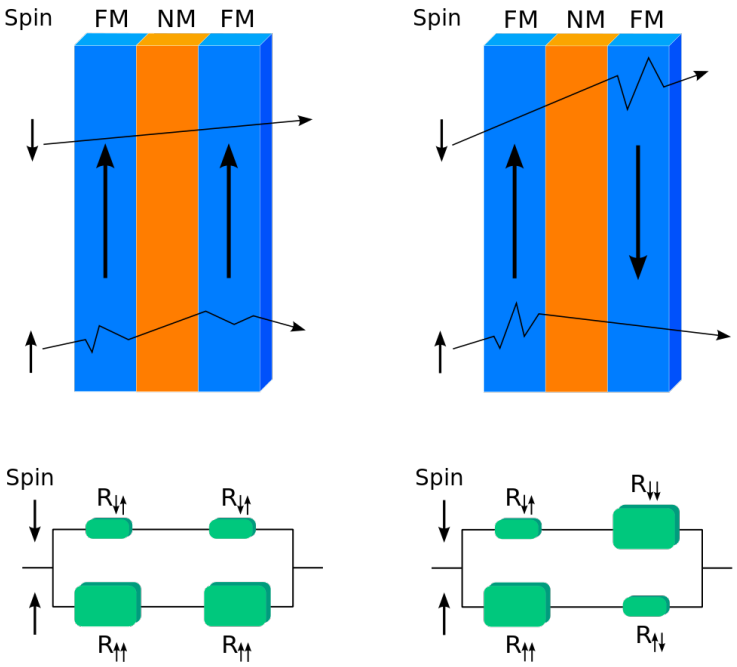

Figure 1.22: Illustration of the GMR effect. Right figure: parallel configuration. One spin channel is thinly scattered while the other is completely scattered. Letf figure: anti-parallel configuration. The equivalent circuit under the figure shows how the overall resistance is affected.

Let us consider the influence of spin on the electronic transport in small nanostructures. In several experiences involving QPC, non integer multiple of G_0 were found as values of conductance. No explanation were found for this anomaly until the electron-electron interactions were considered. Using spin density simulations, the origin of this anomaly was found to be originated from the spin [Akis and Ferry, 2006].

Noise

One of the main characteristic of a nanoscale electronic system is shot noise. It consists of fluctuations of electric current, due to the current being made of discrete charge carriers. It can be modelled as a Poisson process. The electronic modes (as said before) have indeed a non-zero probability τ_n to be transmitted [Blanter and Büttiker, 2000]. This is illustrated in figure 1.23. First, a general expression for noise has to be defined. It can be stated as the fluctuation of current away from its average value:

$$\Delta I_\alpha(t) \equiv I_\alpha(t) - \langle I_\alpha \rangle$$

We define two leads, α and β and introduce the correlation function between the currents in leads α and β:

$$S_{\alpha\beta}\left(t - t'\right) \equiv \frac{1}{2}\left\langle \Delta\hat{I}_\alpha(t)\Delta\hat{I}_\beta\left(t'\right) + \Delta\hat{I}_\beta\left(t'\right)\Delta\hat{I}_\alpha(t)\right\rangle$$

Taking the Fourier transform of this expression, the noise power spectrum is obtained:

$$S_{\alpha\beta}(\omega) = \frac{1}{2}\int \mathrm{e}^{\mathrm{i}\omega t}\left\langle \Delta\hat{I}_\alpha(t)\Delta\hat{I}_\beta(0) + \Delta\hat{I}_\beta(0)\Delta\hat{I}_\alpha(t)\right\rangle \mathrm{d}t \tag{1.15}$$

In Landauer formalism, the current can be expressed as a function of the creation and annihilation (respectively) operators: $a^\dagger_{m\alpha}(\varepsilon)$ and $a_{m\alpha}(\varepsilon)$. They create (annihilate) an ingoing electron with m in the lead α with energy ε. The same operators are introduced, but acting on outgoing electrons: $b^\dagger_{m\alpha}(\varepsilon)$ and $b_{m\alpha}(\varepsilon)$. They are linked by the scattering matrix introduced in the previous section 1.3.1:

$$b_{m\alpha} = \sum_{n\beta} \left(\hat{s}_{\alpha\beta}\right)_{mn} a_{n\beta}$$

The population on incoming modes in a reservoir can be expressed in terms of those operators:

$$\left\langle a^\dagger_{m\alpha}(\varepsilon) a_{n\beta}(\varepsilon)\right\rangle = \delta_{mn}\delta_{\alpha\beta} f_\alpha(\varepsilon)$$

The second member of the equality is the consequence of the perfected coupling between the reservoirs and the leads [20], with $f_a(\varepsilon)$ being the Fermi-Dirac distribution in the lead. The current in lead α can therefore be expressed as a difference between incoming and outgoing modes:

$$I_{m\alpha} = \frac{2e}{h}\int_{-\infty}^{\infty} \mathrm{d}\varepsilon \left[\left\langle a^\dagger_{m\alpha}(\varepsilon) a_{m\alpha}(\varepsilon)\right\rangle - \left\langle b^\dagger_{m\alpha}(\varepsilon) b_{m\alpha}(\varepsilon)\right\rangle\right]$$

If the problem is time-dependent, one can use a Fourier transform $\varepsilon \longrightarrow t$:

$$\hat{I}_\alpha(t) = \frac{2e}{h}\sum_m \int \mathrm{d}\varepsilon \mathrm{d}\varepsilon' \mathrm{e}^{\mathrm{i}\left(\varepsilon-\varepsilon'\right)t/\hbar}\left[a^\dagger_{m\alpha}(\varepsilon) a_{m\alpha}\left(\varepsilon'\right) - b^\dagger_{m\alpha}(\varepsilon) b_{m\alpha}\left(\varepsilon'\right)\right] \tag{1.16}$$

Using properties of the operators and combining 1.16 and 1.15, we can find an expression for the power shot noise at zero frequency in one lead:

$$\begin{aligned} S_{11}(0) =& \frac{2e^2}{h}\int \mathrm{d}\varepsilon \Big\{ \mathrm{Tr}\left[\hat{t}^\dagger(\varepsilon)\hat{t}(\varepsilon)\hat{t}^\dagger(\varepsilon)\hat{t}(\varepsilon)\right]\left[f_1\left(1-f_1\right)+f_2\left(1-f_2\right)\right] \\ &+ \mathrm{Tr}\left[\hat{t}^\dagger(\varepsilon)\hat{t}(\varepsilon)\left(\hat{I}-\hat{t}^\dagger(\varepsilon)\hat{t}(\varepsilon)\right)\right]\left[f_1\left(1-f_2\right)+f_2\left(1-f_1\right)\right]\Big\} \end{aligned}$$

With $\hat{t}$ being the transmission operator/matrix (sub-matrix of the scattering matrix, see section 1.3.1). f_1 and f_2 are respectively the Fermi-Dirac distribution in the leads 1 and 2. If we consider t to be eigenmatrix for each mode n and the transmission probability $\tau_n = \hat{t}^\dagger(\varepsilon)\hat{t}(\varepsilon)$, the expression can be rewritten as [Büttiker, 1992]:

$$\begin{aligned} S_{11}(0) =& \frac{2e^2}{h}\sum_n \int \mathrm{d}\varepsilon \Big\{ \tau_n(\varepsilon)^2\left[f_1\left(1-f_1\right)+f_2\left(1-f_2\right)\right] \\ &+\tau_n(\varepsilon)\left[1-\tau_n(\varepsilon)\right]\left[f_1\left(1-f_2\right)+f_2\left(1-f_1\right)\right]\Big\} \end{aligned}$$

Since the variation of τ as a function of energy requires much higher energy scales than the Fermi energy and the voltage, one can assume τ to be constant, evaluate it at Fermi energy and perform integration. It yields to:

$$S_{11}(0) = \frac{2e^2}{h}\left[2k_\mathrm{B}T\sum_n \tau_n^2 + eV\coth\left(\frac{eV}{2k_\mathrm{B}T}\right)\sum_n \tau_n\left(1-\tau_n\right)\right]$$

[20] i.e. the modes in the reservoir are perfectly transmitted into the leads.

One can see that the power spectrum of the shot noise is equal to $S_{11}(0) = \frac{2e^2}{h}\left[2k_{\mathrm{B}}T\sum_n \tau_n^2\right]$ if the transmission probability is either 1 or 0. It corresponds to the minimum of the shot noise. It is also important to notice that the noise is directly proportional to temperature.

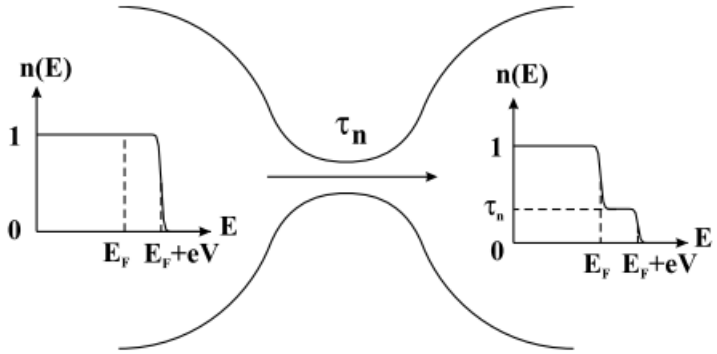

Figure 1.23: Schematic explanation of the shot noise in a ballistic quantum point contact. V is the voltage across the junction, τ the transmission probability, n(E) is the distribution function of the transmitted state. The presence of a probability of transmission leads to fluctuations in the current. Ref. [Agrait et al., 2003].

Measurements of shot noise have direct applications: determination of the mean free path, observation of charge carriers $\frac{e}{3}$ in the Quantum Hall regime, thermometry (see the dedicated section), etc. [Naveh, 1998]. This shot noise has been observed and the observations were consistent with the theory. It is illustrated in figure 1.24.

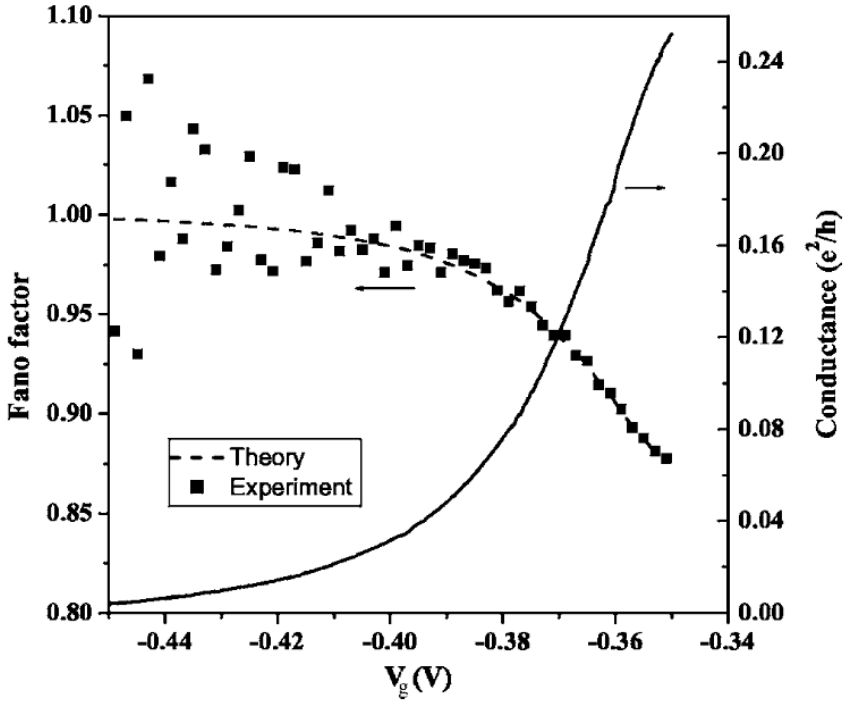

Figure 1.24: Shot noise as a function of gate voltage in a GaAs/AlGaAs heterostructure. The Fano factor corresponds to the spectral noise power divided by $2eI$. Ref. [Chen and Webb, 2006]

Simulation

In order to simulate systems similar to atomic transistors, nanogaps, QPC, etc., multiple techniques are employed. Landauer formalism is widely used to simulate mescoscopic systems. The simulations focus on computing s-matrix and transmission. Also, when dealing with atomic-sized contacts under constraints, molecular dynamics, tight-binding and density functional theory are used. These techniques enable the simulation of the behaviour of sets of atoms under certain constraints. It is indeed useful to simulate the atomic configuration of nano-sized contacts while using techniques to modify them (MBJ, electromigration, electrochemical techniques, etc).

Kwant Kwant is a free Python package designed for quantum transport simulations, relying on tight-binding [21], scattering and Landauer-Buttiker models. Kwant works with user-build scattering geometry, connected to infinite leads (figure 1.25); this geometry is a scattering zone and various quantities can be calculated: conductance, noise, s-matrices, wavefunctions, electronic density, etc. The leads act as infinite waveguides that carry plane waves into the scattering region. The Hamiltonian of this scattering region has the form:

$$\hat{\mathbf{H}} = \sum_{i,j} H_{ij} c_i^\dagger c_j = \sum_{i,j} H_{ij} |i\rangle\langle j|$$

With i, j being the indices of different degrees of freedom of the system, $c_i^\dagger c_i$, the creation and annihilation operators of an electron on the site i. Those degrees correspond to the position r

[21] On the tight-binding model, the atoms are assumed to have only one orbital [Majidi, 2018].

of a site multiplied by the internal degrees of freedom of each site (spin, atomic orbital, etc). The sites correspond usually to an atom or a molecule. H_{ij} is an infinite hermitian matrix determined by the properties of the sample. This matrix can be expressed as a sum over all the Hamiltonian fragments:

$$\hat{H}_{rr'} = \sum_{\alpha\alpha'} H_{r\alpha r'\alpha'} |r\alpha\rangle \left\langle r'\alpha' \right|$$

With α being the label of internal degrees of freedom. Each edge between r and r' sites leads to a non-null matrix element $H_{rr'}$.

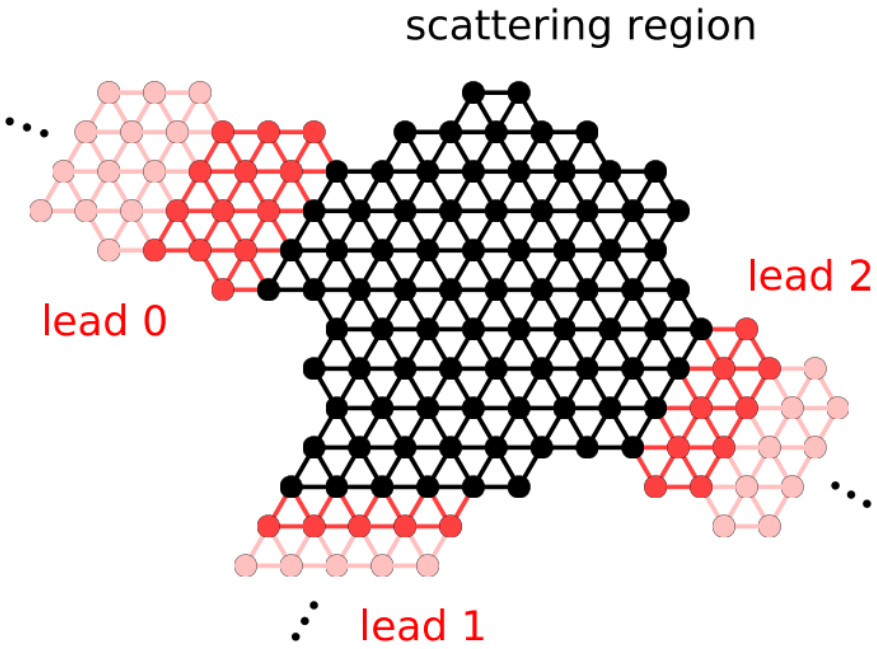

Figure 1.25: Example of a system generated with kwant to perform transport simulations. Black dots represent the sites of the scattering region, while red ones represent the sites of the leads (infinite waveguides that inject or received electronic plane waves). Ref. [Groth et al., 2014]

The scattering problem is formulated using electronic wavefunctions. The Hamiltonian matrix has the triangular form:

$$H = \begin{pmatrix} \ddots & V_L & & \\ V_L^\dagger & H_L & V_L & \\ & V_L^\dagger & H_L & V_{LS} \\ & & V_{LS}^\dagger & H_S \end{pmatrix} \tag{1.17}$$

H_L is the Hamiltonian of one unit cell of the lead, V_L is the Hamiltonian connecting two cells of the lead, H_S is the large scattering Hamiltonian and V_{LS} is the Hamiltonian connecting the leads and the scattering region. The wavefunction of this system is defined as $\left(\ldots, \psi^{\mathrm{L}}(2), \psi^{\mathrm{L}}(1), \psi^S\right)$, with ψ^S is the wavefunction of the scattering region, and $\psi^L(i)$ is the w.f. in the i-th unit cell away from the scattering region. The wave functions in the lead are, as said previously, linear

combination of plane waves. The eigenstates of the translation operator in the leads have the form:

$$\phi_n(j) = (\lambda_n)^j \chi_n$$

The obey the Schrodinger equation:

$$\left(H_L + V_L\lambda_n^{-1} + V_L^\dagger\lambda_n\right)\chi_n = E\chi_n$$

with χ_n the n-th eigenvector, and λ_n the n-th eigenvalue,with the form $\lambda_n = \mathrm{e}^{\mathrm{i}k_n}$. n is the mode number with a momentum of k_n. The scattering states in the leads are:

$$\psi_n(i) = \phi_n^{\text{in}}(i) + \sum_m S_{mn}\phi_m^{\text{out}}(i) + \sum_p \tilde{S}_{pn}\phi_p^{\text{ev}}(i)$$

and inside the scattering region:

$$\psi_n(0) = \phi_n^S$$

Finally, the main outputs of kwant are the scattering matrix S_{nm} and the wave function $\psi_n(0)$. They are computed by solving the equation:

$$H\psi_n = \varepsilon\psi_n$$

With H given by eq. 1.17. With those quantities, other values can be easily computed such as:

- Charge and current density
- Conductance (using the Landauer formula)
- Shot noise
- Spin currents, etc

One may ask how the Hamiltonian is defined. They are mainly defined by the user. The user can define *onsite* Hamiltonian which corresponds to the H_{rr} and the *hopping* which corresponds to $H_{rr'}$ for two neighbour sites. The Hamiltonian matrix is then built by the module *builder*. Usually the hopping term is an energetic value corresponding to the *hopping integral*. This hopping integral is defined[22]for some lattices and corresponds to H_{ij}. Redefining the Hamiltonian allows also one to include external influences and simulate complex systems, such as superconductors, doped semiconductors, Quantum Hall regime, etc.

[22]It can be calculated or simulated [Majidi, 2018].

Other methods

Density functional theory Density functional theory (DFT) computes the ground state of systems with several exchange correlation functions acting in the Hamiltonian part of the corresponding Schrodinger's wave equation. It is used in calculating defect formation energies in solids, formation enthalpy of compounds and materials as well as surface energies of various crystallographic planes of crystals. The calculations are more accurate for ground states rather than for excited ones. DFT deals with the electrons in the given system and as a consequence the number of degrees of freedom involved is much higher. Various approximations such as local density and generalized gradient approximations are used to model exchange-correlation functions. Computationally it is an expensive method. It is also used to calculate the atomic structure of atomic-sized contacts.

Molecular dynamics Molecular dynamics (MD) methods treat atoms as classical particles. It uses standard potentials to compute the dynamical evolution of the system until equilibrium. This method is useful when dealing with a large number of atoms, since it is not computationally expensive compared to other methods.

1.3.2 Heat transport

Dissipation and thermoelectricity

Heat current and thermal conductivity: generalities We consider a nanoscale junction with two leads/electrodes/reservoirs at two different temperature (difference ΔT). We introduce the thermal current density j_{th} and the thermal conductance σ_{th}. In the linear regime of heat transport:

$$j_{th} = -\kappa \nabla T \tag{1.18}$$

and

$$\sigma_{th} = -\lim_{\Delta T \to 0} \frac{J_{th}}{\Delta T} \tag{1.19}$$

Where κ is the thermal conductivity [23]. The thermal energy can be carried through a nanojunction through lattice vibrations (phonons) and/or electrons[24]. Various theoretical methods are commonly employed to describe energy/heat flow. One is the single-particle scattering approach [Dubi and Di Ventra, 2011]; in this model, the particles are assumed to be non-interacting, and the current is simply proportional to the probability of a phonon or an electron to cross the channel [25]. Other techniques are used, such as relying on Density functional theory [Meir and Wingreen, 1992] or molecular dynamics[Wang et al., 2008] to take the interactions between the lattice and electrons into account .

[23] For an uniform sample with length L and cross section a, the relation between κ and σ is $\sigma_{th} = (A/L)\kappa$. The analogy with electric currents is obvious.

[24] $\kappa_{phonons}$ has the approximate form:$\kappa \approx \frac{1}{3} l v c_v$ when l the phonon mean-free path, c_v the heat capacity of phonons and v the speed of sound.

[25] For phonons, the expression of the thermal current is $J_{th} = \int_0^\infty \frac{d\omega}{2\pi} \hbar\omega \mathcal{T}(\omega) (g_L - g_R)$ with $\tau(\omega)$ the transmission coefficient and $g_{L(R)}$ the Bose-Einstein distribution in the leads.

Heat dissipation To consider the local heat dissipation, the local temperature has to be defined, since it is a complex thermodynamic quantity. Three local definitions are reported here:

- *Kinetic definition*: Local temperature related to the kinetic energy of the ions: $\left\langle (1/2)mv^2 \right\rangle \sim 3k_BT/2$. However, it does not consider the quantum effects and an average kinetic energy has to be defined over a length scale, which is conflicting with the quantum nature of particles.
- *Local phonon mode*: a local phonon mode of pulsation ω_0 is considered to be adiabatically coupled to the system. It has been shown that over a voltage bias V_0 such as $eV_0 = \hbar\omega_0$, local heating starts [Galperin et al., 2009]. The temperature is therefore defined by the phonon mode temperature.
- *Distribution function definition*: It also relies on a phonon model coupled to the system but the temperature is determined by comparing the distribution function of the mode to an equilibrium distribution at a given temperature. However, differences between equilibrium and non equilibrium functions may be significant, especially at low bias voltages [Galperin et al., 2007].
- *Dissipated power*: The power dissipated into the junction is commonly assumed to be $\sigma_{th}T^4$. Using DFT and perturbation theory, the power dissipated into the junction by current-carrying states is computed. The local temperature can therefore be extracted using estimated values of σ_{th} [Chen et al., 2005].

While under an electric current, the nanonjunction is the siege of several heating phenomena. The first one is the *ionic heating*. The power of the entire circuit is classically defined: $P = \frac{V^2}{R}$, and a fraction of this power α [26] is dissipated into ionic degrees of freedom due to electron-phonons coupling. However, since the phonon mode spectrum is discrete, there is a voltage threshold V_c required to excite the ground phonon mode. The power dissipated can be written as [Todorov, 1998]: $P = \Theta(V - V_c)\alpha V^2/R$ where Θ is a step function. Also, this power is not fully transmitted onto the lattice and there is a heat current I_Q that transmits a part of this power to the leads. Since the leads are much bigger than the junction itself, one can assume that this heat is dissipated entirely at a a classical rate $I_Q = \sigma_{th}T_{eff}^4$ into those leads. Thus, at steady state, $I_Q = P$:

$$T_{\text{eff}} = \Theta\left(V - V_c\right)\left(\frac{\alpha}{\sigma_{th}R}\right)^{1/4}\sqrt{V} \tag{1.20}$$

However, those expressions are valid under the hypothesis of the leads being perfectly thermally connected to the junction. Bad coupling of the leads or the existence of local phonon modes [27] may cause the temperature to reach high values (1000 K !).
Electrons have a temperature as well. This electronic temperature is defined as the temperature T_e of the Fermi sea[28] of the electrons. This temperature depends on electron-electron interactions and electron-phonon coupling. Under the same hypothesis as for the ionic heat, *D'Agosta et al.*[D'Agosta and Ventra, 2006] have found this relationship:

$$T_e = \gamma_{e-e}V$$

[26] This coefficient is calculated in [Todorov, 1998].
[27] Weakly coupled to the phonon modes of the leads.
[28] General mathematical description of the electrons in a gas at low temperature [D'Agosta and Ventra, 2006].

With γ_{e-e} a coefficient determined from microscopic calculations, depending on the strength of $e^- - e^-$ interactions.
The two combined processes listed above take place at the same time. Therefore, the influence of the electronic temperature on the ionic one can be considered. Since the total power dissipated in the junction is finite, this power should be split between those two phenomena. Thus, the energy used for electronic heating is no longer available for ionic heating. The expression for the effective ionic temperature in presence of those two effects is (using the same assumptions than before):

$$T_{\text{eff}} = \left(T_0^4 + \gamma_{e-ph}^4 V^2 - \gamma_{e-e}^4 V^4\right)^{1/4}$$

It means, that with sufficient voltage values, the phonons cool down. It was observed experimentally (fig A.18). Another idea of cooling is to use thermoelectricity and the Peltier effect. Briefly, it consists in using electrons to transmit heat from a hot source to cold one, using a voltage. It results in the cooling of the leads, and in all the junction, by conduction. Thermoelectricity is covered in the next paragraph.

Thermoelectricity Thermoelectricity consists in a temperature difference leading to a potential difference (and a charge current). Two leads at temperatures T_L and T_R ($\Delta T = T_R - T_L$) are considered here. This effect is used in thermoelectric generators [29]. The thermopower S characterises this effect:

$$S = -\left.\frac{\Delta V}{\Delta T}\right|_{I=0}$$

The thermoelectric merit of figure of a material characterizes the effectiveness of a material to be used as a thermoelectrical generator: $ZT = \frac{GS^2}{\sigma_{th}/T}$ with T, the temperature of the system, σ_{th}, the thermal conductivity of the material and G the electrical conductivity. Thermoelectric effects lie in the fact that the gradient of temperature induces a chemical potential μ gradient, and therefore hot electrons are pushed to travel from hot areas to cold ones. This effect has been observed in nanoscale junctions ([Scheibner et al., 2005] [Scheibner et al., 2007]). The results obtained by those experiments can be explained with the single-particle theory of thermopower. This theory is partially based on the Landauer formula that links current and transmission $\tau(\varepsilon)$:

$$I = \frac{e}{\pi\hbar}\int_{-\infty}^{\infty} d\epsilon \mathcal{T}(\epsilon)\left[f_L(\epsilon) - f_R(\epsilon)\right]$$

with $f_{L(R)}$ the Fermi-Dirac distribution in the left(right) lead. In the limit of small bias and temperature gradient: $|\Delta T| \ll T$ and $|e\Delta V| \ll \mu$. The Fermi-Dirac distribution can therefore be developed in series at first order:

$$f\left(\epsilon, \mu_i, T_i\right) \simeq f(\epsilon, \mu, T) \pm \frac{df}{d\epsilon}\left(\mu - \mu_i\right) \mp \frac{df}{d\epsilon}(\epsilon - \mu)\frac{(T_i - T)}{T}$$

If one injects this expression into the current expression, the terms ΔT and $e\Delta V$ appear in the equation. After setting the current to 0 and isolating S we have:

$$S(T) = \frac{1}{eT}\frac{\int_{-\infty}^{\infty} d\epsilon \mathcal{T}(\epsilon)(\epsilon - \mu)\left[-f'(\epsilon)\right]}{\int_{-\infty}^{\infty} d\epsilon \mathcal{T}(\epsilon)\left[-f'(\epsilon)\right]} \tag{1.21}$$

[29] The Peltier effect is the opposite. A hot lead is cooled by an electrical potential difference which leads to a transfer of hot electrons from the hot lead to the cold one.

This expression can be simplified in the low-temperature limit and by using the Sommerfeld expansion to first order around $\mu(T=0)=\epsilon_F$ one can simplify the integrals and gets:

$$S = \frac{\pi^2}{3}\frac{k_B}{e}k_B T \frac{d\ln[\mathcal{T}(\epsilon)]}{d\epsilon}\bigg|_{\epsilon_F} \tag{1.22}$$

The interpretation of this formula and this development is that the thermal difference leads to a difference between the Fermi-Dirac distribution in the leads. Therefore, this disequilibrium of states leads to an electric field. This model has however some limitations. First one is that it does not take interaction between electrons into account (or only at mean field)[Vignale and Di Ventra, 2009]. The second one is that it gives wrong results when the leads and the junction are poorly coupled.

Thermometry

Various techniques have been developed to measure temperature[30] in nanojunctions. The sample size and the accuracy required are challenges to overcome in order to accurately measure temperatures. Scanning probe methods are most frequently used in mesoscopic physics and this section will focus on them. Optical methods are also used. It also exists on-chip thermometers directly joined to the sample. One must distinguish between two kind of thermometers: the primary ones, that require no calibration (but they are rare and difficult to operate) and the secondary ones that require calibration at a known temperature.

On-chip methods It relies on the fact that tunnelling characteristics through a barrier of two conductors with different electronic densities of states are proportional to temperature. A M quantity depending on the electronic energy distribution function is measured and linked to temperature [Giazotto et al., 2006].

- NIS thermometer: tunnel junction between a normal metal and a superconductor. The temperature can be extracted using the I-V curves.
  $I(V) \propto \int_{-\infty}^{\infty} N_S(E)\left[f_{\mathrm{N}}(E-eV) - f_{\mathrm{N}}(E+eV)\right] dE$ [31]
- SIS thermometer: tunnel junction between two superconductors. The value of the critical current in the junction depends on the temperature.
  $I_c = (\pi\Delta/2eR_{\mathrm{T}})\tanh\left(\Delta/2k_BT\right)$ [32]
- SNS thermometer: the sample is placed between two superconductors. The supercurrent is therefore flowing into the sample. One has to be careful to geometric parametric since the superconducting coherence length ξ_0 has to be far greater than the junction size L. The critical current is as follows.
  $I_c = c\,(k_BT)^{3/2}\exp(-\sqrt{2\pi k_BT/E_T})/\left(eR_N\sqrt{E_T}\right)$ [33]

[30] Especially local temperature.
[31] $f_N(E)$ is the Fermi-Dirac distribution and $N_S(E)$ is the density of states.
[32] Δ is the gap between electrons and Cooper pair state and R_T is the tunnel resistance.
[33] $E_T = \hbar D/L^2$

- Coulomb blockade thermometer: Coulomb blockade is a phenomenon occurring at low temperature in single electron transport (usually in quantum dots) which blocks the current at low voltages due to the charging energy of single electrons. This thermometers acts in an intermediary regime, when temperature is in competition with the charge energy for the control of transport. The temperature can be extracted from the width of the dip in the conductance-voltage curves: $V_{1/2} \simeq 5.439 N k_B T/e$
- Shot-noise thermometer: This thermometer is based on the shot noise (see section 1.3.1). The temperature is extracted from the noise spectral power: $S_1(T) = 2eI \coth\left(\frac{eV}{2k_BT}\right)$.

Scanning probe methods Utilisation of scanning probe for characterization purposes is in constant evolution due to the progress in nanomanufacturing techniques. The (relatively simple) scanning probe method relies on the heat transmission between a probe and a sample. The probe (which is usually a tip) and the sample can be in contact or separated from a small distance. When the tip is in local equilibrium with the sample, the local temperature can be extracted by various methods: thermocouples [Majumdar, 1999], resistive thermometry[Menges et al., 2016], SQUID (superconducting quantum interferometer)[Halbertal et al., 2016], etc. To access an accurate thermal imaging, several parameters have to be controlled. The main ones are the thermal and spatial properties of the probe. The thermal resistance R_T of the tip has to be exactly known to ensure precise measured values [Menges et al., 2016]. Also, when in contact, a tip-sample resistance R_{TS} whose value is generally unknown, appears. The heat flux is, in those conditions, assumed to be

$$\left(\dot{Q}_{\mathrm{ts}} = \left(T_{\mathrm{sensor}} - T_{\mathrm{sample}}\right)/R_{\mathrm{ts}}\right)$$

At nanoscale, scanning thermal microscopes (SThM) measure this flux (or quantities related to it) [Menges et al., 2016]. However, the results are influenced by this contact resistance, which, to add difficulty, is not homogeneous over the sample. Methods to overcome this challenge have been developed, such as two-pass methods [Menges et al., 2012] or dynamic adjustment of the probe temperature [Hwang et al., 2014], but there are difficult to implement and lead to no significant results when dealing with an inhomogeneous sample. *Mendes et al.*[34], have found a method to eliminate the influence of R_{ts} using an AC current [35] to modulate the temperature of the sample: $T_{sample} = T_{RT} + \Delta T_{sample}(1 + sin(2\omega t))$ with T_{RT} being the room temperature. Using this modulation, one can extract the value of R_{TS} and finally the sample local temperature. This method has achieved sub-10 mK and nanometer spatial scale resolutions and it can be used at all temperatures. However, it has also limitations, since it requires a method to tune the sample temperature with a given sinusoidal frequency.
However, resistive and thermocouple thermometers do not work at cryogenic temperatures, as well as optical methods. tSOT (SQUID On a Tip) techniques [Halbertal et al., 2016] enable to perform local temperature measurements at ultralow temperatures. In this method, a SQUID[36] (superconduncting junction) is fabricated on the apex of a sharp tip. It relies on the linear dependence of the current flowing into the superconducting tip with temperature (figure A.19). In this case, the problem of the thermal contact resistance is still present. A condition for

[34] Using resistive thermometry.
[35] One has to note that it works for a limited range of frequencies $\approx 10kHz$.
[36] Superconducting QUantum Interference Device. It is usually used as a magnetic ultra precise sensor.

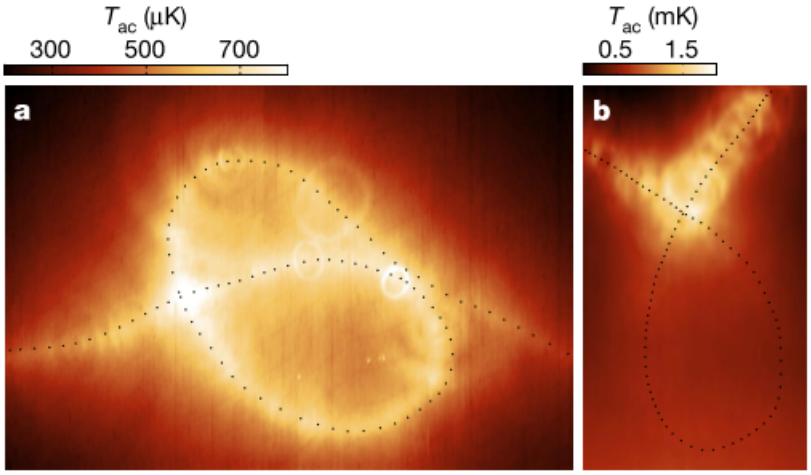

Figure 1.26: Thermal imaging of carbon nanotubes using tSOT technique. Ref. [Halbertal et al., 2016]

an accurate temperature measurement is that this resistance must be lower than the thermal resistance of the sensor itself. This is easily achieved in the superconductive state, since there is no heat conductivity assumed by the electrons and the phonon thermal conductivity is limited due to the geometry of the sample. With this method, *Halbertal et al.* have achieved a spatial resolution of the order of the nanometer and a thermal resolution below the mK. Thermal dissipation of localized electronic states in graphene were observed and imagery of carbon nanotubes (figure 1.26) and quantum dots were achieved using this method.

Optical methods Those methods mainly consist in measuring radiation emitted by the sample. This radiation can be linked to the quantum energetic configuration of the sample and therefore to temperature [Brites et al., 2012].

- Raman spectroscopy: it relies on the inelastic scattering of monochromatic light within the sample. The frequency of the light is slightly shifted as a function of the molecular configuration of the material. Two Raman phenomena can be distinguished: the Stokes and the Anti-Stokes scattering. They correspond respectively to the creation and annihilation of a phonon. From the frequency of the corresponding peaks $\omega_{S(AS)}$ and their intensity $I_{S(AS)}$, one can extract the temperature : $\frac{I_S}{I_{AS}} = \left(\frac{\omega_S}{\omega_{AS}}\right)^4 e^{\frac{\hbar\omega}{k_B T}}$. It has a spatial resolution of 1 μm and a temperature resolution of 1 K.

- Thermoreflectance: it uses the temperature dependence of the reflection coefficient of a material (its refractive index is temperature dependent). It has a sub-micrometer resolution and 0.01K temperature resolution. However, the resolution is limited by the diffraction limit and it requires a calibration.

- Infrared thermography: it is based on the general principle of blackbody radiation. It has a low resolution (10 μm) and the accuracy depends on the "quality" of the blackbody radiation i.e. all bodies are not blackbodies.

1.4 Applications of single-molecule transistors to quantum computing

Quantum computing is a newly emerging field and has a attracted a lot of interest. The computational power perspectives promised by quantum computers are immense. In 2019, Google has announced to have reached the "quantum supremacy", which is the ability for a quantum computer to realize in few seconds what a classical supercomputer would do in an immense amount of time [Arute et al., 2019] (the Google Sycamore takes 200 seconds while a classical computer would have taken 10 000 years). This perfected quantum computer uses superconducting qubits to realize its operations. The architecture and programming of quantum computers algorithms are complicated matters, which are way beyond the scope of this thesis. The focus will be on the generation and the control of qubits, which are the mandatory and most difficult tasks in designing a quantum computer. We focus here on the use of single-molecule transistors (or more generally, single-molecule three-terminal devices) to tune and control nuclear spin qubits.

1.4.1 An example of single molecule spin qubit transistor

We refer to the experiment of [Thiele et al., 2014]. Using a molecular transistor made up of a $TbPc_2$ molecule connected to source and drain electrodes and coupled to a gate electrode (figure 1.27), they were able to achieve the control and measurements of single qubits.

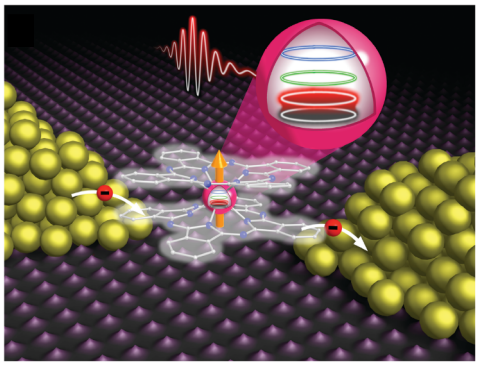

Figure 1.27: Artistic view of a nuclear spin qubit transistor based on a $TbPc_2$ molecule. The source and drain electrodes are represented in yellow. The molecule is composed of a Tb^{3+} ion (pink) connected to two Pc ligands (white). The nuclear spin states of the ion can be manipulated using electric field (generated by the gate).Ref. [Thiele et al., 2014].

The system is made up of three subsystems which are coupled using different interactions:

- The nuclear spin qubit related to the Tb^{3+} ion of the molecule. Its value is $I = 3/2$. Four spin (qubit) states are thus available: $|-3/2\rangle, |-1/2\rangle, |+1/2\rangle,$ and $|+3/2\rangle$
- The electronic spin of the 4f electrons of the Tb atom. The spin ground state has two eigenstates: $|\uparrow\rangle$ and $|\downarrow\rangle$. The hyperfine coupling with the nuclear spin lifts the degeneracy of this state, and each electronic state can be split into four states. Figure A.21.a shows those electronics/nuclear states for more clarity.

- A read out quantum dot, created by the Pc ligands in the vicinity of the Tb atom. The wavefunction of electrons of the π-orbital overlaps with the terbium 4f electrons. It induces an exchange coupling of ≈ 1.66 T.

Reading quantum bits The interactions occurring inside the whole system are used to manipulate the nuclear spin qubit. The read-out procedure is the following:

1. Each electronic ground state doublet is split into four nuclear spin-dependent levels, due to the hyperfine interaction (which is controlled by the gate voltage V_g). Electronic levels corresponding to the same nuclear spin are also split thanks to the Hamiltonian of the PC-ligant. In summary, the eight electronic-nuclear levels are differentiated.

2. Due to the exchange coupling between the quantum dot and the electrons, the conductance of this dot is tuned as a function of the electronic spin state. A sharp jump in conductance of observed when a magnetic field is raised. The position of these jump enables the identification of the electronic/nuclear state. Those jumps are illustrated in figure A.21.

Manipulation of the qubits Quantum computing is done by manipulating quantum bits instead of classical bits to perform operations. In the case of spin state used as qubits, one must be able to flip individual spins[Kane, 1998]. Now that the read-out of the qubits have been achieved, we focus on how to control those nuclear spin states. It relies on the hyperfine Stark effect which describe the change of the constant A in the hyperfine Hamiltonian: $H_{\mathrm{HF}} = A\mathbf{I}\cdot\mathbf{J}$. This Hamiltonian can be also written as a function of a virtual *effective* magnetic field acting on the spins at the center of the atom: $H_{\mathrm{HF}} = g_{\mathrm{N}}\mu_{\mathrm{N}}\mathbf{I}\cdot\mathbf{B}_{\mathrm{eff}}(A,J)$. The A constant can be tuned ($\approx 1\%$) by moderate electric field change amplitudes of 1 mV/nm. Experiments performed in the two-states subspace ($|+3/2\rangle$,$|+1/2\rangle$) of nuclear spins have demonstrated the effective modulation of A when applying a microwave pulse with an electrostatic gate. Further manipulations yielded to Rabi oscillations [37], showing the ability to effectively tune single qubits.

Decoherence Decoherence is the main source of error in quantum computing. External contributions lift the degeneracy of the qubits and therefore the operations are flawed. In this article, the coherence time is $\approx 64\mu s$. It was suggested that the decoherence was mainly caused by charge noise, which in turn induces effective magnetic fluctuations. Also, while applying an electric field pulse to tune the A constant, the effective magnetic field have components along the quantization axis of the molecule (which is the component that can rotate the spin) and along perpendicular directions, which induce additional decoherence. This quantization axis, unfortunately, cannot be known in advance.

[37] Oscillation of a quantum population between two levels in a two-level system.

Chapter 2

Microwave impedance microscopy

2.1 Working principle

Microwave impedance microscopy is a spectrometry technique that characterizes local electrical properties of a sample (permittivity and conductivity), using a scanning probe. An electronic microwave (0.1-10 GHz) signal is sent to a probe (a metal tip, usually made of Tungsten). It generates an electric field at its end which interacts with the sample. Variations in tip-sample complex admittance (Y) are measured, using the reflected signal by the sample. Real (also called, MIM-Re or MIM-R, resistive) and imaginary (MIM-IM or MIM-C, capacitive) parts of this signal are collected and linked to the changes in Y. This methods allows one to successfully spot changes of local electronics properties. It is widely used in the semiconductor and condensed matter physics. MIM is used as a scanning probe method and scanning images like shown in figure 2.1 are obtained. The contrast in the images represents the variation of local properties.

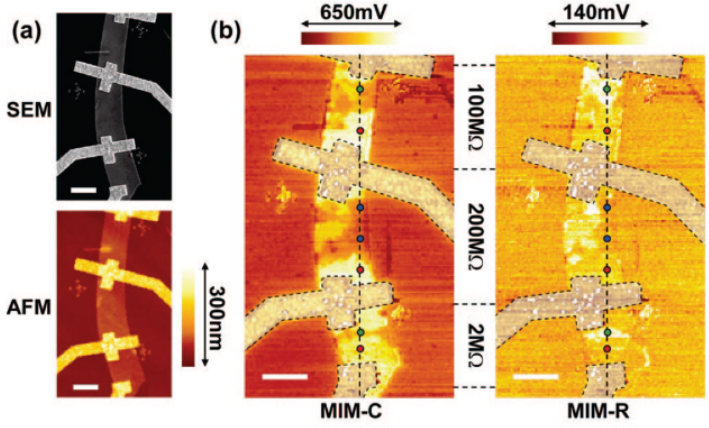

Figure 2.1: Experimental images of a large In_2Se_3 nanoribbon obtained with SEM, AFM and MIM. Ref. [Lai et al., 2008].

This method only requires one measurement terminal and no counter electrodes. It works at low voltage (below 0.1 V [Lai et al., 2009])) values, and below the frequencies of optical excitations. Therefore, MIM is a non-invasive method, in comparison with other scanning probe methods. It has a high sensitivity because changes of the order of the aF in tip-sample capacitance can be recorded [Cui et al., 2016].

2.2 Calibration

To extract an information about the local properties of the samples, the MIM signals obtained must be compared to reference values. To set a reference, simulations and calibration with homogeneous samples are used.
Using simulations (finite-element techniques are usually employed [Jones et al., 2017]), Y values for two given materials (with specific ε and σ values) are computed. Then, the values of MIM signals are measured with calibration samples patterned with these materials. A calibration sample (figure 2.2) is usually made up of an insulating substrate periodically patterned with another (conductive) material. Therefore, only two MIM responses (corresponding to the tip interacting with each material) are measured. These two MIM responses can therefore be assigned to theoretical Y values.

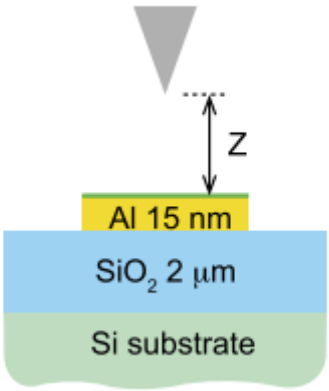

Figure 2.2: Example of calibration sample employed for the MIM experiment.Ref. [Cui et al., 2016].

Since MIM-Re and MIM-Im are directly proportional to $\Im(\Delta)$ and $\Re(\Delta)$, a linear fit using the two measured and simulated values can be made:

$$m = \frac{Y_2 - Y_1}{V_2 - V_1},$$

where Y_2 and V_2 are the simulated admittance and instrument output voltage for one region (material) of the sample, and Y_1, V_1 for the other region.
With this fit, it is possible to predict a Y (real or imaginary part) value for a given MIM-signal output (figure 2.3). Using simulations results (figure A.23) that links Y values to conductivity and permittivity, it is possible to predict the local properties (σ and ϵ). This method of linear fitting was successfully used in Ref. [Jones et al., 2017]. They were able to successfully predict the permittivity of polytetrafluoroethylene specimens.

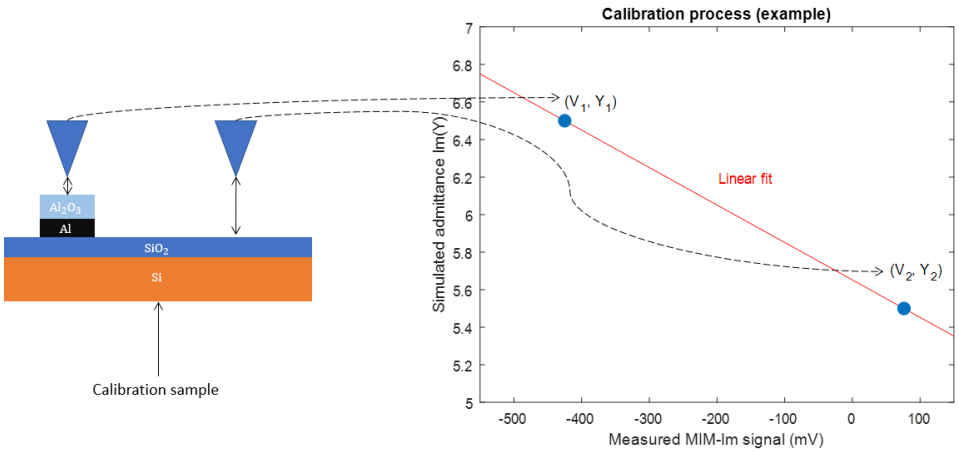

Figure 2.3: Schematic description of the MIM calibration process. Measured values of the MIM signals for each material are assigned to the corresponding simulated admittance values.

2.3 Example

MIM is usually employed to reveal inhomogeneity and/or defects in microscale samples. It has been used to reveal inhomogeneity in In_2Se_3 nanoribbons (with a length scale of around 100 nm). Recent advances in solid state physics have predicted that submicrometer variations of materials properties can occur at given conditions. Since MIM is sensitive to local changes in electronics properties, it was succesfully used to reveal electronic inhomogeneities, even under the surface of these nanoribbons (figure 2.1).

2.4 Hardware

A typical MIM setup is made up of three parts: the tip, the impedance match (signal routing and adapting the probe to the source) and the microwave electronics (generation and measurement of signals). In most of the cases, a third component is included, adding a low-frequency oscillating feature to the tip (in order to enable topography sensing). In the literature, some tips were used with a cantilever [Lai et al., 2009, Yang et al., 2014] or were glued to an oscillating quartz tuning fork (QTF) [Cui et al., 2016]. In our case, we were going to use a quartz tuning fork, due to its easy use and setup (figure 2.4).

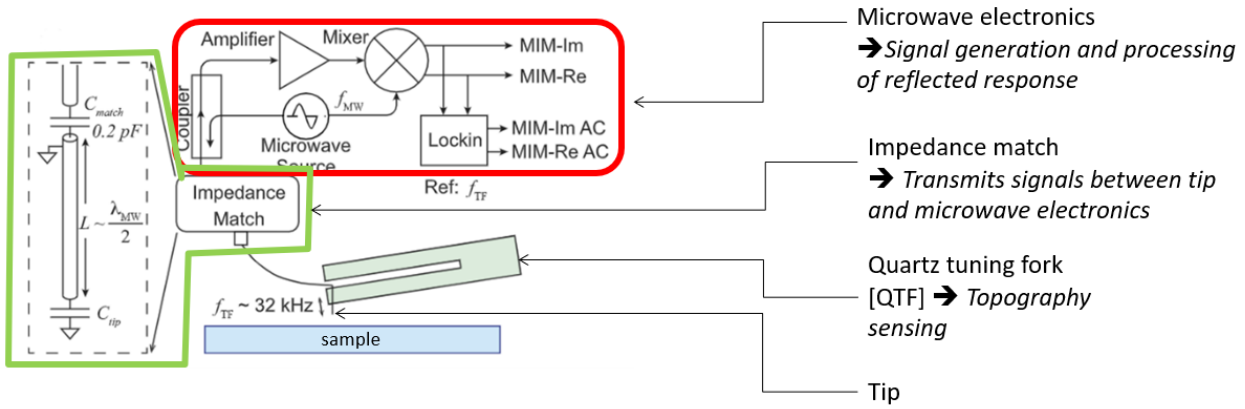

Figure 2.4: Schematic view of a MIM setup [Cui et al., 2016].

2.4.1 Microwave electronics

Microwave electronics generates the signal and process the electrical response from the sample. It contains the source that generates the signal with a given working frequency f_{MW} and send it to the probe through the impedance match. The microwave source also acts as a phase reference for the mixer. The mixer extracts the real and imaginary parts of the reflected signal. In practice, it gives as two output signals with a phase difference of 90 degrees (figure 2.5).

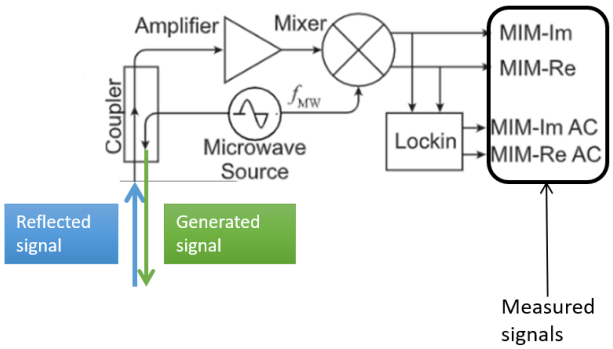

Figure 2.5: Microwave circuitry for MIM.

The coupler separates the reflected signal from the generated one. Since we work with AC currents, we assume the generated signal to have this form:

$$A_{source}(t) = A_0 e^{i\omega t + i\phi} = A_0(e^{i\omega t} + e^{i\phi}),$$

with ω the working angular velocity and ϕ the initial phase. We set the initial phase to 0, since it is the reference taken by the mixer. The reflected signal reads as:

$$A_{reflected}(t) = A_1 e^{i\omega t + i\phi_2} = \frac{A_{source}(t)}{B} e^{i\phi_2},$$

where $B = A_1/A_0$.
The mixer isolates B and ϕ_2, which are the module and the phase of the MIM signals.
In our case, a vector network analyzer (VNA) replaces the microwave electronics. The VNA is used to compute the S-parameters of microwave circuits and more specifically, the reflection coefficient S_{11}. Getting this (complex) parameter is equivalent of accessing the values of MIM signals, since after calibration, one can extract information about the local electric properties (ε_r, σ).

2.4.2 Impedance match

Impedance Z match transmits the signal from the probe to the electronics and minimizes the losses. The probes is usually modeled as a circuit made of a resistor (2 Ω), an inductor (2 nH) and a capacitor (2 pF) placed in series. Without the Z match, the probe would not be adapted to the microwave electronics impedance Z_0, resulting in undesired reflections (the power would be reflected back to source) and noise. The tip must be adapted to Z_0. This is done with the impedance match section of the setup.
It consists of a coaxial cable and a small capacitor connected in series (0.2 pF). The impedance-match acts as a resonator, whose resonant frequency is mainly determined by the length of the coaxial cable (in our case we choose to use a 10 cm cable to have a resonant frequency of 1 GHz). The capacitor is connected to a SubMiniature version A connector to the VNA. To avoid losses, the resonant frequency (at which reflections in the match are minimized) has to be found. Figure A.4 a) shows the resonant frequencies for a MIM setup.
However, only ceramic capacitors can achieve small capacitance values, and they have really small dimensions (below the millimeter). Directly connecting it to the SMA connector and the coaxial cable (by soldering it) would have been difficult. To overcome this challenge, different solutions exist; one would be to use a tuning stub instead of the capacitor. This solution is used by several teams [Lai et al., 2008]. The other one would be to use a printed circuit board (PCB) to solder the capacitor onto.
However PCBs are not suitable for radio-frequency (RF) applications. At high frequencies, the skin effect that increases the resistance is enhanced, especially in PCBs. Indeed, PCBs have proper inductance and capacitance values. Therefore, they must be carefully designed to not provoke losses in the Z-match.
The commercial software ADS (Advanced Design Setup) by Keysight allows one to perform RF simulations of electronics circuits and, in fact, S_{11} parameter can be estimated as a function of frequency. Furthermore, PCBs can also be designed with this software. We were pursuing on this direction before the COVID-19 crisis outbreak.

2.4.3 Quartz tuning fork and the AC mode

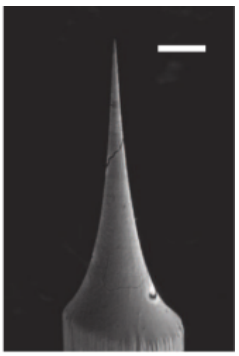

Figure 2.6: SEM image of a MIM tip [Cui et al., 2016]. The scale bar is 10 microns.

One interesting feature of MIM [Cui et al., 2016] is the QTF. This fork (on which the tip is glued) allows topography sensing. The QTF have a resonance frequency of around 32 kHz. When the tip approaches the sample or moves away from it, this resonance frequency slightly shifts and the topography will be recorded if the fork has a good quality factor. This shift of resonance is tracked with a phase-locked loop. This oscillation will also modulate the microwave signal at the same frequency. A lock-in amplifier is used in the microwave circuit to demodulate the signal. The AC mode was successfully demonstrated [Cui et al., 2016] and measures

$$\frac{\partial(MIM\ signal)}{\partial z},$$

with z being the tip-sample distance. This process eliminates the slow drifting of the background due to thermal and electrical fluctuations in the tip. It also increases the spatial resolution.

Chapter 3

MIM numerical computations

Atomic and molecular transistors are based on nanogaps and molecular/atomic "bridges". Monitoring the conductance state of these gaps requires the use of I-V curves, and therefore invasive, costly and time-consuming methods to add electrical contacts. It is a loss of time when the sample reveals to be of low quality during characterization. Using MIM to assess the quality of a sample before measurement could be a solution, since it is a non-invasive process.
Although its resolution is low compared to other scanning methods, it could be a tool to effectively determine if the contact between two electrodes exists or not. We investigate the performance of this process through tip-sample admittance thanks to COMSOL computations in the classical limit. Frequency domain analysis is used, with a working frequency of 1 GHz. We neglected the influence of microwave electronics, quartz-tuning fork and impedance match. The tip-sample interaction was simulated with the AC/DC module of the commercial software COMSOL. This simulation allows to understand the effects of different parameters on the performance of microwave impedance microscopy. First, we simulate the tip-sample interface for tips with different shapes and various samples. These simulations are inspired by Jones' work [Jones et al., 2015]. Then, a realistic nanogap was investigated.

3.1 Lumped-element model

The tip-sample system can be described as a simple electrical circuit. This has been done in several articles [Jones et al., 2015, Wei et al., 2016]. The tip is assumed to be a conductance G_1. The tip-sample interaction is described as a capacitor with a capacitance C_1. Finally, the sample of interest is made of a conductance G_2 and a capacitance of C_2 in parallel.

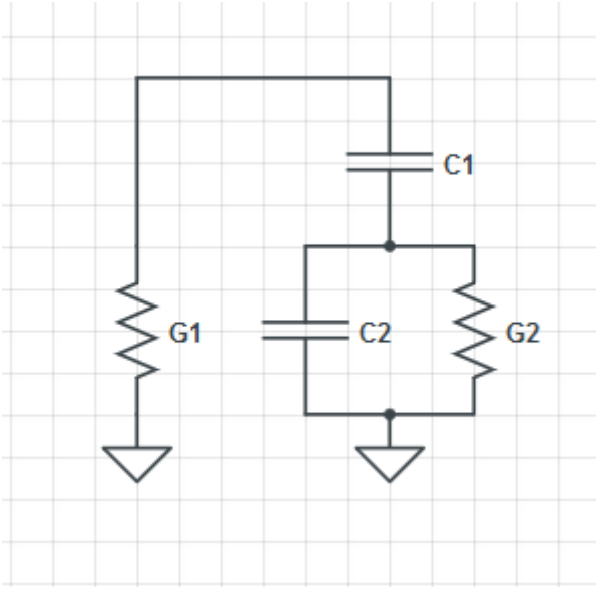

Figure 3.1: Lumped-element model of the tip-sample setup.

The lumped-element model is in accord with literature [Jones et al., 2017], the real and imaginary parts of admittance are as follows:

$$\Re(Y_{21}) = \frac{C_1^2 \cdot G_2 \cdot \omega^2}{G_2^2 + \omega^2 \left(C_1 + C_2\right)^2}, \tag{3.1}$$

$$\Im(Y_{21}) = \frac{C_1 \omega \left(C_2^2 \omega^2 + C_1 C_2 \omega^2 + G_2^2\right)}{G_2^2 + \omega^2 \left(C_1 + C_2\right)^2}. \tag{3.2}$$

3.1.1 Real part

Here $\Re(Y_{21})$ is a bell-shaped function of G_2. This corresponds to the standard experimental and simulation results [Lai et al., 2009, Jones et al., 2017]. However, the tip and the sample were simulated in some articles (such as Ref. [Jones et al., 2015]) in close contact and it results in $\Re(Y_{21})$ varying linearly with respect to G_2. In these conditions, C_1 is replaced by a simple resistance and the expression becomes linear.
However, the link between the electrical conductivity σ_{sample} and G_2 has not been correctly identified. In Ref. [Jones et al., 2015], it has been described as $G_2 = k\sigma_{sample}$, with k a parameter (in unit of meters) determined by the effective area of interaction between the tip and the sample.

3.1.2 Imaginary part

The expression $\Im(Y_{21})$ tends to be constant at high and low values of G_2. These two extreme values correspond respectively to the case of C_1 and C_2 acting as series capacitors and to the case of C_2 being short-circuited. This in accord with the experimental and simulated results present in the literature.

3.2 Homogeneous sample

3.2.1 Metallic sample

The first type of sample to be investigated is a homogeneous metallic system. We will work first in the contact mode.

Model description

Physics We first assume the tip-sample contact to be ohmic and we work in the classical description. The simulations are based on Ohm's law and Maxwell equations. Therefore, the only parameters considered are the electrical conductivity and permittivity. We use the AC/DC module of COMSOL, in the frequency domain, since we work with AC currents. In this domain, each physical quantity is represented as a phasor with a pulsation ω:

$$O(r,t) \rightarrow O(r)e^{-j\omega t}.$$

The equations solved by COMSOL are:

$$\vec{\nabla} \cdot \vec{J} = Q_{j,v}(r), \tag{3.3}$$

$$\vec{J} = \sigma\vec{E} + j\omega\vec{D} + \vec{J}_e, \tag{3.4}$$

$$\vec{E} = -\nabla V. \tag{3.5}$$

Eq. 3.3 is derived from the local charge conservation law:

$$\frac{\partial \rho}{\partial t} + \vec{\nabla} \cdot \vec{J} = Q_{ext},$$

where ρ is the charge density (C/m^3) and Q_{ext} (A/m^3) is the generation of charge per volume per unit of time. Using the Maxwell-Gauss local equation $\vec{\nabla} \cdot \vec{D} = \rho$, linking the the electric displacement field $\vec{D}$ to the charge density, the time derivation in the frequency domain $\frac{\partial}{\partial t} \rightarrow \cdot j\omega$ and the expression of the current density $\vec{J} = \sigma\vec{E} + \vec{J}_e$ this equation can be written as:

$$\vec{\nabla} \cdot (\sigma\vec{E} + j\omega\vec{D} + \vec{J}_e) = Q_{ext} = Q_{j,v}.$$

Eq. 3.3 is the charge density continuity equation, eq 3.4 is the Maxwell-Ampère equation and eq. 3.5 is the Poisson equation. The terms $Q_{j,v}(r)$ and $J_e(r)$ are, respectively, the generation of charge per volume per unit of time and the external current densities that can be set by the user (A/m^3 and A/m^2). Here, we do not set any of these sources, so these terms can be considered as being equal to zero.
The electric potential V is set in some points by the user to specify the distribution of the electric field $\vec{E}$. The current/tension/charge source are called *terminals* in COMSOL. We compute the admittance between two terminals: $Y_{21} = \frac{I_2}{V_1}$, where I_2 is the current flowing into the second terminal (bottom of the sample) and V_1 is the voltage applied to the first terminal (top of the tip).

Geometry and materials Since we work with a metallic sample, we only consider the conduction current ($\sigma\vec{E}$ of the equation 3.4) and $\sigma > 10^6 \frac{S}{m}$. The displacement current ($j\omega\vec{D} = \epsilon_0\epsilon_r j\omega\vec{E}$) is neglectible and we set the permittivity ε_r to 1 [1].
The geometric description of the model is showed in figure 3.2. We use a symmetric model with respect to an axis centered on the median plane of the tip. The tip is set with the tungsten properties $(\sigma, \varepsilon) = \left(1.79.10^7 \text{ S/m}, 6.2438\varepsilon_0\right)$ and put in direct contact with the sample (not shown in the scheme). The surrounding material is air $(\sigma, \varepsilon) = (0 \text{ S/m}, \varepsilon_0)$. Two terminals were set: on the top of the tip (terminal 1, blue line) and on the bottom surface of the sample (terminal 2, red line). The terminal 1 is set to 0.1 V, while the second one is set to 0 V. The blue terminal acts as the source of the microwave power. The boundary conditionsare the following: exception made for the terminals, all the model is set to 0 V.
We performed DC simulations to ensure the validity of the model. The resulting I-V curves are shown in figure 3.3. They indicates that Ohm's law is effectively followed.

Material	Electrical conductivity (MS/m)	ε_r
Gold	45.2	1
Copper	59.98	1
Aluminum	37.7	1
Platinum	9.66	1
Silver	63	1

Table 3.1: Parameters of the metals studied for the sample.

Results

Tip-admittance Tip-sample admittance was computed for the metals listed in table 3.1. The real part of the admittance increases with the conductivity, while the imaginary one decreases. This relation is easily explained by the lumped-element model.

[1] We performed DC simulations with different values of ε_r and no changes were noticed.

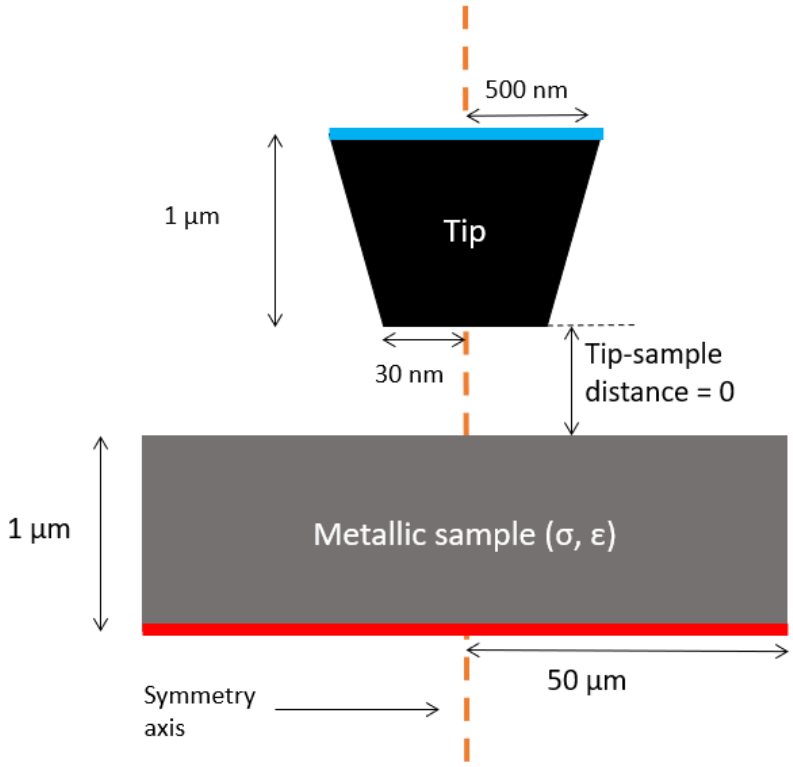

Figure 3.2: Schematic description of the model. The figure is two dimensional, but the effective model has an axial symmetry (the red dotted line). The blue line represents the terminal 1 (voltage: 0.1 V), which is playing the role of the microwave AC source in the AC model. The red line represents the terminal 2 (voltage 0 V). The tip-sample admittance is computed between those two terminals.

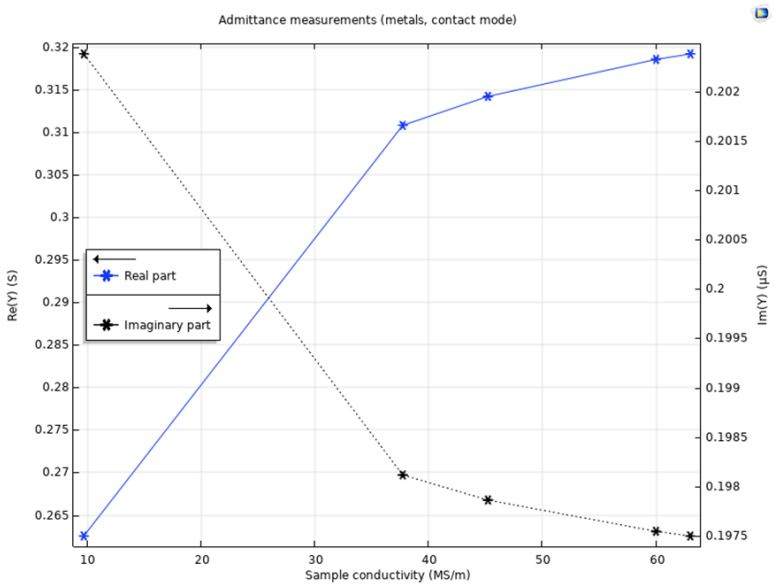

Figure 3.4: Tip-sample admittance as a function of the electrical conductivity for different metallic samples.

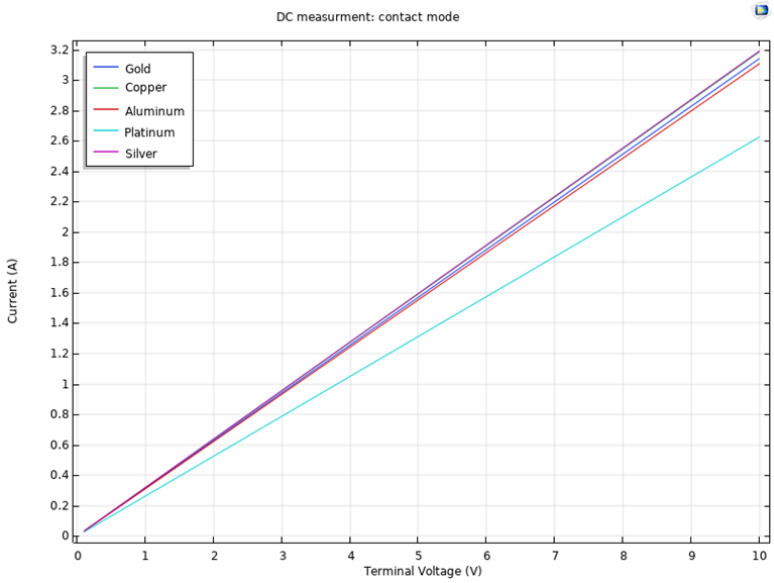

Figure 3.3: I-V curves simulated between the two terminals of the COMSOL model for different materials used as the sample. The linear relation confirms the validity of the model.

3.2.2 Semiconductor sample

We now consider the case of a semiconductor sample. Since we use a Tungsten tip, we can assume that a Schottky barrier will be present at the interface with the semiconductor. We use silicon properties for the sample. This barrier is observed for some semiconductor-metal contacts, especially for Si-W junctions. Therefore, we cannot only use Ohm's law and Maxwell equations here, given the microscopic properties of the semiconductor sample. We will use the semiconductor module of COMSOL.

Schottky barrier

A Schottky barrier is a potential energy barrier for electrons at metal/semiconductor [Kittel, 2007] junctions. The barrier depends on the difference between the electron work function Φ of the metal and the semiconductor electronic affinity χ_0. The electron work function corresponds to the work required to remove an electron from a solid to a point in the vacuum in the immediate proximity. Two electron current types pass through this barrier: the thermionic current (thermally excited electrons with an energy higher than the barrier), described by the Richardson formalism, and the tunneling current, neglected in the COMSOL classical simulation.
The equations solved by COMSOL for a Schottky barrier Φ_B are the following:

$$V = V_0 - \Phi_B$$
$$v_{s,n} = \frac{A_n^* T^2}{qN_c}, \quad v_{s,p} = \frac{A_p^* T^2}{qN_v} \quad ,$$
$$J_n \cdot \vec{n} = -qv_{s,n}\left(n - n_0\right), \quad n_0 = N_c \exp\left(-\frac{q\Phi_B}{k_B T}\right),$$
$$J_p \cdot \vec{n} = qv_{s,p}\left(p - p_0\right), \quad p_0 = N_v \exp\left(-\frac{q\left(E_g - \Phi_B\right)}{k_B T}\right),$$

V_0: Terminal potential set by the user,
$v_{s,n}$, $v_{s,p}$,: Recombination speeds,
J_n: Electron current density,
J_p: Hole current density.

The different quantities and their values are listed in the table below, taken into account the

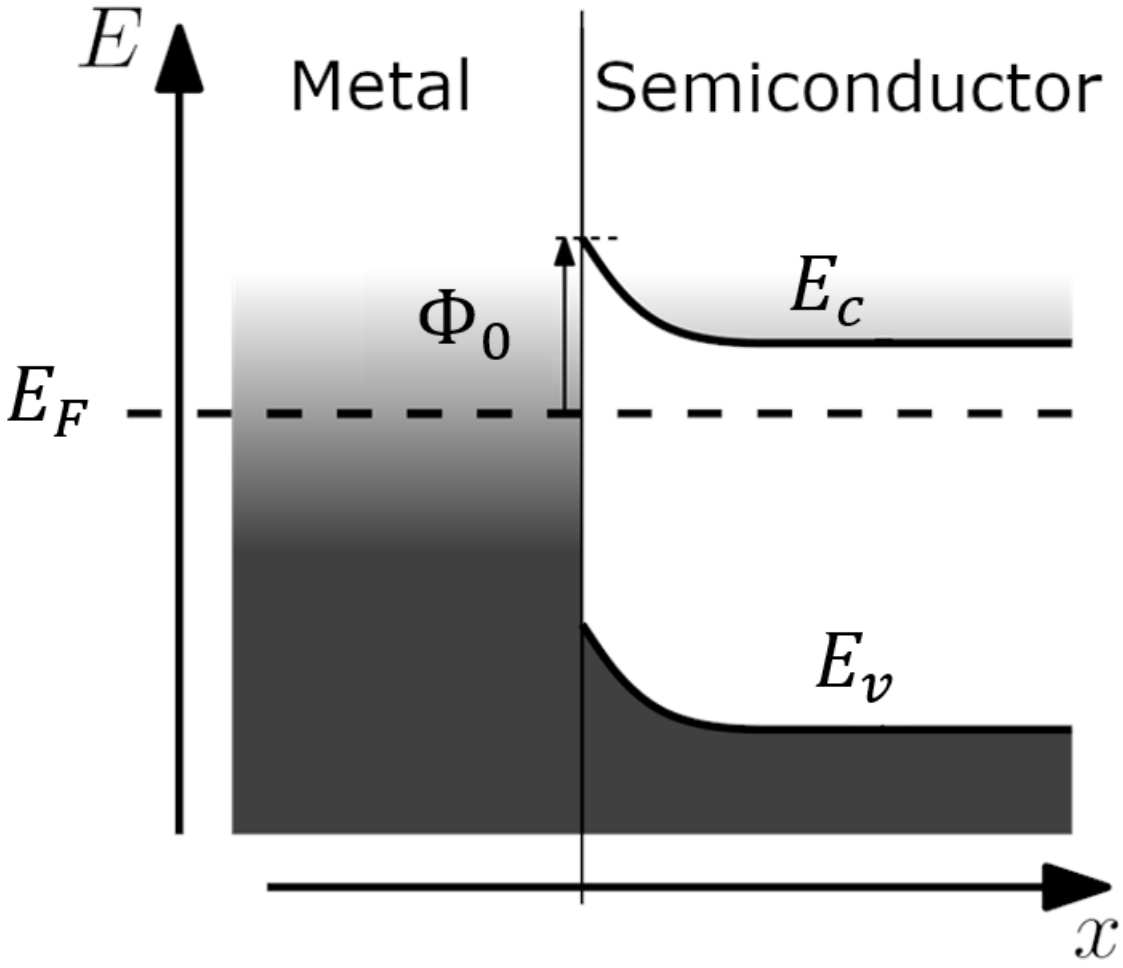

Figure 3.5: Energy configuration of a semiconductor-metal (Schottky) junction. Here E_F is the Fermi energy, E_v is the valence band and E_c is the conduction band.

common notations: q the electron charge, k_B the Boltzman constant, E_g is the effective bandgap (i.e. the sum of material bandage $E_{g,0}$ and of band narrowing ΔE_g) and T the temperature. These equations use the classical model of a semiconductor as the current flowing through the junction is calculated using only the thermionic emission mechanism.

Semiconductor equations

The equations used for the semiconductor are the following:

$$\begin{aligned}
&\rho = q\left(p - n + N_d^+ - N_a^-\right),\\
&q\tfrac{\partial n}{\partial t} = \vec{\nabla}\cdot\vec{J_n}, \quad q\tfrac{\partial p}{\partial t} = -\vec{\nabla}\cdot\vec{J_p},\\
&\vec{J_n} = n\mu_n\nabla E_c + \mu_n k_B T\nabla n + qnD_{n,th}\nabla\ln(T),\\
&\vec{J_p} = p\mu_p\nabla E_v - \mu_p k_B T\nabla p - qpD_{p,th}\nabla\ln(T),\\
&E_c = -\left(V + \chi_0\right) + \alpha\Delta E_g,\\
&E_v = -\left(V + \chi_0 + E_{g,0}\right) - (1-\alpha)\Delta E_g.
\end{aligned} \tag{3.6}$$

The equations are (from top to bottom): charge density ρ equation, continuity equations, electronic current, hole current, conduction band energy and valence band energy equations. The quantities used in the equation are listed in the table below.

n, p	Electron/hole density
J_n, J_p	Electron/hole current density
$E_{g,0}$	Material band gap
N_d^+, N_a^-	Ionized donor/acceptor concentration
μ_n, μ_p	Electron/hole mobilities
$D_{p,th}$, $D_{n,th}$	Hole/electron diffusion coefficient
V	Electric potential
χ_0	Electronic affinity

We work under multiple hypotheses:

- The Si sample is doped with donors (density: 10^{-16} cm^{-3})
- The dopants are completely ionized $N_d^+ = N_{dopant}$
- We work at room temperature
- The electric potential is uniform inside the tungsten tip

Model description

Figure 3.6 shows the 2D model of the semiconductor sample-tip system. The tip is not considered here: only its lower end in contact with the sample is considered. We assume that the electric potential is constant in the tip (which is confirmed by previous simulations). This model has also an axial symmetry. Admittance is also computed the terminals 1 and 2. The terminal 1, has a voltage of V_0 and acts as the source of the microwave power. At this boundary, the conditions of a Schottky contact are applied. The ground terminal (terminal 2) is set to 0 V. The other boundaries of the sample are considered to be insulated from the outside ($\vec{J}\cdot\vec{n} = 0$).

Φ_B	Barrier height = 0.67 V	$\overrightarrow{J_n} \cdot \vec{n}, \overrightarrow{J_p} \cdot \vec{n}$	Electron/hole current density flowing in the direction normal to the boundary
Φ	Metal (Tungsten) work function = 4.72 V	$v_{s,n}, v_{s,p}$	Electron/hole recombination speed
χ_0	Semiconductor (Silicon) electronic affinity = 4.05 V	N_c, N_v	Effective density of states at the conduction/valence band edge for silicon
A_n^*, A_p^*	Richardson coefficients =110, 90 [A/(Kcm^2)]	$(p_0, n_0)(p, n)$	Hole/Electron density at equilibrium (effective hole/electron density)

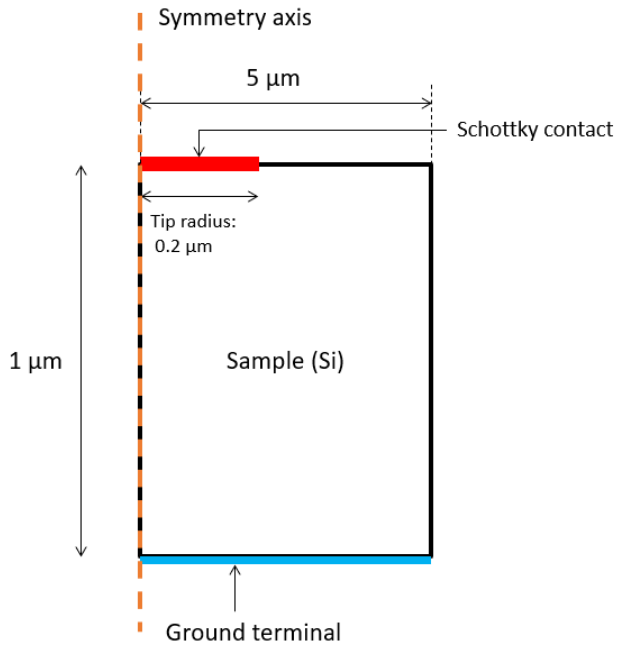

Figure 3.6: Schematic description of the Schottky model. The figure is in two dimensions but has axial symmetry (red dotted line). The red line represents the terminal 1 (terminal voltage V_0), which is the microwave source in the AC model. The blue line represents the terminal 2 (voltage: 0 V). The tip-sample admittance is computed between those two terminals. Here, the tip is not represented. Only its lower end in contact with the sample (terminal 1) is considered.

The Si sample properties are listed in the table below.

Silicon sample properties	
Relative permittivity ε_r	11.63
Material bandgap $E_{g,0}$	1.12 V
Electron affinity χ_0	4.05 V
Hole mobility μ_p	500 $(cm^2)/Vs$
Electron mobility μ_n	1450 $(cm^2)/Vs$
Conduction band fraction of bandgap narrowing α	1
Bandgap narrowing ΔE_g	0

DC model verification

To ensure the validity of the model, we have to first assess if the Schottky behaviour is observed in our sample. This is done using the exponential equation of the current across a Schottky junction:

$$I = I_S \left[\exp\left(\frac{V}{\eta V_{th}} \right) - 1 \right], \tag{3.7}$$

where V is the terminal voltage, $V_{th} = \frac{k_B T}{q}$, I_S is the saturation current and η is an ideality factor close to 1. We use curve fitting to assess the validity of our model. We find a value of I_S of 8.10^{12} A and a η factor of 0.8, which is consistent with the data reported in the literature. Figure 3.7 shows the simulated and the fitted theoretical I-V curves.

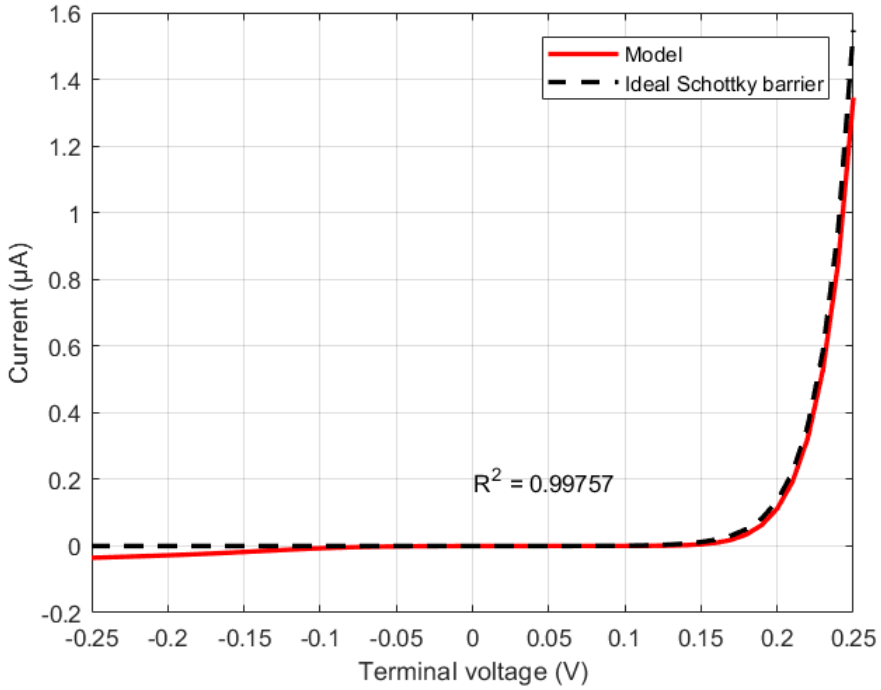

Figure 3.7: Verification of the semiconductor sample model using comparison with theory. Black dashed curve: fit of simulated values (red curve) to the theoretical formula for the current through a Schottky barrier.

Small-signal analysis and admittance measurements

MIM uses AC signals with a small amplitude, usually below 0.1 V. In this range, the current is quasi-constant according to the previous I-V curve. We therefore assume the microscopic configuration of the sample to be constant under a small bias. Therefore, we can use small-signal analysis to treat AC signals with this model. Small-signals analysis starts from a linearization point, which corresponds to the DC configuration. Then the response to a small AC deviation from the linearization point is computed by COMSOL. With small-signal analysis, one can compute Y_{21} (figure 3.8) as a function of the donor concentration.

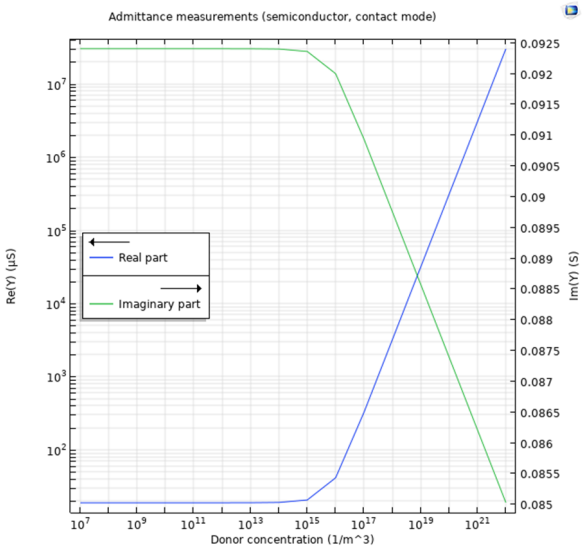

Figure 3.8: Tip-sample admittance (real part: green, imaginary part: blue) as a function of the donor concentration in the silicon sample.

3.2.3 Nanogaps with COMSOL

Now, let's consider the study of nanogaps with COMSOL. We try to investigate if MIM could detect a difference in the gap size (d_{gap}) in the nanometer range. The simulated 3D model is shown schematically in figure 3.9. Here, in the 3D model used, the voltage applied to the tip is 0.1 V, while the electrodes are grounded. Specifically, we considered two Al electrodes which are 1 micron thick. The tip, made of tungsten, has a spherical end with a 100 nm radius and sits at a distance d above the gap. In the numerical computations performed with COMSOL, we consider that the distance is fixed at 100 nm.
We computed Y_{21} at fixed frequency (1 GHz) for different values of d_{gap} from 0 to 100 nm. A linear dependency for the tip-sample admittance as a function of gap size can be seen in figure 3.10. The blue lines are linear fits to the data. The imaginary part of Y_{21} is much larger than the real part. Changing d_{gap} has a bigger influence on the tip-sample capacitance. However, although a global tendency is observed, the signal fluctuates too much to distinguish between two given gap sizes. We need to record Y_{21} with a tip located at other locations above the device and further numerical computations are required to investigate the performance of MIM with nanogaps.
We have simulated next a scanning image of the nanogap with the tip. The tip was moved above

the sample and Y_{21} was recorded at each position. The step used in the numerical procedure is 0.1 micron since it corresponds to the resolution computed previously. With this scanning mode, a difference between gap sizes can be spotted even for a value of 0.1 nm. This could be enough to distinguish between an open and a closed gap, for example. Several scanning maps were computed with different gap sizes, but the ones with the most contrast were the maps of the imaginary part of Y_{21}, as shown in figure 3.11. In this result, we notice that a resolution of 10^{-9} S is required for the experimental set-up. It roughly corresponds to a capacitance difference of 1 aF, which is distinguishable by typical MIM systems.
Although these simulations show that MIM could be a good method to be used with nanogaps, they were rather limited. The numerical computations were only done for a certain type of nanogap, with triangular metallic electrodes. Other electrode shapes and materials must be considered. In experimental conditions, the shape of the samples cannot be controlled perfectly and the results might differ from the theoretical or simulated ones.

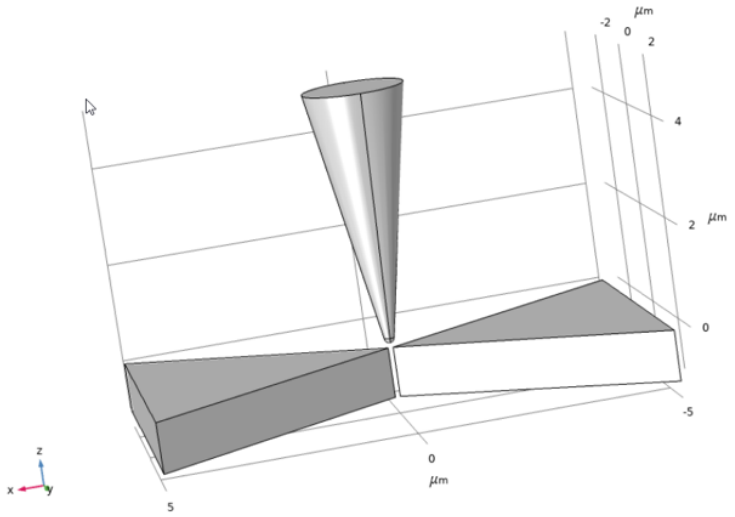

Figure 3.9: The 3D model of a MIM tip interacting with a nanogap, used for numerical computations with COMSOL, is shown schematically.

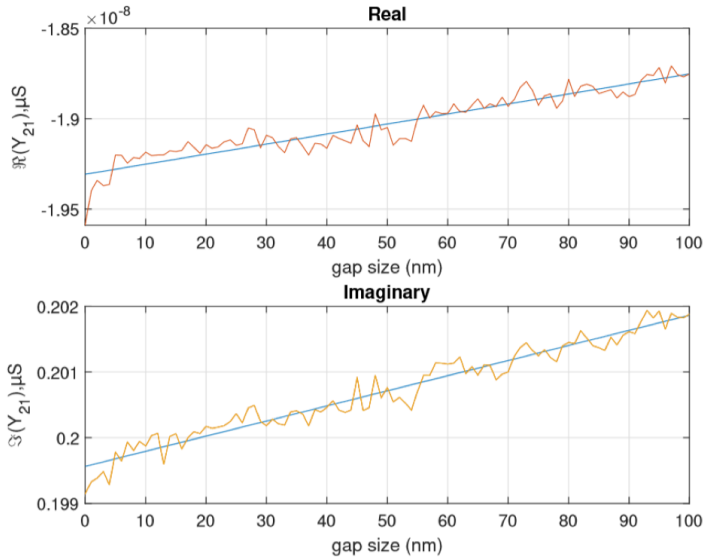

Figure 3.10: Computed Y_{21}, real (top panel) and imaginary (bottom panel) parts, at fixed frequency (1 GHz) for different values of d_{gap} from 0 to 100 nm.

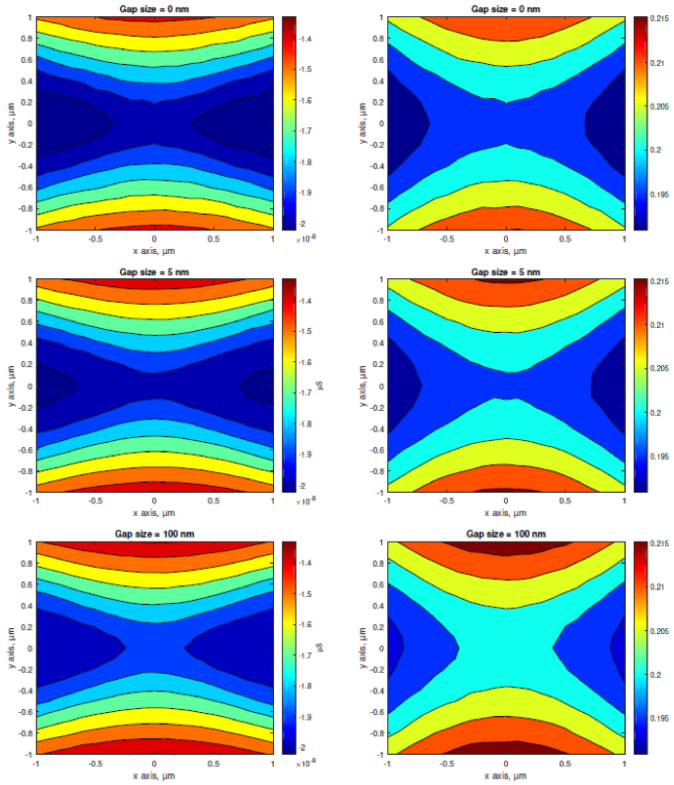

Figure 3.11: Several scanning maps were computed with different gap sizes, but the ones with the most contrast were the maps of the imaginary part of Y_{21} (right panels). The real part of Y_{21} is displayed in the left panels.

Chapter 4

Conclusion

During this work we have studied planar nanogap technology for atomic transistors from the perspective of MIM technique.
Our numerical computations indicate that opening or closing a nanogap induces a significant difference in tip-sample admittance. However, this analysis must be completed with experience, since MIM signal quality depends on the features of the experimental setup (noise management, impedance match, etc). Therefore, the effectiveness of the process will be proven essentially during the calibration step.
The model delineated in this work has also several limitations. The first one is that all the simulations were performed in the classical approximation: Maxwell equations were solved. In most of cases treated by the literature, classical simulations were sufficient since assumed homogeneous samples with dimensions around some μm that could be treated as continuous media. In our case, the gap was treated as a continuous medium with nanometer-scale dimensions (for the gap part). Quantum inhomogeneities and defects (simulations performed in literature show that 0D defects modify the response in the adjacent region [Jones et al., 2015]) could play a huge role in reality and could yield a totally different response, especially when we try to detect sub-nanometer scale transistor behavior. Therefore, attention has to paid to the sample purity. In addition to this aspect, we cannot take the quantum excitations into account in the classical model. Even if at the working wavelength (1 GHz) we are below the general electronic quantum excitations, resonant excitations could appear, especially at low temperatures. Indeed, microwave tunnelling through a nanogap has been observed [Lee et al., 2016], and this effect could modify the tip-sample admittance.
Another limitation comes from geometrical and topology considerations. The nanogap studied by numerical computations has a perfect trapezoidal shape with a large tip above. In the reality, nanogaps have different shapes since the shape of the electrodes depends on the fabrication process employed. Shape of the electrodes could be slightly different for a different width of the gap. Others simulations are required before using MIM with large-width nanogaps such as the ones produced by electromigration [Naitoh et al., 2013]. In conclusion, the simulations performed here were limited to a certain type of nanogap and might neglect some phenomena occurring at sub-nanometer scale.
In order to better understand the influence of MIM, one could perform quantum electronic transport simulations. The free python package software Kwant allows one to perform tight-binding simulations and extract several parameters such as electronic density or current density and 1D, 2D and 3D samples can be simulated. Interesting materials for this work can be

graphene or silicene, thanks to their exceptional properties and their sheet geometry. Moreover, electronic properties of graphene and silicene are sensitive to charge and potential variations. A closed nanogap can be easily simulated with Kwant. One can go further and then add the tip to the simulated setup, and consider the air separation as a potential barrier, with a value determined by the tip-sample distance. However, working with a model with different spatial scales requires a scaling method [Liu et al., 2015] and the results may not fit the really.
Another issue of these numerical computations is the time and computational power required. To simulate the nanogap system it took hours and around 5 GB of RAM. The analytical solution of the tip-sample interaction could help save time and computing power but it hasn't been found yet. However, a solution of the Poisson equation, whose solution yields the electric potential ϕ provided a charge spatial distribution $Q(\vec{r})$:

$$\nabla^2\phi = Q(\vec{r}),$$

has been found for a spherical tip in bi-spherical coordinates [Wei et al., 2015]. This coordinate system is described by the equations:

$$\begin{aligned} x &= \frac{a\sin\eta\cos\phi}{\cosh\mu - \cos\eta} \\ y &= \frac{a\sin\eta\sin\phi}{\cosh\mu - \cos\eta} \\ z &= \frac{a\sinh\mu}{\cosh\mu - \cos\eta}, \end{aligned}$$

$$\text{where } 0 \leq \phi \leq 2\pi, -\infty \leq \mu \leq \infty, \text{ and } 0 \leq \eta \leq \pi.$$

Here a is the distance between the foci and the origin. This bi-spherical coordinate system results from rotating a two-dimensional bipolar coordinate system about the axis that connects the two foci. The ground plane is located on $\mu = 0$ and the boundary of the tip is in $\mu = \mu_0$. If we consider a punctual charge in (μ_c, η_c, ϕ_c), the Poisson equation reduces to:

$$\nabla^2\varphi = -\frac{1}{h_\mu h_\eta h_\phi \varepsilon_0}\delta(\mu - \mu_c)\,\delta(\eta - \eta_c)\,\delta(\phi - \phi_c).$$

The scale factors h_μ, h_η, h_ϕ, in the bi-spherical coordinates are:

$$h_\eta = h_\mu = \frac{a}{\cosh\mu - \cos\eta},$$

$$h_\phi = \frac{a\sin\sigma}{\cosh\mu - \cos\eta}.$$

The boundary conditions are:

$$\varphi(\mu = 0) = 0 \text{ and } \varphi(\mu = \mu_0) = 0.$$

As indicated above $\mu = 0$ corresponds to the plane $z = 0$, which is the so-called ground plane and $\mu = \mu_0$ corresponds to a sphere of radius $\frac{a^2}{\sinh^2\mu_0}$, which is the surface of the spherical tip. The electrical potential is set to 0 on these two surfaces. The general solution (which is called *Green's function*) is:

$$G_q = \sum_{n=0}^{\infty}\sum_{m=0}^{n} -(0.5+m)\sqrt{(\cosh\mu-\cos\eta)}\cos\left[m\left(\phi-\phi_c\right)\right] P_n^m(\cos\eta)\cdot \begin{cases} \frac{2\sinh N(\mu_0-\mu)\sinh N\mu_c}{\sinh N\mu_0} & \text{if } \mu>\mu_c \\ \frac{2\sinh N(\mu_0-\mu_c)\sinh N\mu}{\sinh N\mu_0} & \text{if } \mu<\mu_c \end{cases}.$$

Here $N = 0.5 + n$, $P_n^m(\cos\eta)$ is the associated Legendre polynomial of degree n and order m, n and m are summing indices. The solution for an arbitrary dipole in the boundary of the tip can be found in Ref. [Wei et al., 2015]. Using this solution, one can calculate the charge density (and therefore, the potential and electric field) induced by an arbitrary dipole inside the tip. The tip here is assumed to be a cone ended by a sphere as shown in figure 4.1 b). However, it has been shown using simulations that the spherical end can be taken into account alone without differences (figure 4.1). Figure 4.1 c) shows the calculated charge density (and the simulated value) induced by a dipole along the tip. However, this model can be used considering only if the separation between the spherical end of the tip and the sample is small enough.
One can compute the tip-sample admittance using this function. Finite-element simulations are in accord with the analytical Green's function. Working with this analytical solution would help to save computational power and time required for finite-element simulations, and may open a way to perform quantum transport simulations with Kwant, since the potential induced by the tip (on graphene or silicene atoms) has an analytical expression.

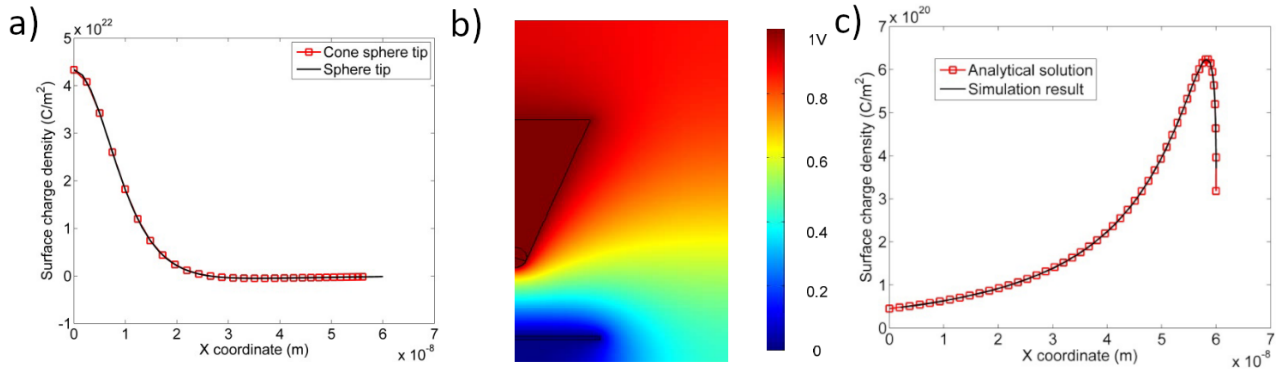

Figure 4.1: a) Comparison between the surface charge density induced by a MIM tip (cone ended by a sphere) with and without the conic part. It shows that the conic part has no significant influence. b) Typical potential distribution of tip-ground system for a cone-sphere tip. c) Surface charge density along the tip induced by a unit η direction dipole. Simulations performed with COMSOL are in accord with the analytical solution. Ref. [Wei et al., 2015]

Since we are also interested in single molecule transistors, it may be interesting to investigate the efficiency of MIM dealing with molecules deposited between two electrodes. Simulating this kind of structure with COMSOL isn't really accurate, since the closest thing to a molecule lying between two electrodes would be a long wire with ridiculously small dimensions. In this case, simulating an atomic chain (or ribbon) may give better results with smaller computational resources required.
Simulating an atomic chain with Kwant could provide interesting results. The band structure can be plotted for different potentials applied to the atomic chain. Thanks to the Green function calculated in Ref. [Wei et al., 2016], the exact potential induced by a tip can be applied to the atomic chain. Also, the effects of spin could be investigated. This may allow one to investigate the effectiveness of MIM as a function of spin configuration, and thus selecting molecules which

may give better results with MIM. If a way of computing the reflected signal by the molecule with Kwant is found, the tip-sample admittance can be calculated.
Another perspective to improve the numerical computational process would be to investigate the influence of MIM signal on the electronic transport through a nanogap. This can be achieved in the quantum regime with Kwant, using graphene or silicene. In the classical model, one can simply set a current flowing through the nanogap and look at the value of the tip-sample admittance. This approach could also help to investigate the effect of noise in a nanogap, since the signal created by MIM is usually weak.

Appendix A

Additional figures

Table 1 Challenges and opportunities for semiconductor R&D						
Year of production:	1999	2002	2005	2008	2011	2014
DRAM half-pitch (nm)	180	130	100	70	50	35
Overlay accuracy (nm)	65	45	35	25	20	15
Microprocessor gate length (nm)	140	85–90	65	45	30–32	20–22
Critical-dimension control (nm)	14	9	6	4	3	2
Equivalent oxide thickness (nm)	1.9–2.5	1.5–1.9	1.0–1.5	0.8–1.2	0.6–0.8	0.5–0.6
Junction depth (nm)	42–70	25–43	20–33	16–26	11–19	8–13
Metal cladding (nm)	17	13	10	0	0	0
Inter-metal dielectric κ	3.5–4.0	2.7–3.5	1.6–2.2	1.5	<1.5	<1.5

Table A.1: Semiconductor industry challenges. Yellow: solutions being pursued, red: no known solutions. Ref. [Peercy, 2000].

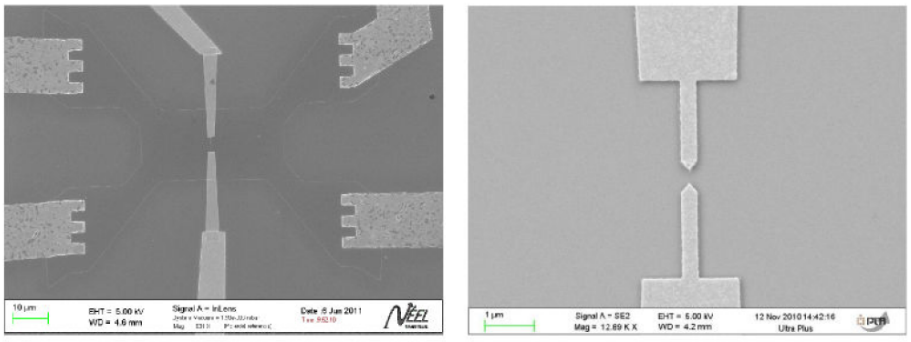

Figure A.1: Scanning electronic microscopy (SEM) images of a GaAs quantum point contact. Left figure: large field microscopy. The lighter parts correspond to metallic electrodes. In the center, the narrow electrodes act as gate electrodes (they define electronic paths electrostatically by controlling the electronic density below them). The four contacts in the corners are ohmic contacts used to contact the two-dimensional electron gas and perform transport measurements. The conductive part of the sample is a little darker. Right figure: narrow field microscopy of the gates. Ref. [Brun, 2014].

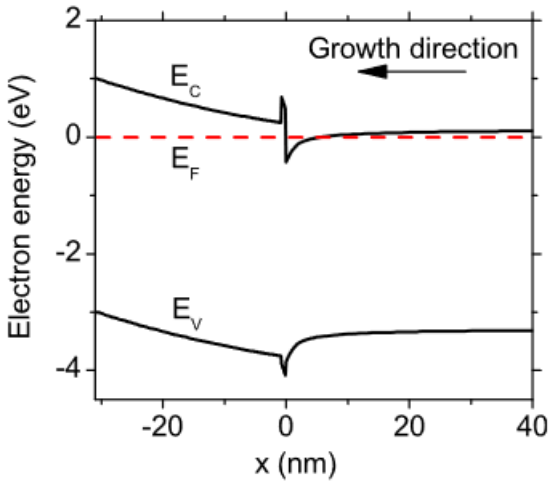

Figure A.2: Band structure of an AlGaN-based heterostructure. The red dotted line is the Fermi level. The boundary between AlGaN (negative x values) and GaN (positive x values) is in $x = 0$. At the interface, the band offset can be seen and is used to confine electrons in the x-direction. Ref. [Ahmadi et al., 2016].

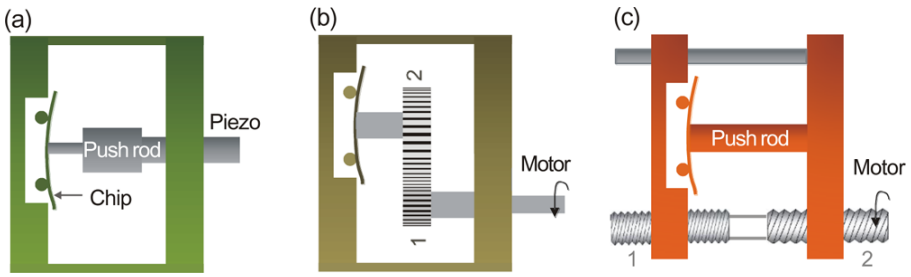

Figure A.3: Schematic views of the devices used to bend the substrate for the MBJ setup. a) Push rod driven by a piezo actuator. b) Push rod driven by a motor and gear coupling. c) Push rod driven by a motor and differential screws. Ref. [Brun, 2014].

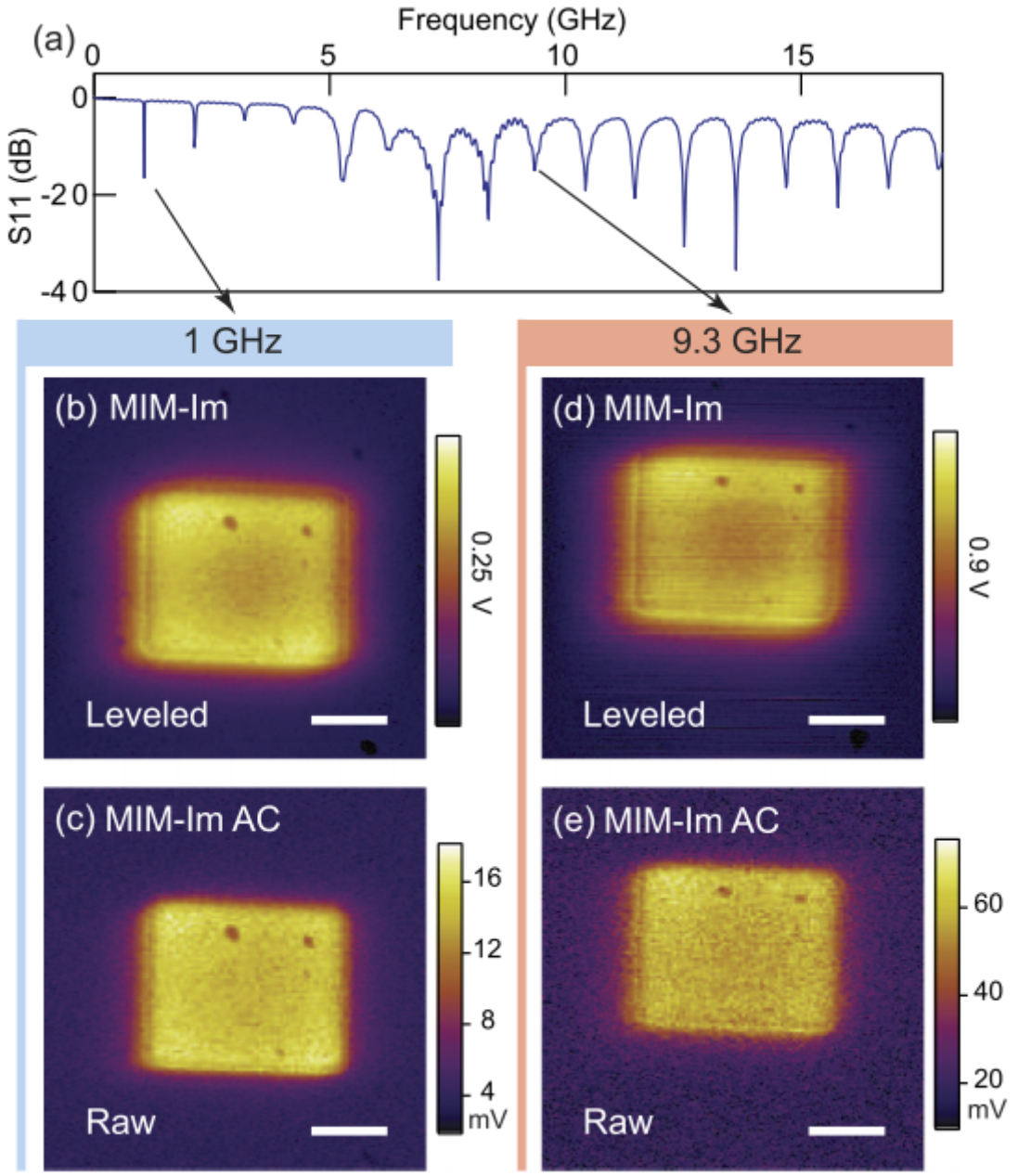

Figure A.4: a) Measured S_{11} parameter as a function of frequency. Tip-sample interaction is maximal at resonant frequencies. b - e) MIM images of the sample for indicated resonant frequencies. The sample observed is made up of SiO_2 patterned with Al dots. The lighter part of the image correspond to an Al dot. Ref. [Cui et al., 2016].

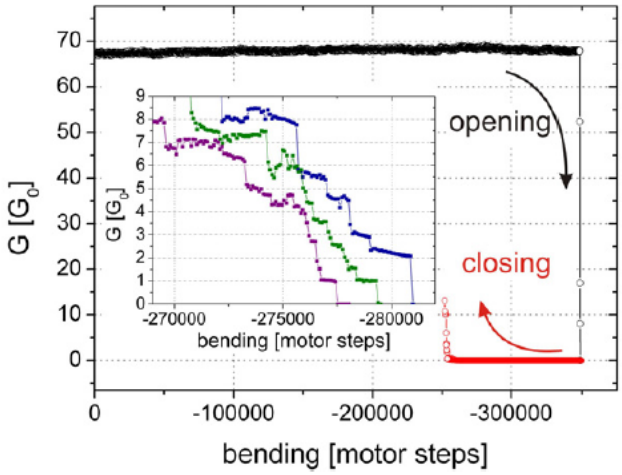

Figure A.5: Conductance vs bending in a molecular MBJ QPC. The conductance G shows abrupt changes in integer numbers of G_0. The 1500 motor steps correspond here to a variation of 1 Å. Ref. [Ballmann and Weber, 2012].

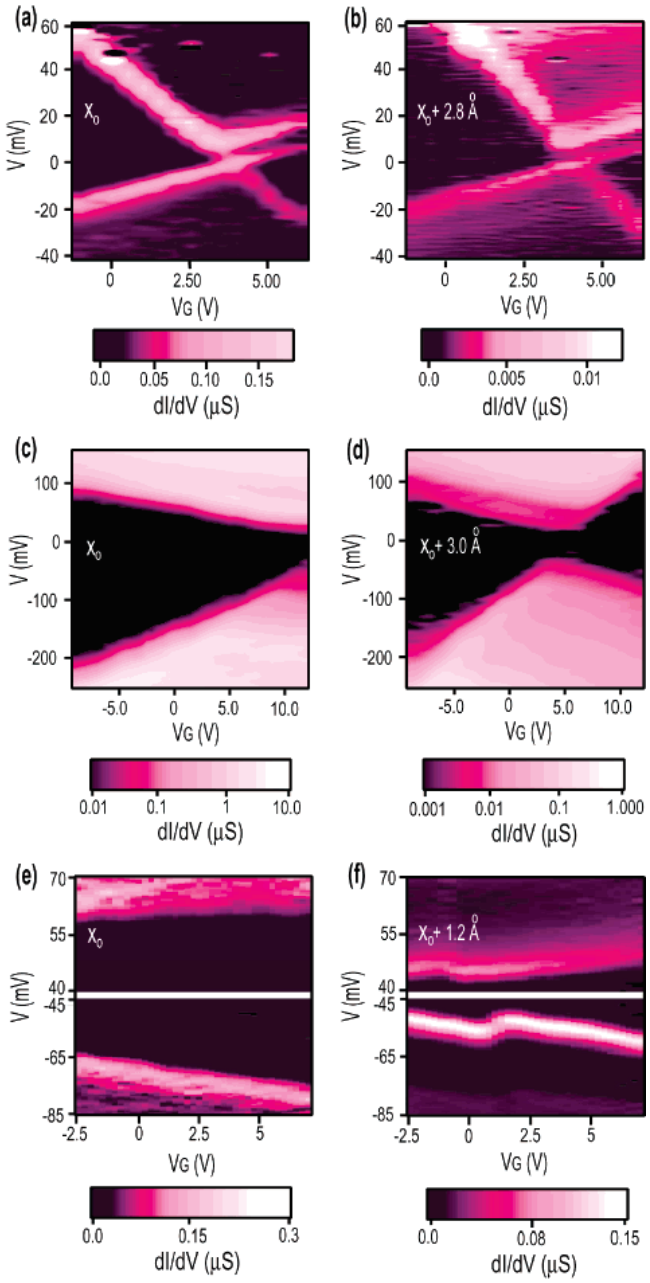

Figure A.6: Color plot of differential conductance as a function of V_g and V_{sd} (V), measured in MBJ single-molecule (C_{60}) transistors (one C_{60} is connecting the two electrodes). Here x_0 represents the initial source-drain displacement. a, b) Sample 1 (linear scale). c, d) Sample 2 (logarithmic scale). e, f) Sample 3 (linear scale). Ref. [Champagne et al., 2005].

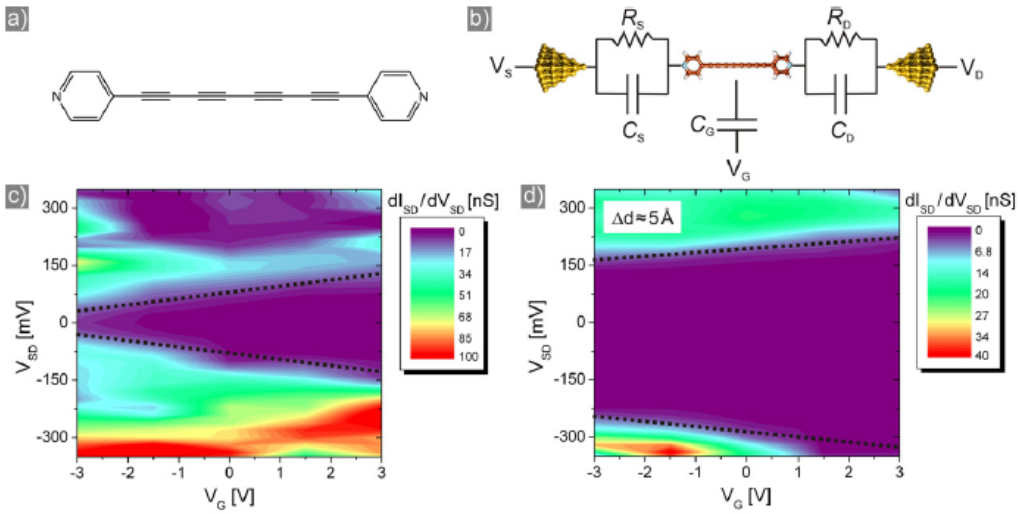

Figure A.7: a) A typical molecular wire used in MBJ transistors. b) Schematic representation of a single molecular transistor. c, d) Stability diagrams (differential conductance as a function of V_g and V_{sd}). Ref. [Ballmann and Weber, 2012].

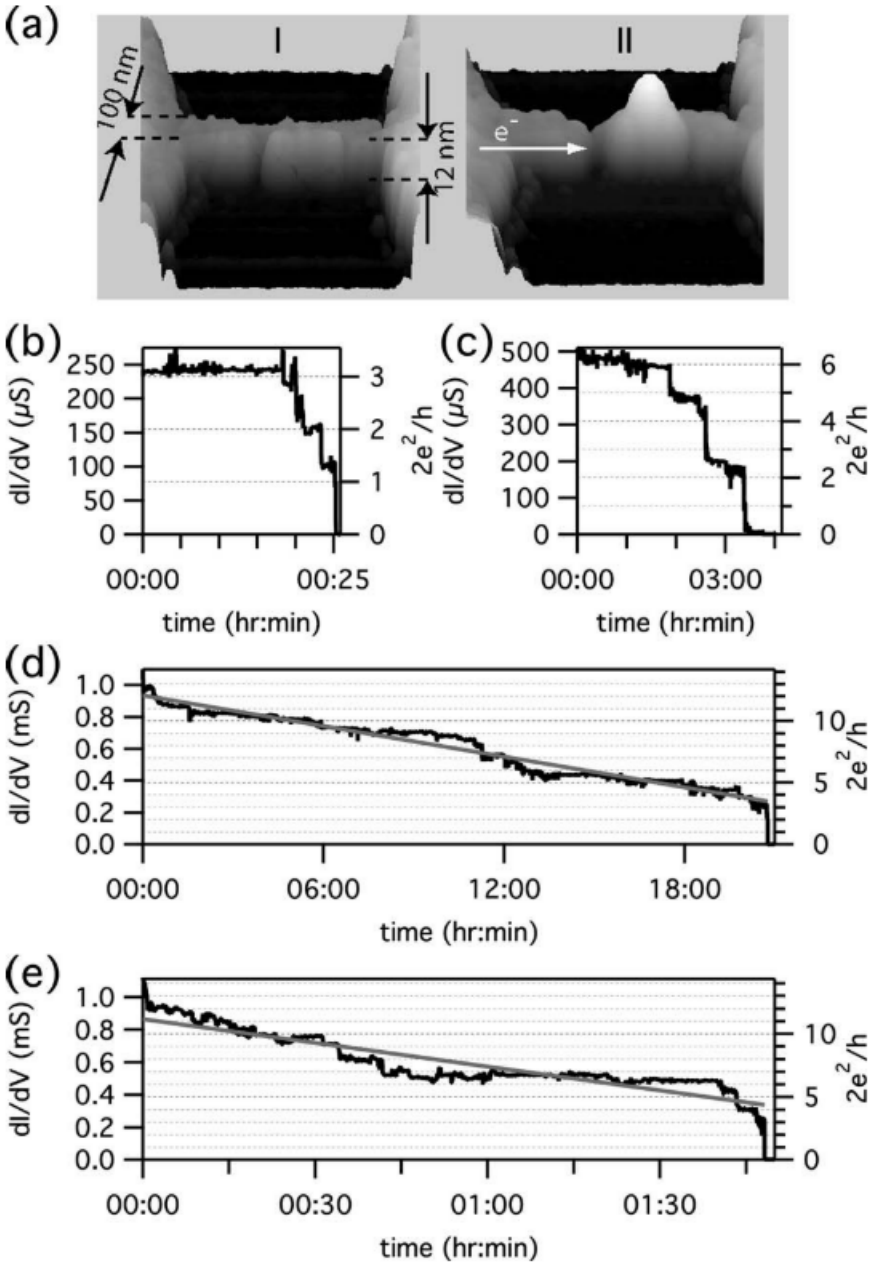

Figure A.8: a) AFM images of a sample before and after electromigration. b - e) Conductance as a function of time illustrating the self-breaking process (Au junctions at room temperature), with samples previously narrowed until different resistance values: 4 kΩ, 2 kΩ, 900 Ω and 700 Ω. Ref. [Heersche et al., 2007].

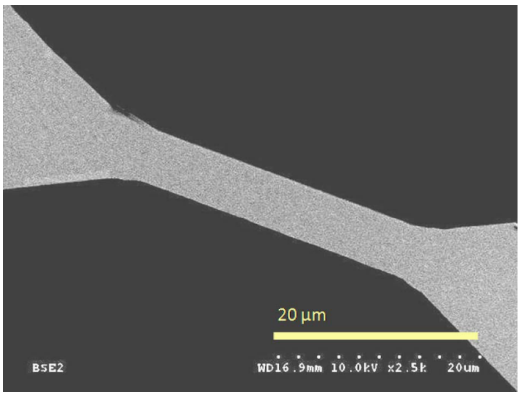

Figure A.9: SEM picture of a gold metal sheet defined by lithography. Ref. [Asghar et al., 2010].

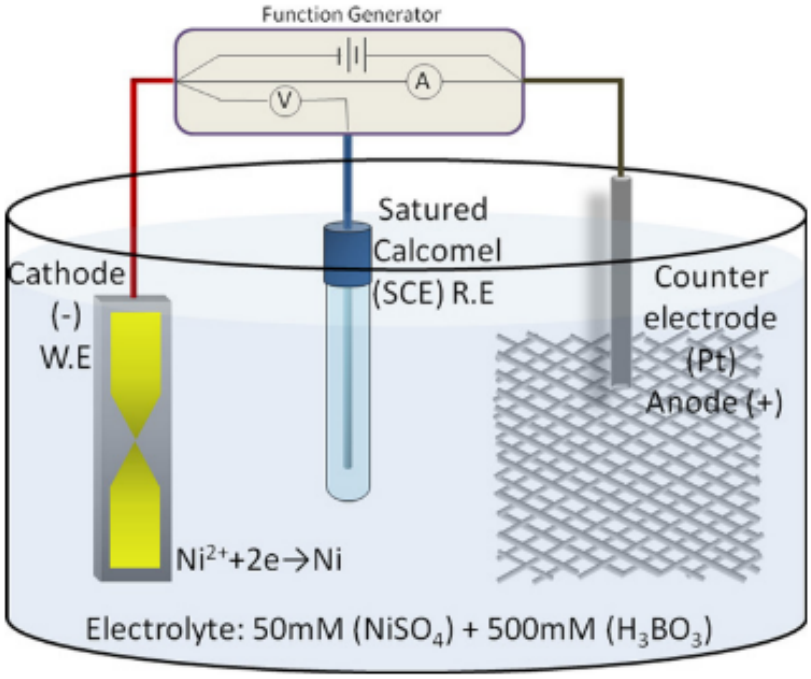

Figure A.10: Electrochemical cell used in the preparation of atomic transistors. Ref. [De Los Santos Valladares et al., 2010].

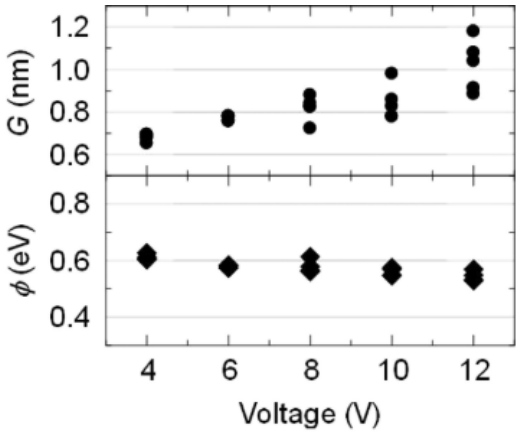

Figure A.11: Influence of the electromigration voltage on the nanogap parameters. The samples are made up of two gold electrodes separated by nanogaps. The nanogap is obtained with a process that combines gold deposition and electromigration. Each dot represents one sample. Top figure: width of the gap (G) of some samples as a function of voltage applied during the electromigration process. Bottom figure: barrier height ϕ as a function of voltage. This barrier correspond to the energy gap between the two electrodes. Electrons can pass through via tunnelling emission. This barrier height was estimated via the tunnelling equation. Ref. [Naitoh et al., 2013].

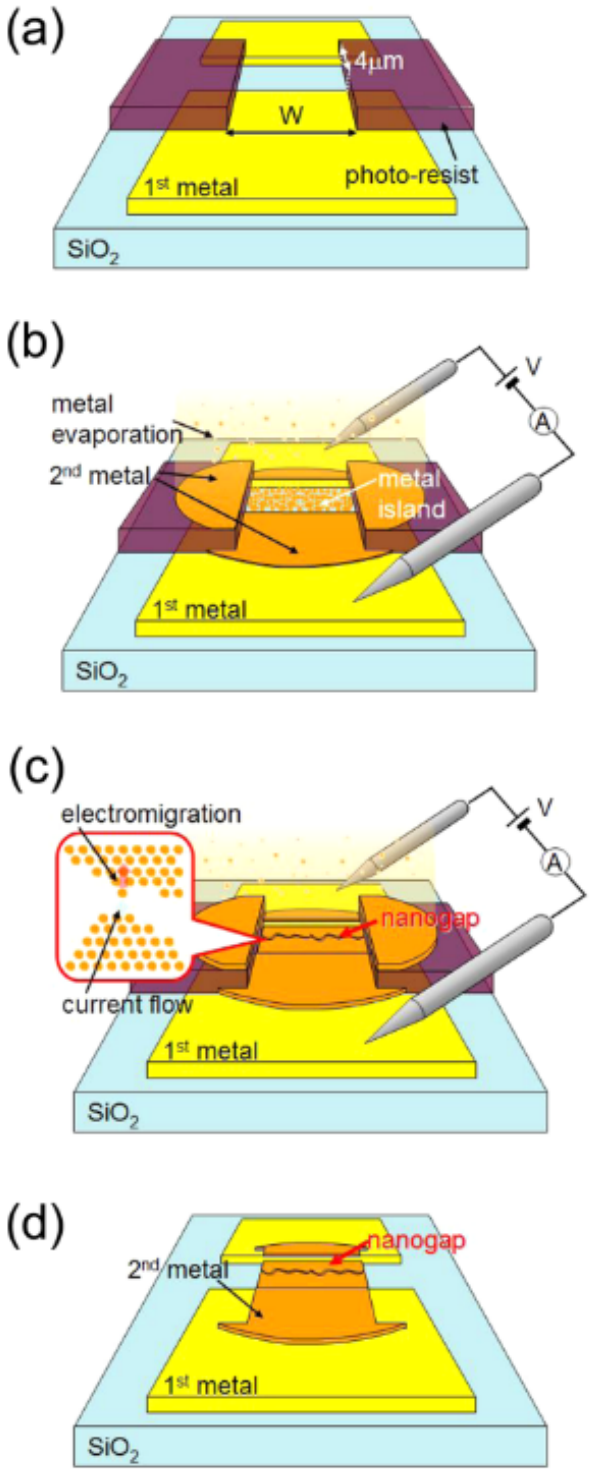

Figure A.12: Schematic view of the electromigration process used in Ref. [Naitoh et al., 2013]. a) Deposition of the photoresist. b-c) Metal evaporation and electromigration using a voltage. d) Sample after lift-off.

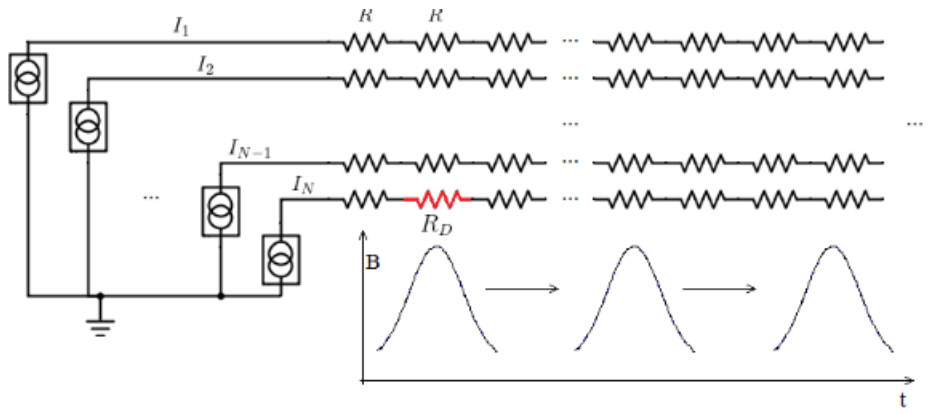

Figure A.13: Model employed to simulate the effect of a transverse magnetic field (TMF) on an arbitrary nanowire. This nanowire is modelled as N parallel sub-wires with different currents in order to simulate the Hall effect induced by the TMF. The graph in the lower part show how the magnetic field can be moved along the wire to electromigrate it from a given location at the edge. Ref. [Sheikholeslam et al., 2014]

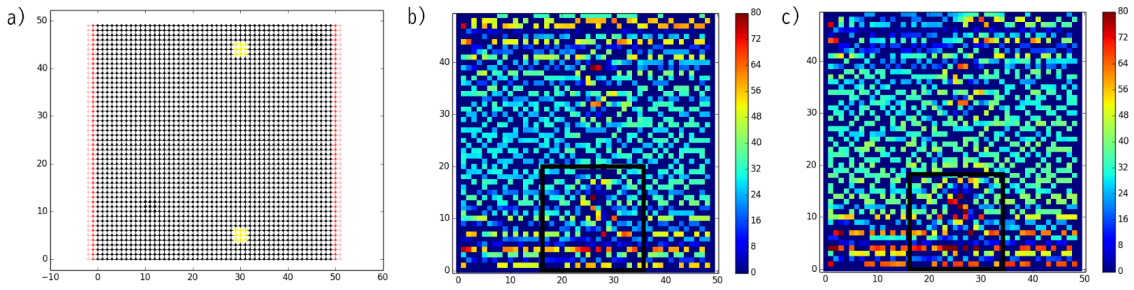

Figure A.14: Numerical simulation using Kwant of the "wind force" (arbitrary units) of electrons applied to the ions in a 50×50 atoms lattice set with arbitrary physical parameters. a) View of the lattice model. Each dot represents an atom. The red dots represent the leads (perfect reservoirs of electrons). The right and left leads have, respectively, chemical potentials of $\mu_R = 0$ and $\mu_L = 10^{-4}$, allowing electron conduction. The yellow dots represent defects in the lattice (dangling bonds). b) Map of the mechanical stress when no magnetic field applied. c) Map of the mechanical stress when a transverse magnetic field applied. The mechanical stress is stronger on one edge (the bottom edge). The Hamiltonian used for tight-binding is $H(t) = \sum_i e^{\frac{-ieA(t)\delta_i}{\hbar c}} t_{i,i+\delta_i} c_i^\dagger c_{i+\delta_i} + \sum_i \epsilon_0 c_i^\dagger c_i$, with $c_i, c_i^\dagger$ being the electronic creation and annihilation operators. The $A(t)$ is the potential vector corresponding to $\vec{A(t)} = -B(t)y\hat{x}$, t is the hopping integral and ϵ_0 is a bonding parameter (to define "dangling bonds", this coefficient is set to 0). Ref. [Sheikholeslam et al., 2014].

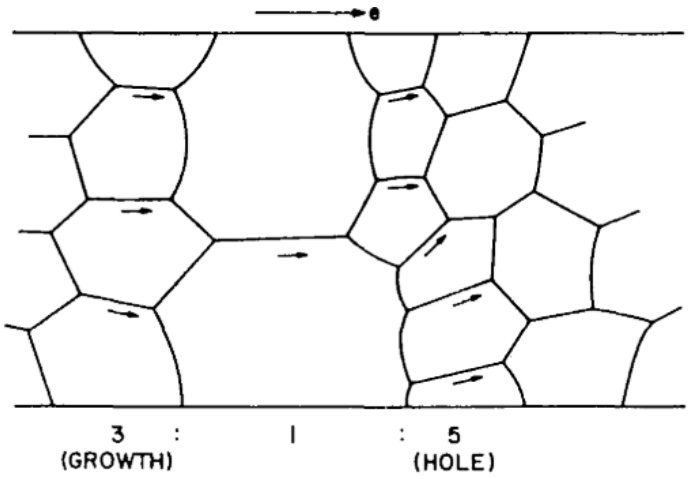

Figure A.15: Schematic explanation of the effect of electromigration in a non-uniform grain structure. The arrows represent the magnitude of mass migration. Significant mass build-up occurs at the boundary from small to large grains, whereas a corresponding mass depletion proceeds at the boundary from large to small grains. Electromigration is therefore enhanced when the number of boundaries increases. Ref. [Scorzoni et al., 1991].

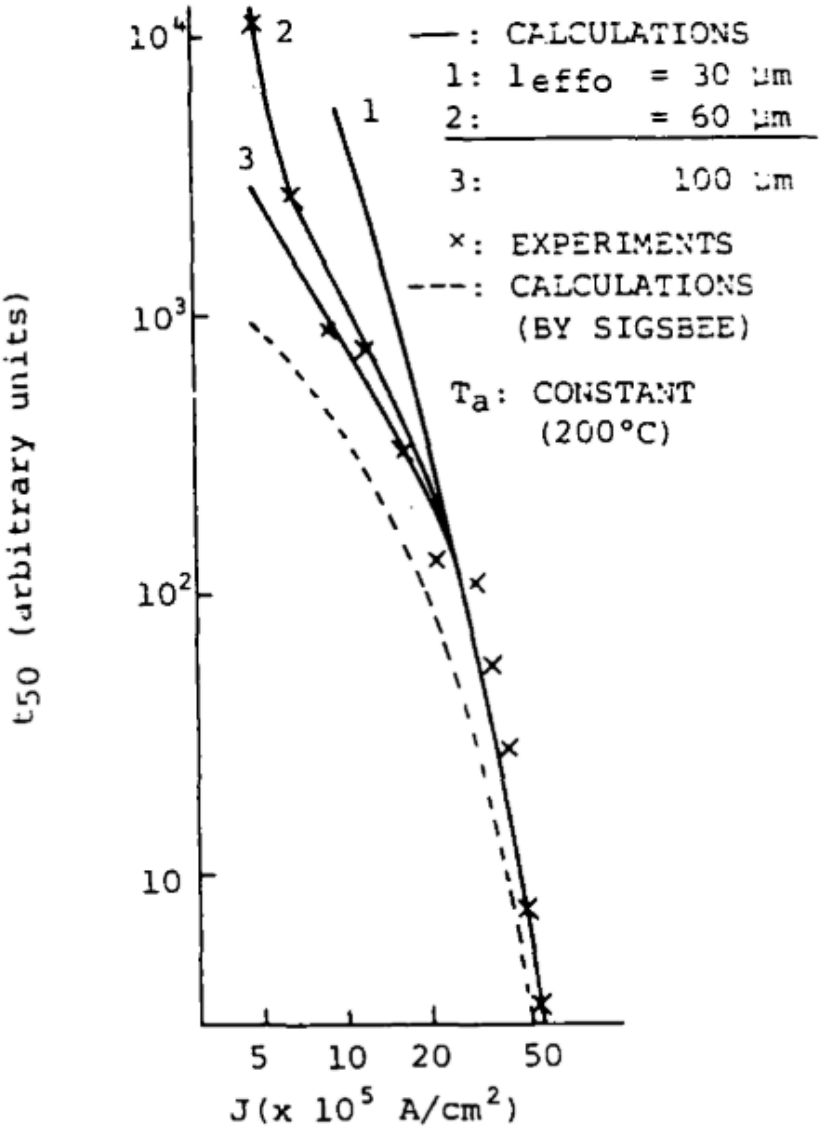

Figure A.16: Current density dependence of the median time to failure (t_{50}, arbitrary units) due to electromigration. Here l_{effo} is the threshold length (minimum length of the stripe required to undergo electromigration). The experiments were made on metal strips. Ref. [Scorzoni et al., 1991].

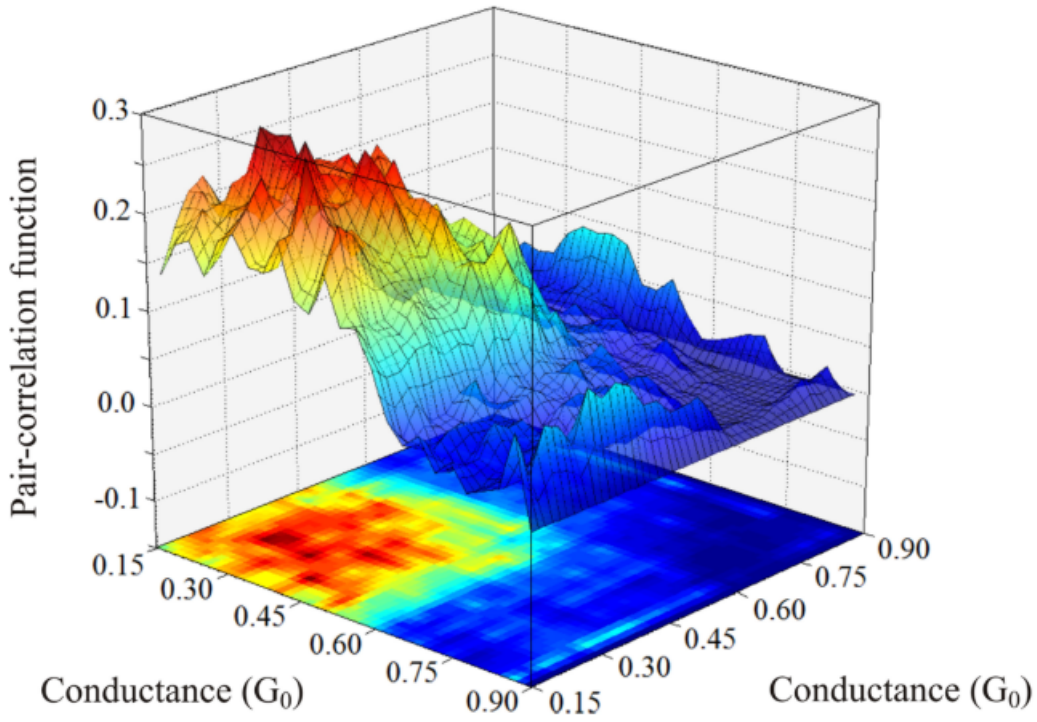

Figure A.17: Pair-correlation function for (intermediary) conductance jumps in an electrochemical gold single atom transistor when a switching bias voltage is applied. The correlation function is proportional to the number of jumps between two conductance values. If there is a correlation between the number of switching events and the conductances values, in other words, if some conductance jumps are more likely to occur than others, the correlation function would not be constant. This is the case here, demonstrating that there are "preferred" values of switching and therefore there are "preferred" intermediary conductance configurations while switching between 0 and 1 G_0. Ref. [Maul et al., 2012].

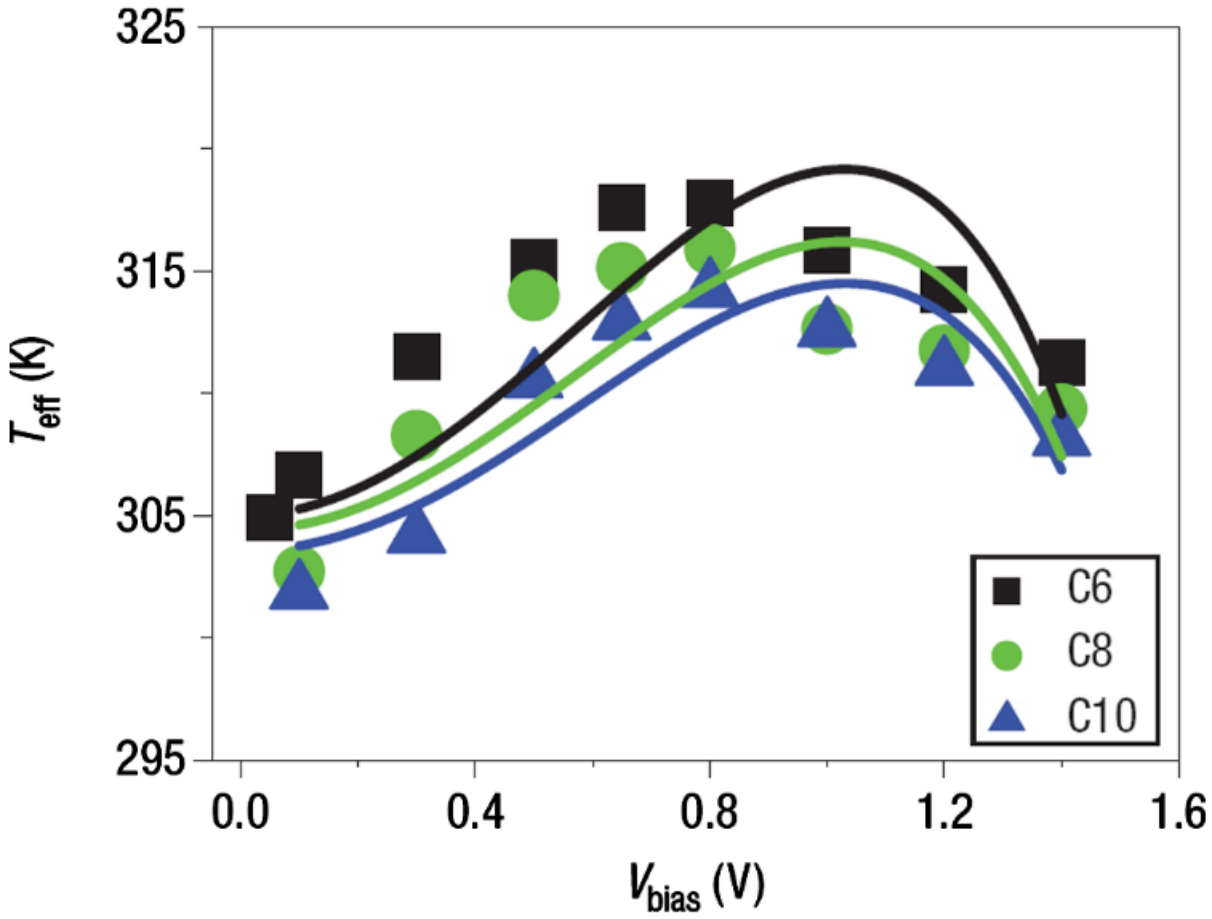

Figure A.18: Effective phonon temperature as a function of bias voltage of a molecular junction for three different molecules (C6: 1,6-alkanedithiol, C8: 1,8-alkanedithiol, C10: 1,10-alkanedithiol). The curves represent the fit from the equation $T_{\text{eff}}^4 = T_0^4 + \gamma_{\text{e-p}}^4 V_{\text{bias}}^2 - \gamma_{\text{e-e}}^4 V_{\text{bias}}^4$ and the solid dots represent the measured values. Ref. [Huang et al., 2007].

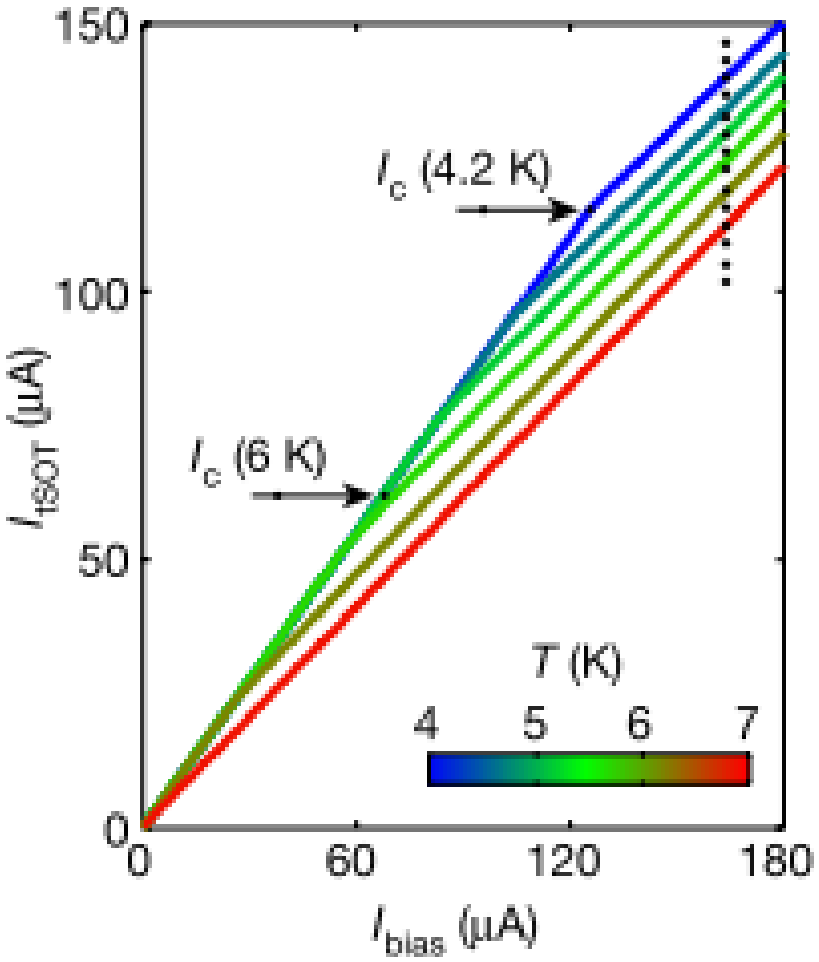

Figure A.19: Electrical characteristics of a Pb superconducting tip used as a temperature sensor at low temperatures (4.2 to 7.2 K): I_{tSOT} is the current in the superconducting tip while I_{bias} is the externally applied bias current. This bias current is applied in the tip which is connected in parallel to a shunt resistor. When $I_{bias} > I_c$, the current flows mostly into the shunt resistor. Critical current (I_c) values for specific temperatures are also indicated. See also Figure A.20. When $I_{bias} > I_c$ (dashed lines), the current is directly proportional to the temperature. This is used to measure temperature. Ref. [Halbertal et al., 2016].

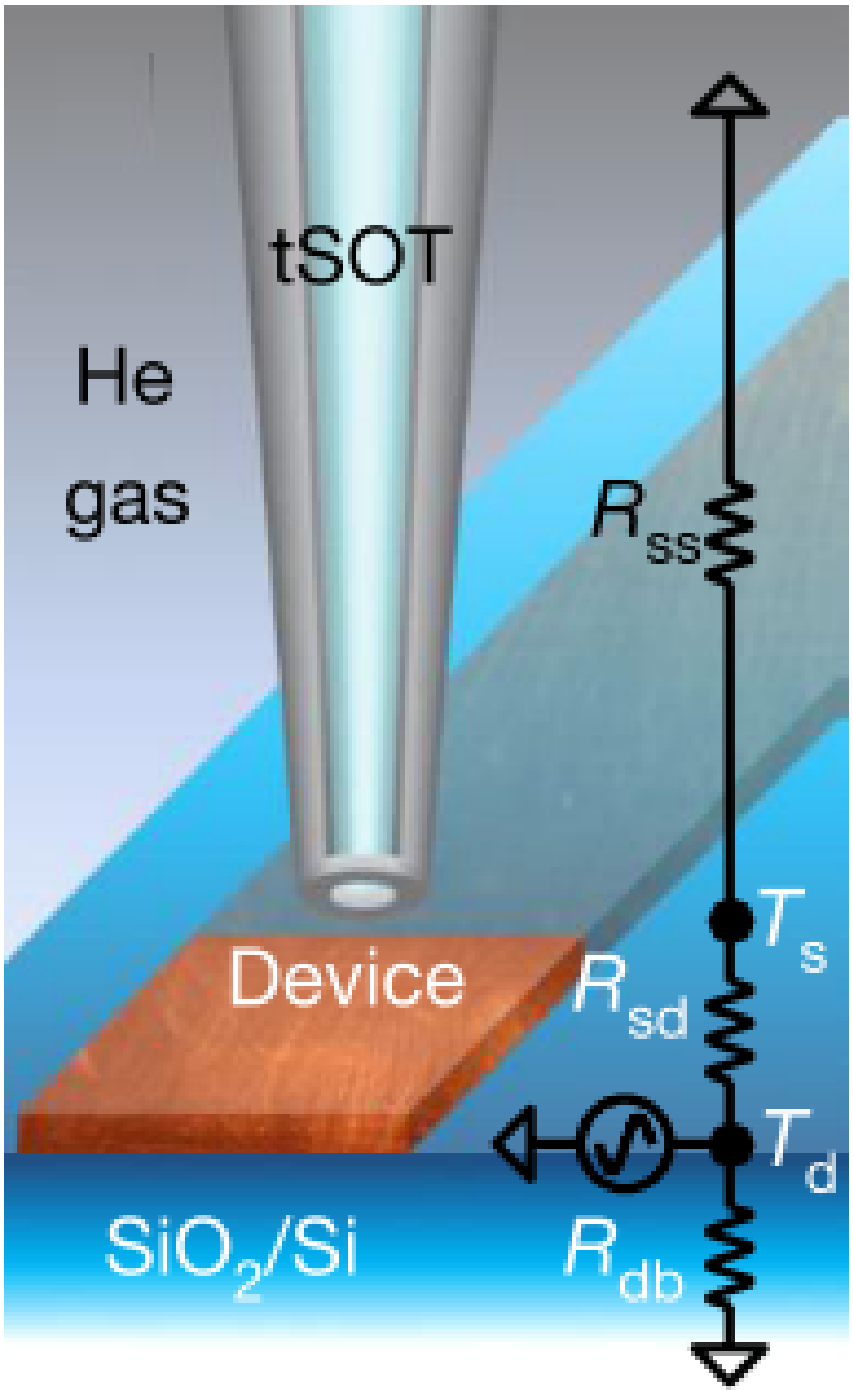

Figure A.20: Schematic drawing of the Pb superconducting tip used as a temperature sensor. The circuit showed on the right is the effective thermal circuit, R_{ss} is the thermal resistance between the tip and the support structure, R_{sd} is the tip-sample contact resistance, R_{db} is the resistance between the sample and the bulk of its substrate, T_d is the device temperature and T_s is the sensor temperature. The "sinusoidal source" shown represent the heat generated by the sample. The tip has a diameter of 46 nm. Ref. [Halbertal et al., 2016].

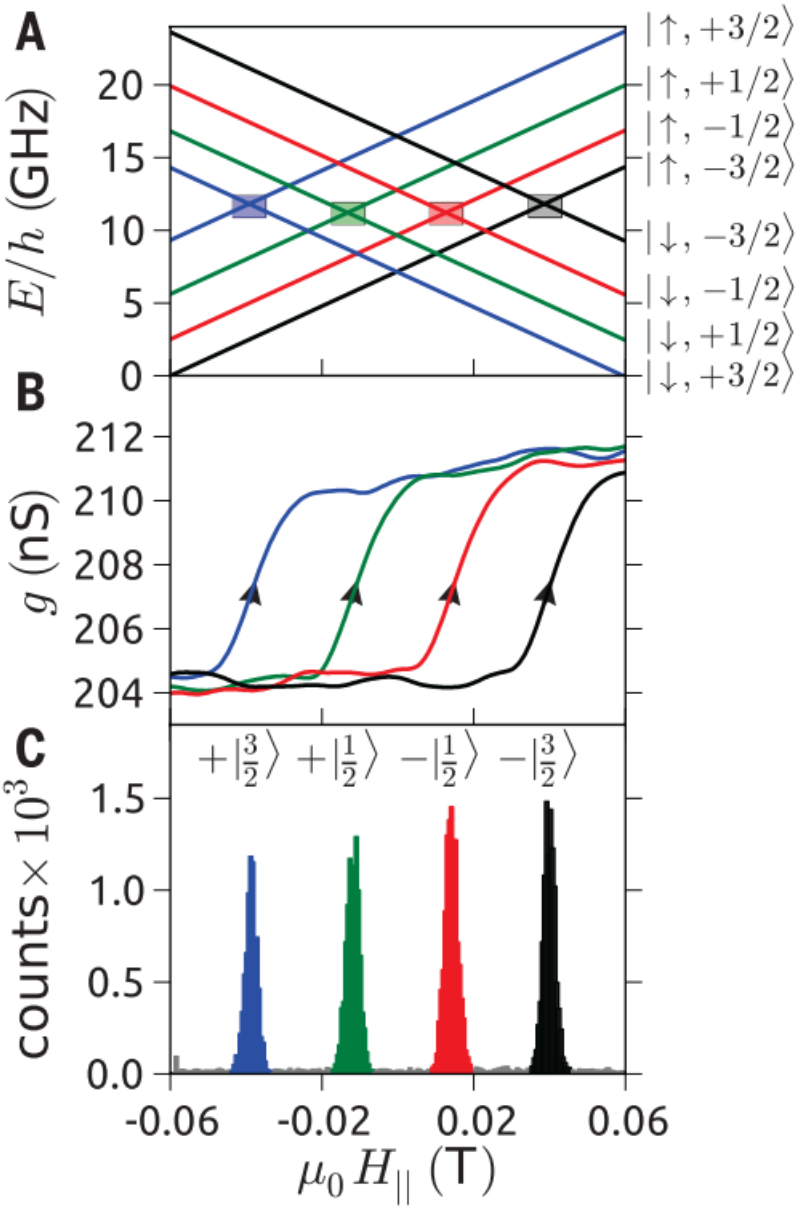

Figure A.21: a) Zeeman diagram of the quantum states in $TbPc_2$ qubit transistor. The kets include the electronic spin state (up or down), while the numerical values represent the nuclear spin state. b) Conductance jumps as a function of an external magnetic field for different nuclear spin states. It enables the identification of the qubit state. c) Histograms of the position of the 75 000 conductances; each peak can be associated to a nuclear spin state. Ref. [Thiele et al., 2014].

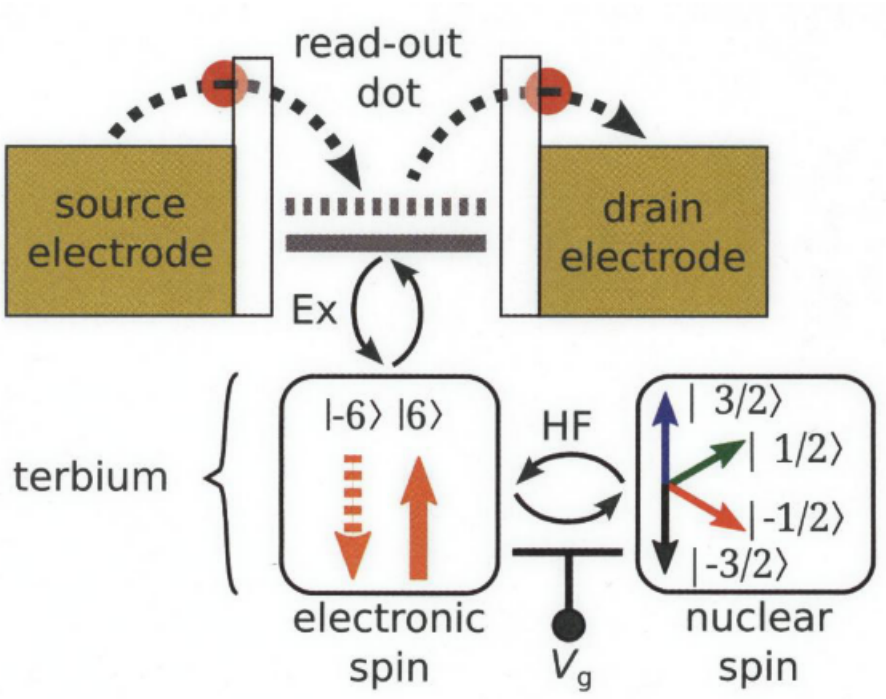

Figure A.22: Nuclear spin qubit transistor and its working scheme. It is made of up of three subsystems. The four-level nuclear spin is coupled with hyperfine interaction (controlled by the gate voltage V_g) to the electronic spin which is in turn coupled to the read-out quantum dot using anti-ferromagnetic interaction exchange. Ref. [Thiele et al., 2014].

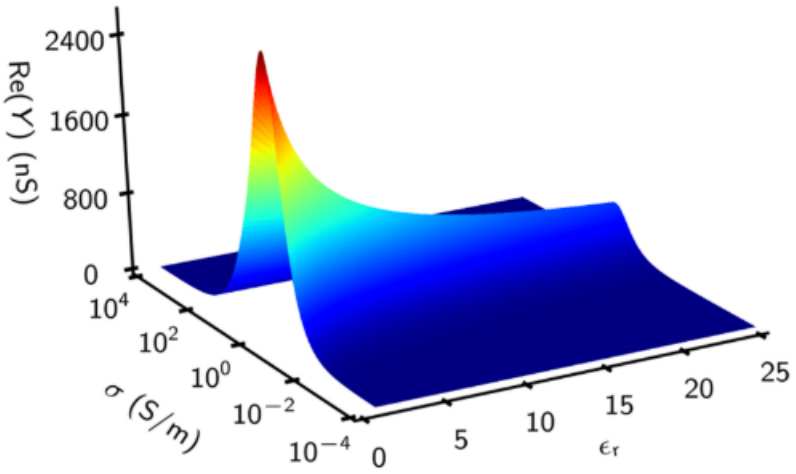

(a) Real part.

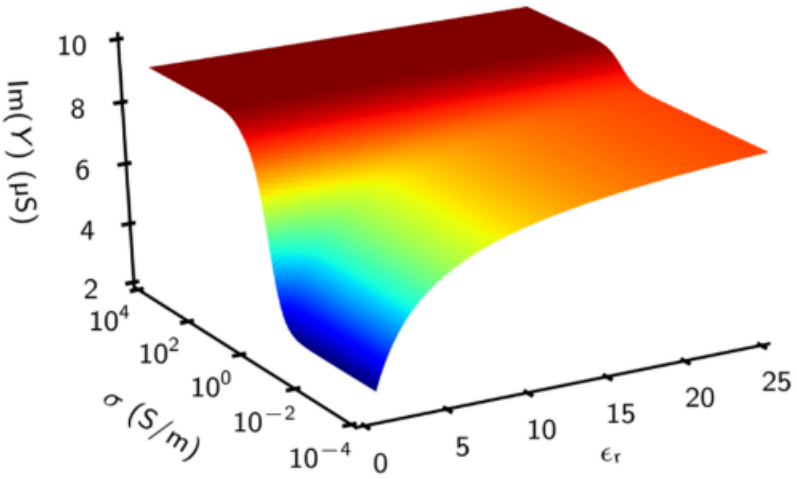

(b) Imaginary part.

Figure A.23: a) Real and b) imaginary parts of the tip-sample admittance as a function of permittivity and conductivity of the studied sample as obtained by numerical simulation. This sample was only characterized by its conductivity and permittivity. Ref. [Jones et al., 2017].

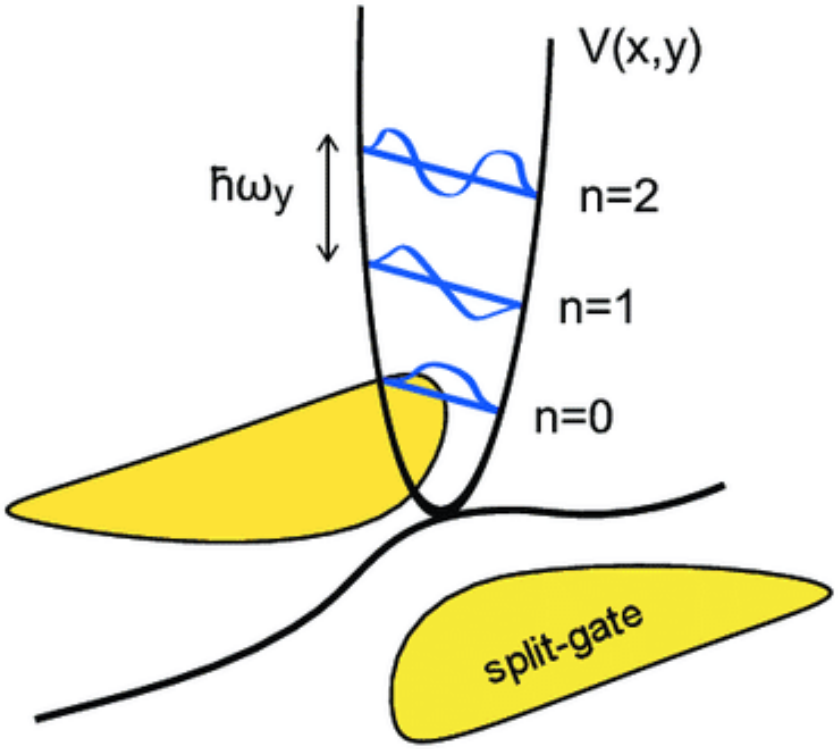

Figure A.24: Schematic explanation of the transverse modes in a QPC. Ref. [Jouan et al., 2020].

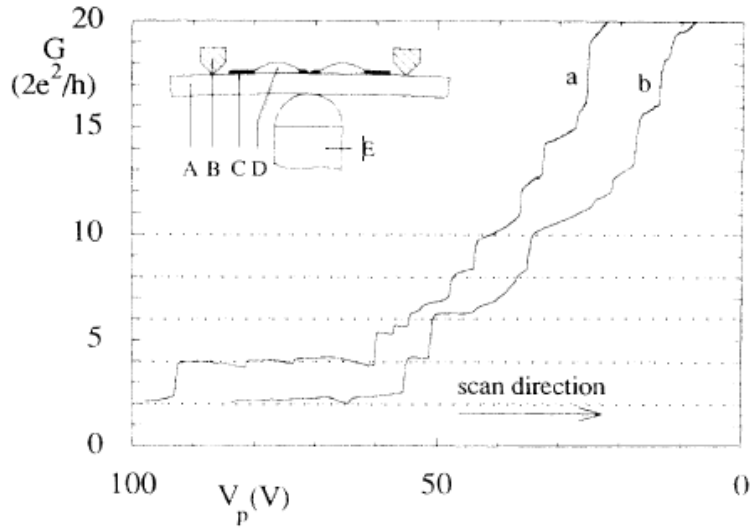

Figure A.25: First conductance steps observed in metallic junctions, with V_p the piezo voltage, used to tune the diameter of the junction. Ref. [Muller et al., 1992].

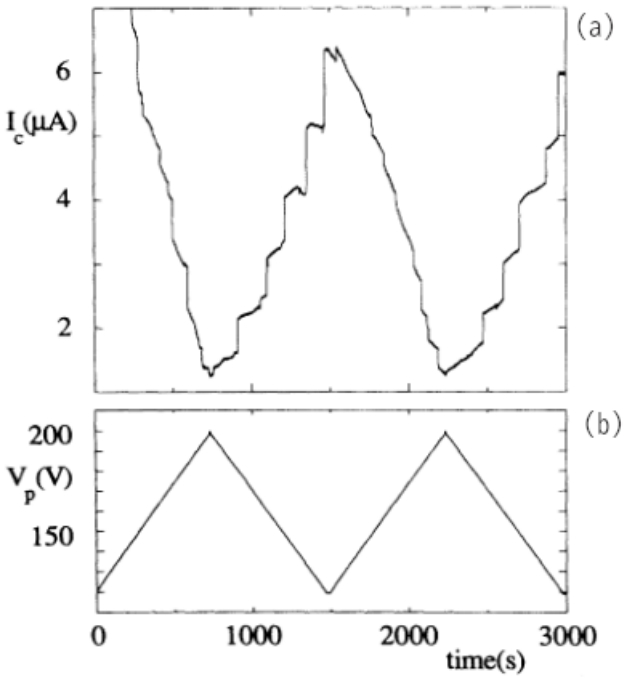

Figure A.26: a) Critical current I_c in a Nb superconducting QPC. b) Piezovoltage applied. The piezovoltage is inversely proportional to the channel width. Ref. [Muller et al., 1992].

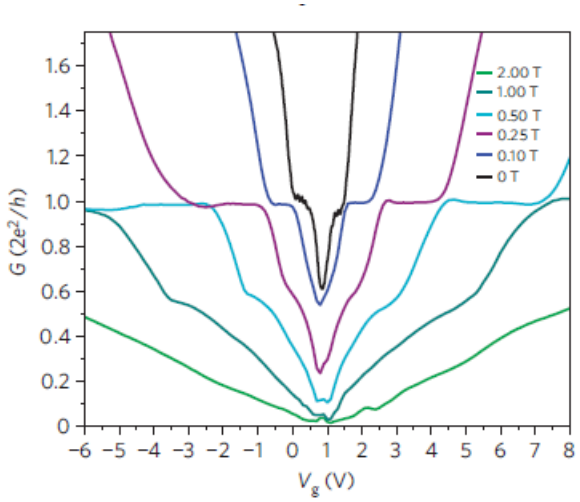

Figure A.27: Quantized conductance in a graphene nanoconstriction at different magnetic field values at 4.2 K. Ref. [Tombros et al., 2011].

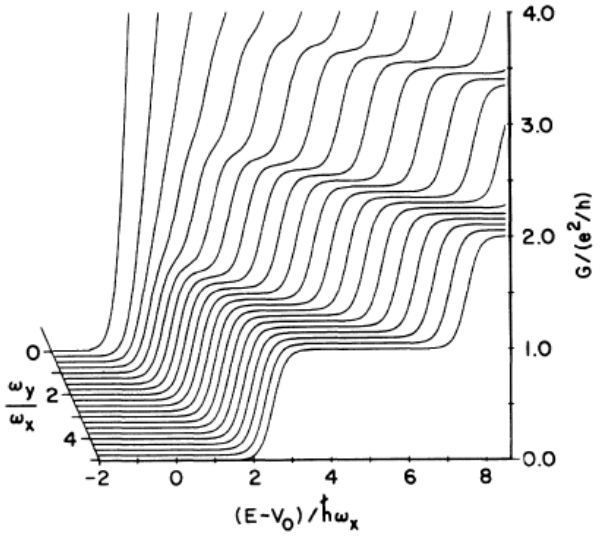

Figure A.28: Theoretically calculated values of conductance in a quantum point contact described by the "saddle-point model" as a function of $(E - V_0)/\hbar\omega_x$ for different potentials. Here ω_x and ω_y are parameters that describe the confining potential defining this QPC and E is the electron energy. The saddle point model is a way to model a quantum point contact (i.e. a narrow conduction channel for electrons). In this model, electrons travel between two leads (perfect reservoirs of electrons) through a channel in the x-direction. The channel is defined by a confining potential $V(x, y) = V_0 - \frac{1}{2}m\omega_x^2 x^2 + \frac{1}{2}m\omega_y^2 y^2$. Ref. [Büttiker, 1990].

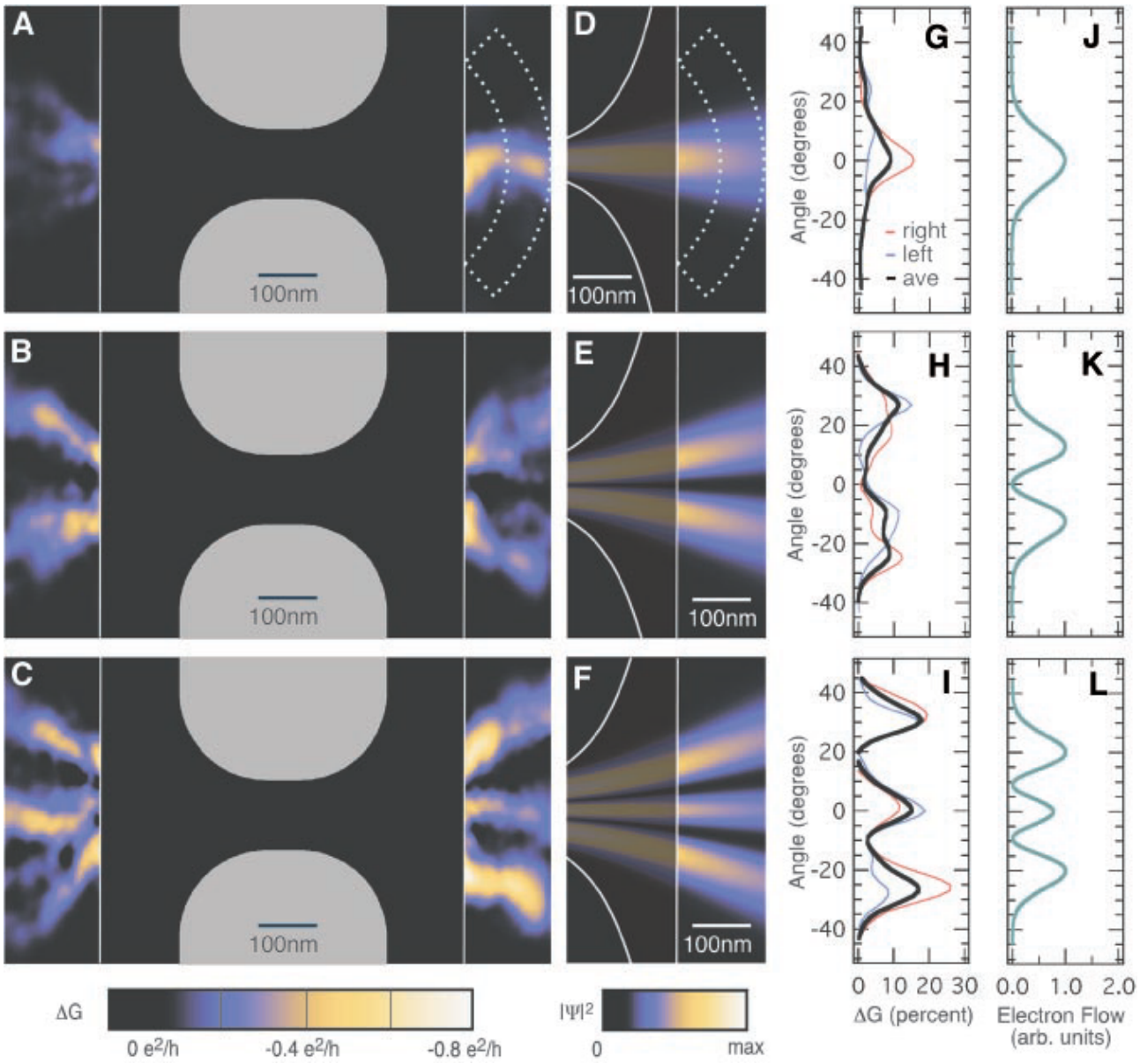

Figure A.29: a - c) Electronic density measured by an AFM tip around a QPC. d - f) Theoretical values of the electronic density for the same situation. g - i) Measured angular distribution of the electron flow. j - k) Calculated angular distribution of the wavefunction. First row: First mode. Second row: second mode. Third row: third mode. Ref. [Topinka et al., 2000].

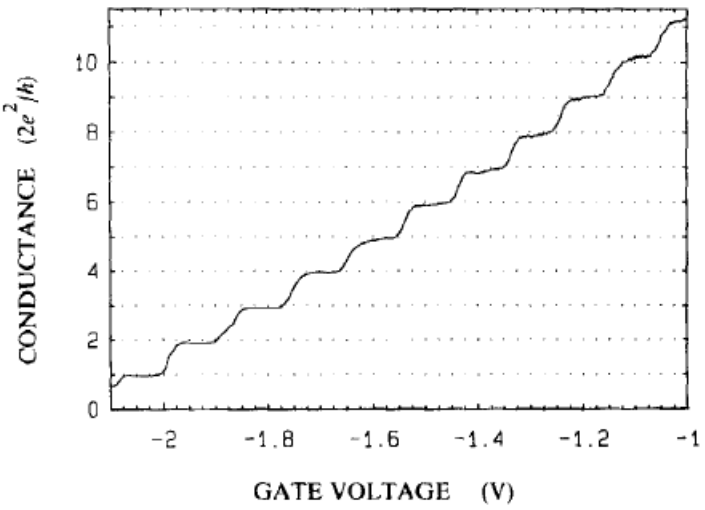

Figure A.30: First experimental observation of quantized conductance. This data was obtained at low temperature (0.6 K). Ref. [van Wees et al., 1988].

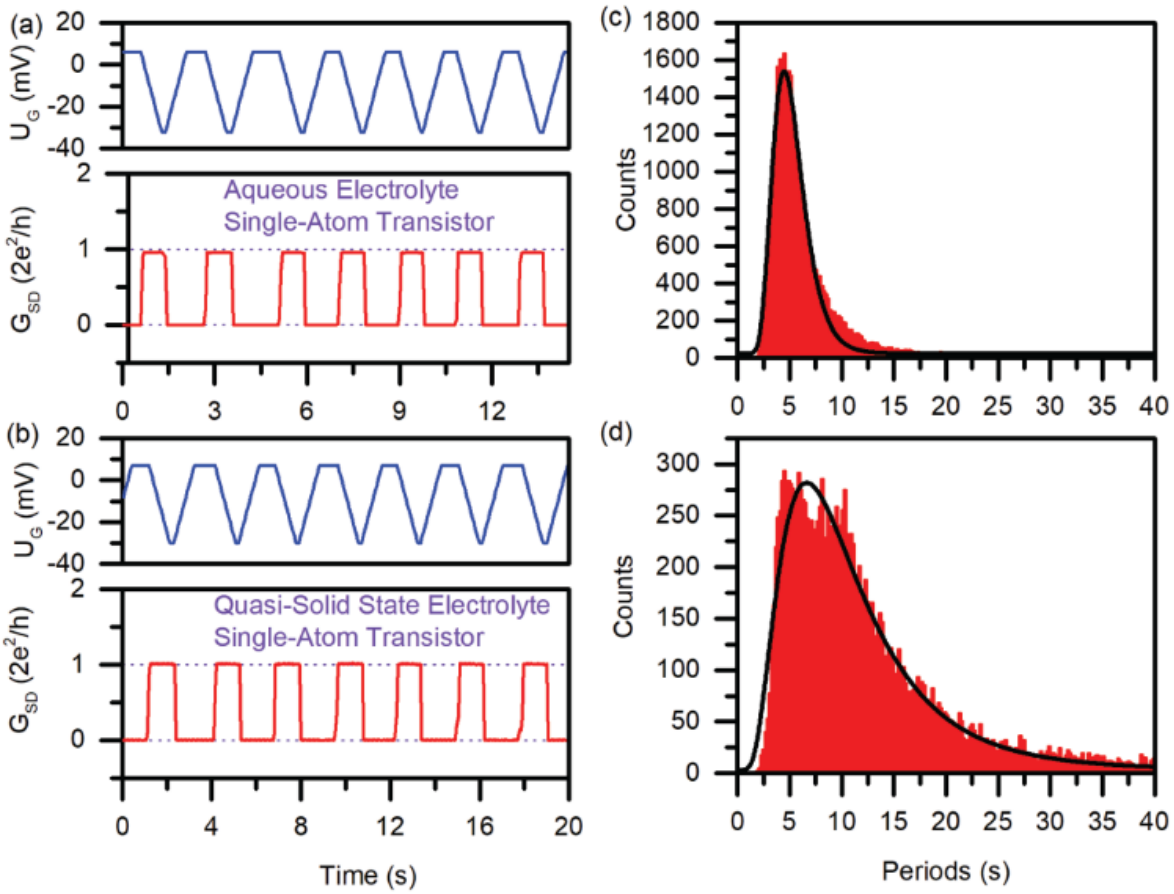

Figure A.31: a, b) Top: control voltage as a function of time. Bottom: Measured conductance as a function of time. c, d) Histogram of the switching counts. First row: aqueous electrolyte SAT. Second row: quasi-solid state electrolyte SAT. Ref. [Xie et al., 2018].

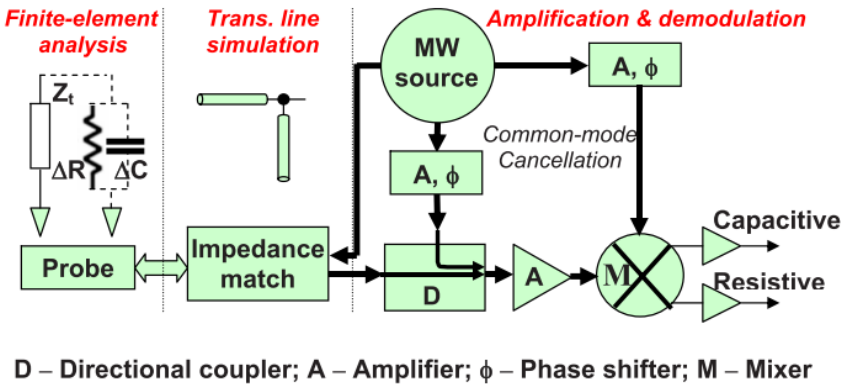

Figure A.32: Block diagram of the microwave impedance microscopy setup. Ref. [Lai et al., 2008].

List of Figures

Bibliography

[Agrait et al., 2003] Agrait, N., Yeyati, A. L., and van Ruitenbeek, J. M. (2003). Quantum properties of atomic-sized conductors. *Physics Reports*, 377(2-3):81–279.

[Ahmadi et al., 2016] Ahmadi, E., Keller, S., and Mishra, U. K. (2016). Model to explain the behavior of 2DEG mobility with respect to charge density in N-polar and Ga-polar AlGaN-GaN heterostructures. *Journal of Applied Physics*, 120(11):115302.

[Akis and Ferry, 2006] Akis, R. and Ferry, D. K. (2006). Spin filtering effects in a quantum point contact. In Saraniti, M. and Ravaioli, U., editors, *Nonequilibrium Carrier Dynamics in Semiconductors*, pages 163–166, Berlin, Heidelberg. Springer Berlin Heidelberg.

[Arute et al., 2019] Arute, F., Arya, K., Babbush, R., Bacon, D., Bardin, J. C., Barends, R., Biswas, R., Boixo, S., Brandao, F. G., Buell, D. A., Burkett, B., Chen, Y., Chen, Z., Chiaro, B., Collins, R., Courtney, W., Dunsworth, A., Farhi, E., Foxen, B., Fowler, A., Gidney, C., Giustina, M., Graff, R., Guerin, K., Habegger, S., Harrigan, M. P., Hartmann, M. J., Ho, A., Hoffmann, M., Huang, T., Humble, T. S., Isakov, S. V., Jeffrey, E., Jiang, Z., Kafri, D., Kechedzhi, K., Kelly, J., Klimov, P. V., Knysh, S., Korotkov, A., Kostritsa, F., Landhuis, D., Lindmark, M., Lucero, E., Lyakh, D., Mandrà, S., McClean, J. R., McEwen, M., Megrant, A., Mi, X., Michielsen, K., Mohseni, M., Mutus, J., Naaman, O., Neeley, M., Neill, C., Niu, M. Y., Ostby, E., Petukhov, A., Platt, J. C., Quintana, C., Rieffel, E. G., Roushan, P., Rubin, N. C., Sank, D., Satzinger, K. J., Smelyanskiy, V., Sung, K. J., Trevithick, M. D., Vainsencher, A., Villalonga, B., White, T., Yao, Z. J., Yeh, P., Zalcman, A., Neven, H., and Martinis, J. M. (2019). Quantum supremacy using a programmable superconducting processor. *Nature*, 574(7779):505–510.

[Asghar et al., 2010] Asghar, W., Ramachandran, P. P., Adewumi, A., Noor, M. R., and Iqbal, S. M. (2010). Rapid nanomanufacturing of metallic break junctions using focused ion beam scratching and electromigration. *Journal of Manufacturing Science and Engineering, Transactions of the ASME*, 132(3):0309111–0309114.

[Baibich et al., 1988] Baibich, M. N., Broto, J. M., Fert, A., Van Dau, F. N., Petroff, F., Eitenne, P., Creuzet, G., Friederich, A., and Chazelas, J. (1988). Giant magnetoresistance of (001)Fe/(001)Cr magnetic superlattices. *Physical Review Letters*, 61(21):2472–2475.

[Baldini et al., 1993] Baldini, G. L., De Munari, I., Scorzoni, A., and Fantini, F. (1993). Electromigration in thin-films for microelectronics. *Microelectronics Reliability*, 33(11-12):1779–1805.

[Ballmann and Weber, 2012] Ballmann, S. and Weber, H. B. (2012). An electrostatic gate for mechanically controlled single-molecule junctions. *New Journal of Physics*, 14(12):123028.

[Beenakker and van Houten, 1991] Beenakker, C. W. J. and van Houten, H. (1991). Josephson current through a superconducting quantum point contact shorter than the coherence length. *Phys. Rev. Lett.*, 66:3056–3059.

[Blanter and Büttiker, 2000] Blanter, Y. M. and Büttiker, M. (2000). Shot noise in mesoscopic conductors. *Physics Report*, 336(1-2):1–166.

[Brites et al., 2012] Brites, C. D., Lima, P. P., Silva, N. J., Millán, A., Amaral, V. S., Palacio, F., and Carlos, L. D. (2012). Thermometry at the nanoscale. *Nanoscale*, 4(16):4799–4829.

[Brun, 2014] Brun, B. (2014). *Electron interactions in mesoscopic physics: Scanning Gate Microscopy and interferometry at a quantum point contact.* PhD thesis, Université de Genève.

[Büttiker, 1990] Büttiker, M. (1990). Quantized transmission of a saddle-point constriction. *Phys. Rev. B*, 41:7906–7909.

[Büttiker, 1992] Büttiker, M. (1992). Scattering theory of current and intensity noise correlations in conductors and wave guides. *Physical Review B*, 46(19):12485–12507.

[Champagne et al., 2005] Champagne, A. R., Pasupathy, A. N., and Ralph, D. C. (2005). Mechanically adjustable and electrically gated single-molecule transistors. *Nano Letters*, 5(2):305–308.

[Chen and Webb, 2006] Chen, Y. and Webb, R. A. (2006). Full shot noise in mesoscopic tunnel barriers. *Physical Review B - Condensed Matter and Materials Physics*, 73(3):035424.

[Chen et al., 2005] Chen, Y.-c., Zwolak, M., and Di Ventra, M. (2005). Inelastic effects on the transport properties of alkanethiols. *Nano Letters*, 5:621–624.

[Cui et al., 2016] Cui, Y. T., Ma, E. Y., and Shen, Z. X. (2016). Quartz tuning fork based microwave impedance microscopy. *Review of Scientific Instruments*, 87(6):063711.

[D'Agosta and Ventra, 2006] D'Agosta, R. and Ventra, M. D. (2006). Hydrodynamic approach to transport and turbulence in nanoscale conductors. *Journal of Physics: Condensed Matter*, 18(49):11059–11065.

[Datta, 1995] Datta, S. (1995). *Electronic Transport in Mesoscopic Systems.* Cambridge Studies in Semiconductor Physics and Microelectronic Engineering. Cambridge University Press.

[de Heer et al., 1997] de Heer, W., Frank, S., and Ugarte, D. (1997). Fractional quantum conductance in gold nanowires. *Zeitschrift für Physik B Condensed Matter*, 104(3):469–473.

[De Los Santos Valladares et al., 2010] De Los Santos Valladares, L., Felix, L. L., Dominguez, A. B., Mitrelias, T., Sfigakis, F., Khondaker, S. I., Barnes, C. H., and Majima, Y. (2010). Controlled electroplating and electromigration in nickel electrodes for nanogap formation. *Nanotechnology*, 21(44):445304.

[Dubi and Di Ventra, 2011] Dubi, Y. and Di Ventra, M. (2011). Colloquium: Heat flow and thermoelectricity in atomic and molecular junctions. *Rev. Mod. Phys.*, 83:131–155.

[Galperin et al., 2007] Galperin, M., Nitzan, A., and Ratner, M. A. (2007). Heat conduction in molecular transport junctions. *Phys. Rev. B*, 75:155312.

[Galperin et al., 2009] Galperin, M., Saito, K., Balatsky, A. V., and Nitzan, A. (2009). Cooling mechanisms in molecular conduction junctions. *Phys. Rev. B*, 80:115427.

[Giazotto et al., 2006] Giazotto, F., Heikkilä, T. T., Luukanen, A., Savin, A. M., and Pekola, J. P. (2006). Opportunities for mesoscopics in thermometry and refrigeration: Physics and applications. *Rev. Mod. Phys.*, 78:217–274.

[Gong et al., 2013] Gong, C., Zhao, Y., Dong, L., Hui, M., Yu, X., and Liu, X. (2013). The tolerable target temperature for bimaterial microcantilever array infrared imaging. *Optics Laser Technology*, 45:545–550.

[Groth et al., 2014] Groth, C. W., Wimmer, M., Akhmerov, A. R., and Waintal, X. (2014). Kwant: A software package for quantum transport. *New Journal of Physics*, 16:1–19.

[Halbertal et al., 2016] Halbertal, D., Cuppens, J., Shalom, M. B., Embon, L., Shadmi, N., Anahory, Y., Naren, H. R., Sarkar, J., Uri, A., Ronen, Y., Myasoedov, Y., Levitov, L. S., Joselevich, E., Geim, A. K., and Zeldov, E. (2016). Nanoscale thermal imaging of dissipation in quantum systems. *Nature*, 539:407.

[Heersche et al., 2007] Heersche, H. B., Lientschnig, G., O'Neill, K., van der Zant, H. S., and Zandbergen, H. W. (2007). In situ imaging of electromigration-induced nanogap formation by transmission electron microscopy. *Applied Physics Letters*, 91(7):2005–2008.

[Ho and Huntington, 1966] Ho, P. S. and Huntington, H. B. (1966). Electromigration and void observation in silver. *Journal of Physics and Chemistry of Solids*, 27(8):1319–1329.

[Huang et al., 2007] Huang, Z., Chen, F., D'Agosta, R., Bennett, P. A., Di Ventra, M., and Tao, N. (2007). Local ionic and electron heating in single-molecule junctions. *Nature Nanotechnology*, 2(11):698–703.

[Hwang et al., 2014] Hwang, G., Chung, J., and Kwon, O. (2014). Enabling low-noise null-point scanning thermal microscopy by the optimization of scanning thermal microscope probe through a rigorous theory of quantitative measurement. *Review of Scientific Instruments*, 85(11):114901.

[Jones et al., 2015] Jones, T. S., Pérez, C. R., and Santiago-Avilés, J. J. (2015). Simulation of sample inhomogeneity in microwave impedance microscopy. *Proceedings of the 2015 COMSOL Conference.*

[Jones et al., 2017] Jones, T. S., Pérez, C. R., and Santiago-Avilés, J. J. (2017). Quantitative microwave impedance microscopy with effective medium approximations. *AIP Advances*, 7(2):025207.

[Jouan et al., 2020] Jouan, A., Singh, G., Lesne, E., Vaz, D., Bibes, M., Barthelemy, A., Ulysse, C., Stornaiuolo, D., Salluzzo, M., Hurand, S., Lesueur, J., Feuillet-Palma, C., and Bergeal, N. (2020). Quantized conductance in a one-dimensional ballistic oxide nanodevice. *Nature Electronics*, 3:201–206.

[Kane, 1998] Kane, B. E. (1998). A silicon-based nuclear spin quantum computer. *Nature*, 393(6681):133–137.

[Kittel, 2007] Kittel, C. (2007). *Introduction to Solid State Physics,* 7^{th} *Ed.* Wiley.

[Lai et al., 2008] Lai, K., Kundhikanjana, W., Kelly, M., and Shen, Z. X. (2008). Modeling and characterization of a cantilever-based near-field scanning microwave impedance microscope. *Review of Scientific Instruments*, 79(6):063703.

[Lai et al., 2009] Lai, K., Kundhikanjana, W., Peng, H., Cui, Y., Kelly, M. A., and Shen, Z. X. (2009). Tapping mode microwave impedance microscopy. *Review of Scientific Instruments*, 80(4):2–4.

[Lee et al., 2016] Lee, K., Jeong, J., Bahk, Y. M., Rhie, J., Baek, I. K., Lee, B. J., Kang, Y. H., Hong, S., Park, G. S., and Kim, D. S. (2016). Microwave funneling through sub-10 nm nanogaps. *ACS Photonics*, 3(4):537–542.

[Li et al., 2000] Li, C. Z., He, H. X., and Tao, N. J. (2000). Quantized tunneling current in the metallic nanogaps formed by electrodeposition and etching. *Applied Physics Letters*, 77(24):3995–3997.

[Liu et al., 2015] Liu, M. H., Rickhaus, P., Makk, P., Tóvári, E., Maurand, R., Tkatschenko, F., Weiss, M., Schönenberger, C., and Richter, K. (2015). Scalable tight-binding model for graphene. *Physical Review Letters*, 114(3):1–5.

[Majidi, 2018] Majidi, M. A. (2018). Electron hopping integral renormalization due to anharmonic phonons. *Journal of Physics: Conference Series*, 1011(1):012080.

[Majumdar, 1999] Majumdar, A. (1999). Scanning thermal microscopy. *Annual Review of Materials Science*, 29(1):505–585.

[Martin et al., 2008] Martin, C. A., Ding, D., van der Zant, H. S. J., and van Ruitenbeek, J. M. (2008). Lithographic mechanical break junctions for single-molecule measurements in vacuum: possibilities and limitations. *New Journal of Physics*, 10(6):065008.

[Martin et al., 2009] Martin, C. A., Smit, R. H. M., van der Zant, H. S. J., and van Ruitenbeek, J. M. (2009). A nanoelectromechanical single-atom switch. *Nano Letters*, 9(8):2940–2945. PMID: 19639963.

[Martin et al., 2010] Martin, C. A., van Ruitenbeek, J. M., and van der Zant, H. S. J. (2010). Sandwich-type gated mechanical break junctions. *Nanotechnology*, 21(26):265201.

[Maul et al., 2012] Maul, R., Xie, F. Q., Obermair, C., Schön, G., Schimmel, T., and Wenzel, W. (2012). Memory effects in electrochemically gated metallic point contacts. *Applied Physics Letters*, 100(20):20351.

[Meir and Wingreen, 1992] Meir, Y. and Wingreen, N. S. (1992). Landauer formula for the current through an interacting electron region. *Phys. Rev. Lett.*, 68:2512–2515.

[Meng et al., 2015] Meng, C., Huang, P., Zhou, J.-W., Duan, C.-K., and Du, J.-F. (2015). Thermally controllable break junctions with high bandwidths and high integrabilities. *Chinese Physics Letters*, 32(07):076201.

[Menges et al., 2016] Menges, F., Mensch, P., Schmid, H., Riel, H., Stemmer, A., and Gotsmann, B. (2016). Temperature mapping of operating nanoscale devices by scanning probe thermometry. *Nature Communications*, 7:1–6.

[Menges et al., 2012] Menges, F., Riel, H., Stemmer, A., and Gotsmann, B. (2012). Quantitative thermometry of nanoscale hot spots. *Nano Letters*, 12(2):596–601.

[Moreland and Hansma, 1984] Moreland, J. and Hansma, P. K. (1984). Electromagnetic squeezer for compressing squeezable electron tunneling junctions. *Review of Scientific Instruments*, 55(3):399–403.

[Morpurgo et al., 1999] Morpurgo, A. F., Marcus, C. M., and Robinson, D. B. (1999). Controlled fabrication of metallic electrodes with atomic separation. *Applied Physics Letters*, 74(14):2084–2086.

[Muller et al., 1992] Muller, C. J., van Ruitenbeek, J. M., and de Jongh, L. J. (1992). Conductance and supercurrent discontinuities in atomic-scale metallic constrictions of variable width. *Phys. Rev. Lett.*, 69:140–143.

[Naitoh et al., 2013] Naitoh, Y., Ohata, T., Matsushita, R., Okawa, E., Horikawa, M., Oyama, M., Mukaida, M., Wang, D. F., Kiguchi, M., Tsukagoshi, K., and Ishida, T. (2013). Self-aligned formation of sub 1 nm gaps utilizing electromigration during metal deposition. *ACS Applied Materials and Interfaces*, 5(24):12869–12875.

[Naveh, 1998] Naveh, Y. (1998). Direct determination of the electron-electron mean free path in diffusive mesoscopic samples using shot noise. *Physical Review B - Condensed Matter and Materials Physics*, 58(20):R13387–R13390.

[Obermair et al., 2010] Obermair, C., Xie, F.-Q., and Schimmel, T. (2010). The single-atom transistor: Perspectives for quantum electronics on the atomic-scale. *Europhysics News*, 41:25–28.

[O'Neill et al., 2007] O'Neill, K., Osorio, E. A., and Van Der Zant, H. S. (2007). Self-breaking in planar few-atom au constrictions for nanometer-spaced electrodes. *Applied Physics Letters*, 90(13):2005–2008.

[Peercy, 2000] Peercy, P. S. (2000). The drive to miniaturization. *Nature*, 406(6799):1023–1026.

[Perrin et al., 2015] Perrin, M. L., Burzurí, E., and van der Zant, H. S. J. (2015). Single-molecule transistors. *Chem. Soc. Rev.*, 44:902–919.

[Prins et al., 2009] Prins, F., Hayashi, T., De Vos Van Steenwijk, B. J., Gao, B., Osorio, E. A., Muraki, K., and van der Zant, H. S. (2009). Roomerature stability of Pt nanogaps formed by self-breaking. *Applied Physics Letters*, 94(12):2007–2010.

[Rubio et al., 1996] Rubio, G., Agraït, N., and Vieira, S. (1996). Atomic-sized metallic contacts: Mechanical properties and electronic transport. *Phys. Rev. Lett.*, 76:2302–2305.

[Scheibner et al., 2005] Scheibner, R., Buhmann, H., Reuter, D., Kiselev, M. N., and Molenkamp, L. W. (2005). Thermopower of a kondo spin-correlated quantum dot. *Phys. Rev. Lett.*, 95:176602.

[Scheibner et al., 2007] Scheibner, R., Novik, E. G., Borzenko, T., König, M., Reuter, D., Wieck, A. D., Buhmann, H., and Molenkamp, L. W. (2007). Sequential and cotunneling behavior in the temperature-dependent thermopower of few-electron quantum dots. *Phys. Rev. B*, 75:041301.

[Schirm et al., 2013] Schirm, C., Matt, M., Pauly, F., Cuevas, J. C., Nielaba, P., and Scheer, E. (2013). A current-driven single-atom memory. *Nature Nanotechnology*, 8:645.

[Scorzoni et al., 1991] Scorzoni, A., Neri, B., Caprile, C., and Fantini, F. (1991). Electromigration in thin-film interconnection lines: Models, methods and results. *Materials Science Reports*, 7(4-5):143–220.

[Sheikholeslam et al., 2014] Sheikholeslam, S. A., Grecu, C., and Ivanov, A. (2014). Using magnetic controlled electromigration for electrode fabrication. In 14^{th} *IEEE International Conference on Nanotechnology*, pages 839–842.

[Thiele et al., 2014] Thiele, S., Balestro, F., Ballou, R., Klyatskaya, S., and Wernsdorfer, W. (2014). Electrically driven nuclear spin resonance in single-molecule magnets. *Science*, 344(6188):1135–1138.

[Todorov, 1998] Todorov, T. N. (1998). Local heating in ballistic atomic-scale contacts. *Philosophical Magazine B*, 77(4):965–973.

[Tombros et al., 2011] Tombros, N., Veligura, A., Junesch, J., Guimarães, M. H. D., Vera-Marun, I. J., Jonkman, H. T., and van Wees, B. J. (2011). Quantized conductance of a suspended graphene nanoconstriction. *Nature Physics*, 7(9):697–700.

[Topinka et al., 2000] Topinka, M. A., LeRoy, B. J., Shaw, S. E. J., Heller, E. J., Westervelt, R. M., Maranowski, K. D., and Gossard, A. C. (2000). Imaging coherent electron flow from a quantum point contact. *Science*, 289(5488):2323–2326.

[van Wees et al., 1988] van Wees, B. J., van Houten, H., Beenakker, C. W. J., Williamson, J. G., Kouwenhoven, L. P., van der Marel, D., and Foxon, C. T. (1988). Quantized conductance of point contacts in a two-dimensional electron gas. *Phys. Rev. Lett.*, 60:848–850.

[Vignale and Di Ventra, 2009] Vignale, G. and Di Ventra, M. (2009). Incompleteness of the landauer formula for electronic transport. *Phys. Rev. B*, 79:014201.

[Wang et al., 2008] Wang, J. S., Wang, J., and Lü, J. T. (2008). Quantum thermal transport in nanostructures. *European Physical Journal B*, 62(4):381–404.

[Wei et al., 2015] Wei, Z., Agarwal, K., and Chen, X. (2015). Analytical green's function for tip-sample interaction in microwave impedance microscopy. In *2015 IEEE MTT-S International Microwave Workshop Series on Advanced Materials and Processes for RF and THz Applications (IMWS-AMP)*, pages 1–3.

[Wei et al., 2016] Wei, Z., Cui, Y.-T., Ma, E. Y., Johnston, S., Yang, Y., Chen, R., Kelly, M., Shen, Z.-X., and Chen, X. (2016). Quantitative theory for probe-sample interaction with inhomogeneous perturbation in near-field scanning microwave microscopy. *IEEE Transactions on Microwave Theory and Techniques*, 64(5):1402–1408.

[Xiang et al., 2013] Xiang, D., Jeong, H., Kim, D., Lee, T., Cheng, Y., Wang, Q., and Mayer, D. (2013). Three-terminal single-molecule junctions formed by mechanically controllable break junctions with side gating. *Nano Letters*, 13(6):2809–2813.

[Xiang et al., 2016] Xiang, D., Wang, X., Jia, C., Lee, T., and Guo, X. (2016). Molecular-scale electronics: From concept to function. *Chemical Reviews*, 116(7):4318–4440.

[Xie et al., 2018] Xie, F., Peukert, A., Bender, T., Obermair, C., Wertz, F., Schmieder, P., and Schimmel, T. (2018). Quasi-solid-state single-atom transistors. *Advanced Materials*, 30(31):1801225.

[Xie et al., 2017] Xie, F.-Q., Lin, X.-H., Gross, A., Evers, F., Pauly, F., and Schimmel, T. (2017). Multiplicity of atomic reconfigurations in an electrochemical pb single-atom transistor. *Phys. Rev. B*, 95:195415.

[Xie et al., 2008] Xie, F.-Q., Maul, R., Brendelberger, S., Obermair, C., Starikov, E. B., Wenzel, W., Schön, G., and Schimmel, T. (2008). Preselectable integer quantum conductance of electrochemically fabricated silver point contacts. *Applied Physics Letters*, 93(4):043103.

[Xie et al., 2004] Xie, F.-Q., Nittler, L., Obermair, C., and Schimmel, T. (2004). Gate-controlled atomic quantum switch. *Phys. Rev. Lett.*, 93:128303.

[Yang et al., 2014] Yang, Y., Ma, E. Y., Cui, Y. T., Haemmerli, A., Lai, K., Kundhikanjana, W., Harjee, N., Pruitt, B. L., Kelly, M., and Shen, Z. X. (2014). Shielded piezoresistive cantilever probes for nanoscale topography and electrical imaging. *Journal of Micromechanics and Microengineering*, 24(4):045026.

[Zimmermann et al., 2017] Zimmermann, K., Jordan, A., Gay, F., Watanabe, K., Taniguchi, T., Han, Z., Bouchiat, V., Sellier, H., and Sacépé, B. (2017). Tunable transmission of quantum hall edge channels with full degeneracy lifting in split-gated graphene devices. *Nature Communications*, 8(1):14983.

UNIVERSITÉ CATHOLIQUE DE LOUVAIN
École polytechnique de Louvain
Rue Archimède, 1 bte L6.11.01, 1348 Louvain-la-Neuve, Belgique | **www.uclouvain.be/epl**